

# Abrupt changes and intervening oscillations in conceptual climate models

Andrew Roberts

A dissertation submitted to the faculty of the University of North Carolina at Chapel Hill in partial fulfillment of the requirements for the degree of Doctor of Philosophy in the Department of Mathematics.

Chapel Hill  
2014

Approved by:

Christopher K.R.T. Jones

Patrick Eberlein

Jeremy Marzuola

Richard McGehee

Mary Lou Zeeman

©2014  
Andrew Roberts  
ALL RIGHTS RESERVED

## ABSTRACT

ANDREW ROBERTS: Abrupt changes and intervening oscillations in conceptual climate models

(Under the direction of Christopher K.R.T. Jones)

This thesis examines the role of fast/slow dynamics in understanding the mechanisms behind oscillatory patterns found in paleoclimate data. Fast/slow systems often exhibit rapid transitions between metastable states, and understanding these transitions is important to understanding climate phenomena. However, these rapid changes in the state of the system implicitly require examining trajectories that enter a region of phase space where the basic theory used to analyze fast/slow systems no longer applies. The content of this thesis examines the non-standard behavior arising from the break down of the theory, typically appearing in the form of small amplitude oscillations due to canard trajectories. First, canard theory is extended to piecewise-smooth systems. Conditions are found in which canard behavior is similar to that of smooth systems. Additionally, the dynamics are classified when these conditions are not met. Second, the new theory is used to analyze a variation on Stommel's model of large-scale ocean circulation, showing that the model is capable of exhibiting both canards and relaxation oscillations. Another variation of Stommel's model with an extra phase-space dimension is also demonstrated to exhibit relaxation oscillations. Finally, a model for glacial-interglacial cycles is analyzed through the lens of mixed-mode oscillations. The model is demonstrated to exhibit complicated oscillations due to a generalized canard phenomenon.

To my parents, Alan and Geri, and my brother, Alex.

## ACKNOWLEDGEMENTS

This project would not have been possible without the help and support of many people. Many thanks to my advisor, Chris Jones, for always providing me with guidance and helping me keep perspective. I would also like to thank my committee members: Patrick Eberlein, Jeremy Marzuola, Richard McGehee, and Mary Lou Zeeman. Thank you for being so supportive. Thank you to University of North Carolina, the Statistical and Mathematical Sciences Institute, the University of Warwick, and the Mathematics and Climate Research Network for providing me with financial means to complete this dissertation. Thank you to the UNC math graduate students, especially James Martindale and Andrea Overbay, for being there on those frustrating days. Finally, thank you to my family and friends who provided me with emotional support every step of the way.

# TABLE OF CONTENTS

LIST OF FIGURES .....	ix
Chapter	
1. Introduction .....	1
1.1. Overview .....	1
1.2. Oscillations in Climate Data .....	2
1.2.1. Dansgaard-Oeschger Events .....	4
1.2.2. Glacial-Interglacial Cycles .....	6
1.3. Geometric Singular Perturbation Theory .....	7
1.4. Relaxation Oscillations, Fold Points, and Canards .....	11
2. Canard-like Phenomena in Piecewise-Smooth Planar Systems .....	16
2.1. Introduction .....	16
2.2. Background .....	19
2.2.1. Canards in smooth, planar systems .....	19
2.2.2. Quasi-canards in Piecewise Linear Systems .....	27
2.2.3. Nonsmooth Hopf Bifurcations .....	31
2.3. Main Results .....	32
2.3.1. Canards at the smooth fold .....	36
2.3.2. Conditions for the creation of canard cycles at the corner ....	37
2.4. Discussion .....	47
3. Relaxation Oscillations in an Idealized Ocean Circulation Model .....	49
3.1. Introduction .....	49

3.2.	Stommel's Model .....	51
3.3.	Dynamic Oscillations with 1 Slow Variable .....	55
3.3.1.	Globally Attracting Critical Manifold .....	57
3.3.2.	Bistable Critical Manifold .....	59
3.4.	Separating the Forcing Terms .....	60
3.4.1.	The Critical Manifold .....	62
3.4.2.	The Reduced Problem and Singularities .....	63
3.4.3.	Strategy .....	66
3.4.4.	Evidence of Stable Relaxation Orbit .....	72
3.4.5.	Lack of a Periodic Orbit with only One Relaxation Phase ...	73
3.5.	Discussion .....	76
4.	Mixed-mode Oscillations in a Conceptual Climate Model .....	78
4.1.	Introduction .....	78
4.2.	Setting up the Model .....	82
4.3.	Analyzing the System .....	88
4.3.1.	The Layer Problem .....	89
4.3.2.	The Reduced Problem .....	90
4.3.3.	Strategy .....	93
4.3.4.	Folded Node Conditions .....	94
4.3.5.	Estimate of the Funnel .....	96
4.3.6.	Singular Periodic Orbit .....	101
4.3.7.	Main Result .....	105
4.4.	Discussion .....	107
5.	Conclusion .....	112
5.1.	Non-smooth Canards .....	112

5.2. Relaxation Oscillations in Ocean Models .....	113
5.3. MMOs in a Climate Based Model .....	114
5.4. Future Work .....	115
REFERENCES .....	116



## LIST OF FIGURES

1.1.	Oxygen isotope data from Greenland (NGRIP) .....	5
1.2.	Temperature record depicting interglacial periods .....	6
1.3.	Temperature record depicting the Mid-Pleistocene transition .....	7
1.4.	Relaxation Oscillation .....	12
2.1.	Example of a ‘2’ shaped critical manifold. ....	18
2.2.	Fast and slow dynamics leading to canard explosion in the smooth case. ....	20
2.3.	Examples of the three types of singular canard cycles .....	22
2.4.	Depiction of the quasi-canard explosion. ....	31
2.5.	Relative slopes of vectors as discussed in the proof of Lemma 2.3.1. ...	35
2.6.	The set $V$ for a given $\lambda$ .....	37
2.7.	Images characterizing a nonsmooth canard explosion for $\epsilon = 0.2$ .....	38
2.8.	An example of a set $W$ which is positively invariant .....	40
2.9.	The stable orbit of a super-explosion (blue) for $\epsilon = 0.2$ .....	42
2.10.	Positively invariant sets .....	43
2.11.	Important sets for the proof of Proposition 2.3.8 .....	46
3.1.	Oxygen isotope data from Greenland (NGRIP) .....	51
3.2.	Graphs of (3.6) for (a) $A < 1$ and (b) $A > 1$ . ....	54
3.3.	Bifurcation diagram for (3.4) .....	55
3.4.	Possible phase spaces of (3.10) for $A < 1$ and $1 + a \neq b$ .....	58
3.5.	Oscillatory behavior in (3.12). ....	61
3.6.	Example of a singular periodic orbit .....	66
3.7.	Existence of a stable singular periodic orbit .....	67
3.8.	Regions of phase space that satisfy conditions (a)-(e). ....	74
3.9.	Example of the 3D stable periodic orbit .....	75

4.1.	Temperature record depicting interglacial periods .....	79
4.2.	Energy balance .....	84
4.3.	Cubic approximation of (4.10) .....	87
4.4.	Example of a singular periodic orbit .....	92
4.5.	A lower bound for the edge of the funnel. ....	98
4.6.	Locally invariant regions on the critical manifold .....	102
4.7.	Parameters that will produce an MMO orbit .....	106
4.8.	MMO orbit .....	107
4.9.	More parameters that could produce MMOs .....	108
4.10.	Examples of MMO patterns in the three time-scale case. ....	109
4.11.	Another MMO orbit .....	110

## CHAPTER 1

### Introduction

#### 1.1. Overview

Different mechanisms affect the Earth's climate on very different time scales: from the 5-year El Niño cycles, to the Atlantic Multidecadal Oscillation, to the Milankovitch cycles with periods on the order of 10 millennia. Dynamical systems with variables that change on dramatically different time scales are called fast/slow systems. This thesis examines the role of fast/slow dynamics in understanding the mechanisms behind oscillatory patterns found in paleoclimate data. The intuitive approach to analyzing systems with multiple time scales is to analyze the dynamics on each time scale separately. In doing so, the fast dynamics may be attracted to an apparent equilibrium, however the equilibrium can be destabilized by the slow dynamics. Because full fast/slow system remains in this state for a long time, it is called a *metastable state*. Fast/slow systems often exhibit rapid transitions between metastable states, and understanding these transitions is important in climate science. However, these rapid changes in the state of the system implicitly require examining trajectories that enter a region of phase space where the basic theory used to analyze fast/slow systems no longer applies. The content of this thesis examines the non-standard behavior arising from the break down of the theory, typically appearing in the form of small amplitude oscillations.

Chapter 1 discusses the dynamical systems techniques that have been used to analyze oscillations in climate data and introduces the theory used to analyze fast/slow systems. Chapters 2-4 are each intended to be stand-alone work, addressing a different problem in the theory of fast/slow systems or its applications to climate science.

Chapter 2 focuses on special behavior, called canard phenomena, in piecewise-smooth, planar systems, demonstrating conditions under which a piecewise-smooth, planar system exhibits small oscillations called canard cycles. Additionally, the dynamics are analyzed in the event that the conditions for canard cycles are not met, showing the existence of *super-explosion* behavior in piecewise-smooth, nonlinear systems. Chapter 3 applies the results of Chapter 2 to a large-scale ocean circulation model that reduces to a system with 1 fast and 1 slow variable. A more complicated model with 1 fast and 2 slow variables is also analyzed, examining the consequences of a cusp catastrophe in large-scale ocean circulation. Chapter 4 explores the role of fast/slow dynamics in glacial-interglacial cycles of the past 400,000 years (400 kyr). A smooth model with 1 fast and 2 slow variables is analyzed, showing the existence of mixed-mode oscillations due to a generalized canard phenomenon. Chapter 5 summarizes the work of the previous chapters and discusses future directions of research.

## 1.2. Oscillations in Climate Data

The Earth's climate is an ever-changing system, and it is not always a simple task to understand what causes the variability. In his book, Cronin [11] distinguishes two causes of climate change: external forcing and internal processes. Cronin also discusses how both of these causes are viewed differently in climatology versus paleoclimatology. However, from both the climatological and paleoclimatological viewpoints, examining feedback mechanisms is an integral part of understanding how the causes of climate change create the observed effect. Feedback mechanisms either amplify or dampen the effects of external forcing and internal processes. In many cases, feedbacks destabilize a metastable climate state, causing an abrupt transition to another state. Often, the destabilization is thought of as a bifurcation in some underlying subsystem. The metastable climate state is an attracting equilibrium of this underlying system, and it loses stability as a parameter is varied. After the bifurcation, trajectories are quickly attracted to another attracting equilibrium. This is often described as a *hysteresis*, because the system does not respond immediately

to the varying parameter. That is, a large variation in the parameter can lead to a small change in the dynamics.

Nonlinear dynamical systems techniques, especially those designed to analyze systems with multiple time scales, can be particularly effective in providing an understanding of how feedback mechanisms function. Crucifix [12] surveys applications of these techniques to conceptual paleoclimate models, emphasizing oscillations in the climate system that can be seen as stable periodic orbits of an underlying dynamical system. One particular mechanism that Crucifix discusses is the *relaxation oscillation*.

In a fast/slow system, a relaxation oscillation is a periodic orbit that involves a fast relaxation to a meta-stable equilibrium. The meta-stable equilibrium slowly loses stability until it becomes unstable. Once the system is unstable, it quickly relaxes to another meta-stable state. In this sense, a relaxation oscillation is very closely related to a hysteresis loop. A hysteresis loop is described by two (or more) bifurcations. The system starts in a stable state, and as a parameter is increased, this equilibrium slowly becomes less stable. Once it becomes unstable (through a bifurcation), the system rapidly equilibrates to a different stable state. Then, as the parameter is decreased, the new state becomes unstable. The system transitions back to the original stable state, creating the hysteresis loop. On the surface, the distinction between a hysteresis loop and a relaxation oscillation appears to be a matter of terminology. A hysteresis loop results from slowly varying a parameter past bifurcation points; a relaxation oscillation depends on a slow variable that evolves according to specified equations. However, the inclusion of a bifurcation parameter as a slow variable, even when included in such a way as to cause the metastable states to destabilize, does not guarantee the system will have a relaxation oscillation. For some parameter ranges, the system will have a stable small-amplitude periodic orbit called a *canard cycle*. Canard cycles form the “intervening oscillations” referenced in the title of this thesis.

While there are many other important problems involving oscillations in the climate system, this work will focus on two particular oscillations: Dansgaard-Oeschger events and glacial-interglacial cycles. As will be made explicit, both of these oscillations exhibit relaxation behavior.

**1.2.1. Dansgaard-Oeschger Events.** Over the last 100 kyr, the North Atlantic climate has undergone a series of millennial scale oscillations [13]. These oscillations, known as Dansgaard-Oeschger (D-O) events, are characterized by a rapid warming ( $\sim 10^\circ \text{C}$  over a few decades) followed by a longer cooling period, with the average period of a full cycle being approximately 1.5 kyr. Evidence of D-O events was first discovered in Greenland ice core proxy data, depicted in Figure 1.1. Additional proxy data in other areas of the globe suggest these events impacted the climate in Antarctica and China [50], however the temperature variation is less dramatic with smaller magnitude and more gradual fluctuation away from the North Atlantic. This imbalance indicates that D-O events are associated with a change in the Earth's primary heat distribution system, the ocean. As the ocean transports heat from the North Atlantic to the much larger South Atlantic, and eventually the Pacific, the warm water passes through the colder deep ocean. The increased volume and cooler temperatures of these regions cause dissipation of heat and a large timescale for the global response.

The correlation between D-O events and ocean circulation has caused scientists to focus on oscillations in the Atlantic Meridional Overturning Circulation (AMOC). In his classical paper, Stommel [61] demonstrates the bistability of the AMOC. In Stommel's model, there is a parameter range in which the ocean has two stable states: (1) a strong circulation transporting warm, salty water from the equator to the pole along the surface (sometimes called a positive circulation) as well as (2) a reverse circulation state that transports cold water from the pole to the equator along the surface (called a negative circulation). Between those states, there is also a weak positive circulation that is unstable.

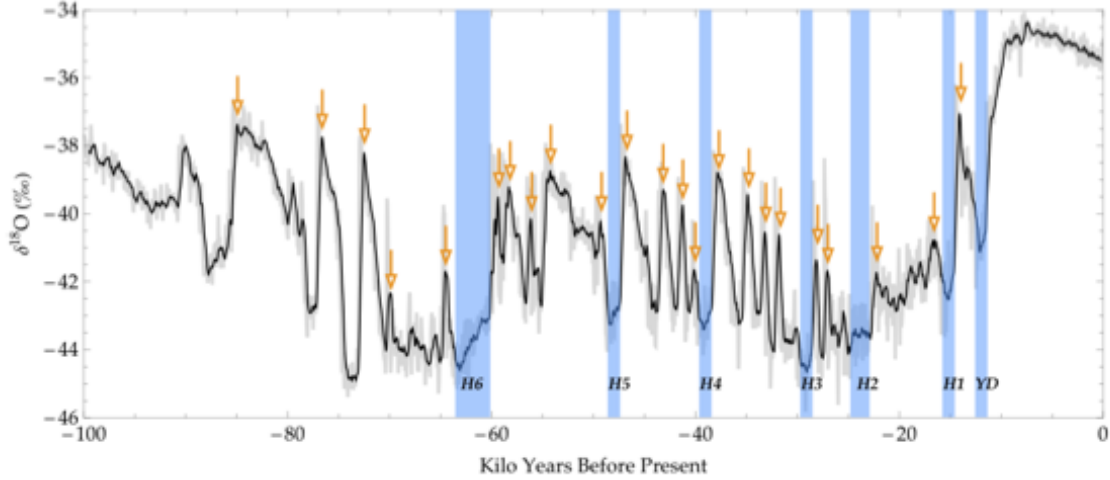


FIGURE 1.1. Oxygen isotope data from Greenland (NGRIP). Orange arrows indicate thermal maxima of Dansgaard-Oeschger cycles over the last 100,000 years. Figure courtesy of Saha [50].

The bifurcation parameter in Stommel’s model is the ratio of temperature forcing to salinity forcing. Scientists have taken a variety of approaches to dynamically explain the transition between circulation states; Dijkstra and Ghil survey many of these approaches in [17]. Some mechanisms trigger the oscillations through periodic [24] or stochastic [7] fluctuations in freshwater (i.e., salinity) forcing. Saltzman *et al.* generate oscillations through stochastic changes in thermal forcing combined with feedback mechanisms in the model. Still other models generate oscillations through convective sinking that occurs when the vertical stratification of the ocean becomes unstable [8, 9, 10] through feedback mechanisms in the intrinsic ocean dynamics. Saha’s model [50] also has oscillations caused by periodic convective sinking, although the unstable stratification is created through feedbacks with sea-ice formation and melting.

Creating a transition between stable circulation states is not the only challenge when modeling D-O events. The rapid warming events clearly exhibit relaxation behavior and indicate the presence of multiple time-scales in an underlying mathematical model. However, the longer cooling period creates an asymmetric oscillatory

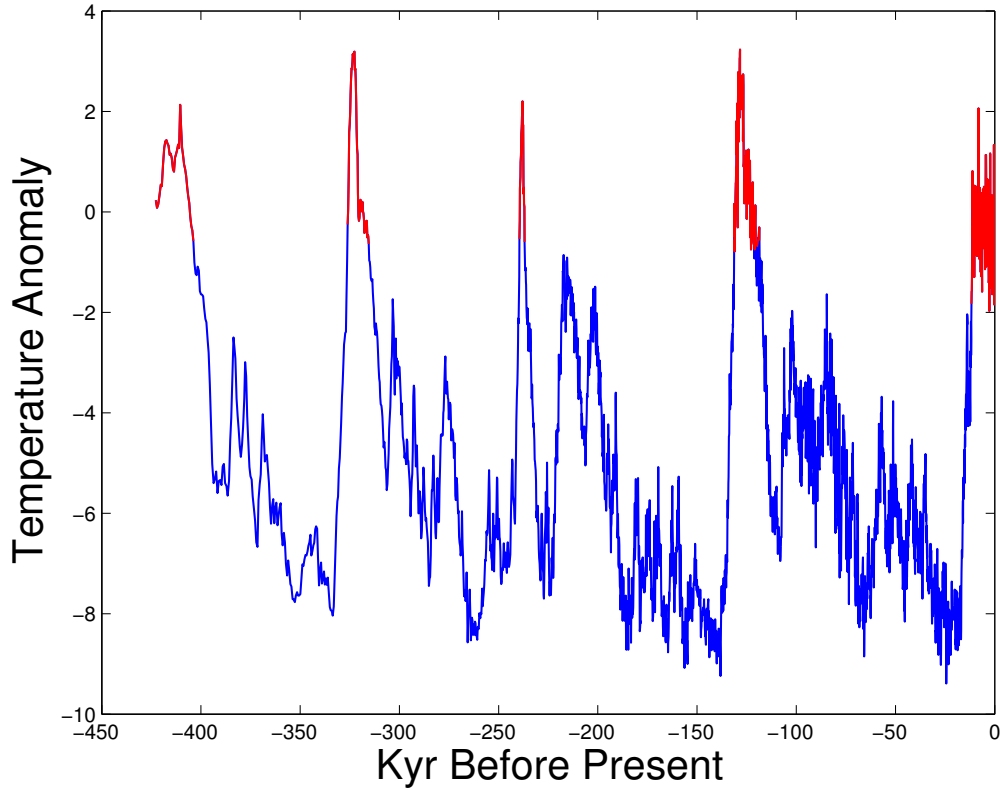


FIGURE 1.2. Temperature record depicting interglacial periods [43].

pattern. Chapter 3 discusses a mechanism by which the state of the ocean dynamically affects the state of the atmosphere through changes in the evaporation rate near the equator. The asymmetry is addressed through a non-smooth vector field. The non-smooth nature of the vector field results from an absolute value term that is intrinsic to large-scale ocean circulation models that allow for a reverse circulation.

**1.2.2. Glacial-Interglacial Cycles.** The Antarctic glacial-interglacial cycles of the last 400 kyr provide another example in which fast/slow dynamical systems techniques can be applied in climate science. Proxy data shown in Figure 1.2 also indicates rapid warming events characteristic of relaxation behavior. However, between each of the large amplitude spikes there are a series of small amplitude oscillations, providing a more complicated oscillatory pattern than can be understood by relaxation oscillations.



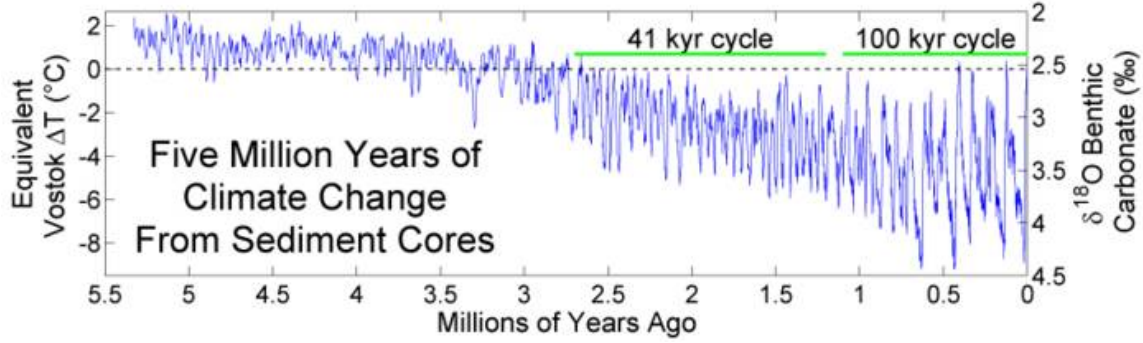


FIGURE 1.3. Temperature record depicting the Mid-Pleistocene transition [39].

A major goal of paleoclimatology has been to explain a shift from oscillations with a dominant period of 41 kyr to the 100 kyr cycles depicted in Figure 1.2. This shift is called the Mid-Pleistocene Transition (MPT) and it can be seen in the extended proxy data shown in Figure 1.3. Maasch and Saltzman have a series of papers attempting to explain the MPT, focusing on a dynamic Hopf bifurcation [52, 53, 54]. Paillard and Parrenin develop a piecewise-linear model with a Heaviside function to simulate the transition between glacial and interglacial states [42]. Hogg also develops a piecewise-smooth model that incorporates  $\text{CO}_2$  feedback [28]. All of these models rely on Milankovitch forcing—changes in solar forcing due to variation in the Earth’s orbit—to generate oscillations. However, the analysis of the last 400 kyr centers around explaining the dominant 100 kyr period and does not adequately describe the smaller oscillations between large spikes. Chapter 4 of this thesis addresses the small amplitude oscillations using the theory of mixed-mode oscillations (MMOs), incorporating a relaxation oscillation and more complicated behavior into a single attracting periodic orbit.

### 1.3. Geometric Singular Perturbation Theory

From the relaxation behavior depicted in Figures 1.1 and 1.2 it is clear there are climate processes that operate on multiple time-scales. Systems with multiple time

scales take the form

$$(1.1) \quad \begin{aligned} x' &= f(x, y, \epsilon) \\ y' &= \epsilon g(x, y, \epsilon), \end{aligned} \quad x \in \mathbb{R}^n, \quad y \in \mathbb{R}^m, \quad 0 < \epsilon \ll 1,$$

where  $f, g$  are  $C^k$  functions for some  $k \geq 1$  and the prime denotes differentiation with respect to the time variable  $t$  (i.e.  $' = d/dt$ ). The system (1.1) should be dimensionless, and the small parameter  $\epsilon$  should relate to physical parameters of the full system with dimensions. Here  $x$  is called the fast variable and  $y$  is called the slow variable. The technique used here to analyze systems of the form (1.1), called *geometric singular perturbation theory* (GSP), was first developed by Fenichel [20, 21, 22, 23]. Intuitively, one can think of analyzing the fast ( $x$ ) and slow ( $y$ ) dynamics separately, and GSP provides the rigorous means of connecting them together.

Rescaling time by a nonzero scalar value does not change the paths of trajectories in phase space, only the speed at which the paths are traced. The system (1.1) is called the fast system, and rescaling time by a factor of  $\epsilon$  produces the slow system

$$(1.2) \quad \begin{aligned} \epsilon \dot{x} &= f(x, y, \epsilon) \\ \dot{y} &= g(x, y, \epsilon), \end{aligned} \quad x \in \mathbb{R}^n, \quad y \in \mathbb{R}^m, \quad 0 < \epsilon \ll 1.$$

Here the dot denotes differentiation with respect to the new time variable  $\tau = \epsilon t$  (i.e.  $\dot{\phantom{x}} = d/d\tau$ ). The systems (1.1) and (1.2) are equivalent as long as  $\epsilon > 0$ , however much can be gained from looking at the limits of these systems as  $\epsilon \rightarrow 0$ .

As  $\epsilon \rightarrow 0$ , (1.1) becomes

$$(1.3) \quad \begin{aligned} x' &= f(x, y, 0) \\ y' &= 0, \end{aligned}$$

and (1.2) becomes

$$(1.4) \quad \begin{aligned} 0 &= f(x, y, 0) \\ \dot{y} &= g(x, y, 0), \end{aligned}$$

so the systems are no longer equivalent. Because the  $\epsilon = 0$  limits of (1.1) and (1.2) are different, this is a singular perturbation problem and the limit  $\epsilon \rightarrow 0$  is called the *singular limit*.

The singular limit of the fast dynamics (1.3) is called the *layer problem*, and here the  $y$  dynamics are trivial. Thus the layer problem can either be viewed as a dynamical system in  $\mathbb{R}^n$ , where the  $m$ -vector  $y$  can be thought of as a parameter vector, or as a dynamical system in  $\mathbb{R}^{(n+m)}$  as written in (1.3). The set

$$M_0 = \{f(x, y, 0) = 0\}$$

is the set of critical points of (1.3) and is called the *critical manifold*. Calling  $M_0$  a manifold is justified (in cases of interest here) by the Implicit Function Theorem, which states that there is a  $C^k$  function  $h$  such that  $\{f(x, y, 0) = 0\} = \{x = h(y)\}$  locally, as long as  $\det(\partial f / \partial x) \neq 0$ . Note that  $M_0$  may be a manifold with boundary.

In (1.4) the dynamics are only defined on the set given by the algebraic condition  $\{f(x, y, 0) = 0\}$ , so the critical manifold  $M_0$  is again an important set. That is, (1.4) defines a dynamical system on the  $m$ -dimensional manifold  $M_0$ . Because the dynamical system is defined on a lower dimensional manifold than the full system (1.1) (or equivalently, (1.2)), (1.4) is called the *reduced problem*.

The intuition behind GSP is to allow the layer problem to equilibrate to some point on  $M_0$ , and then follow the slow dynamics on  $M_0$  as defined by the reduced problem. This intuitive picture provides a caricature of the full dynamics given by the system (1.1) (or equivalently, (1.2)) for  $\epsilon > 0$ . GSP says this intuitive approach is correct away from degenerate points where

$$\det \left( \frac{\partial f}{\partial x} \right) \bigg|_{p \in M_0} = 0.$$

This non-degeneracy condition is called *normal hyperbolicity*, and it guarantees that the manifold of critical points  $M_0$  will be hyperbolic (i.e., have no eigenvalues  $\lambda$  such that  $\text{Re}(\lambda) = 0$ ) with respect to the  $n$ -dimensional fast dynamics. The following

theorem is due to Fenichel and begins to provide rigorous justification for the desired intuitive approach [30].

**THEOREM 1.3.1.** *If  $\epsilon > 0$  is sufficiently small, and  $M_0$  is a normally hyperbolic, compact manifold (possibly with boundary), then*

- (1)  $M_0$  perturbs to a slow manifold  $M_\epsilon$  which lies within  $\mathcal{O}(\epsilon)$  of  $M_0$ ,
- (2)  $M_\epsilon$  is  $C^k$ , including in  $\epsilon$ ,
- (3)  $M_\epsilon$  is diffeomorphic to  $M_0$ , and
- (4)  $M_\epsilon$  is locally invariant under the flow (1.1).

In the  $(n+m)$ -dimensional system (1.3) the normally hyperbolic critical points on  $M_0$  will have an  $m$ -dimensional 0-eigenspace. These  $m$  dimensions correspond to the  $m$  dimensions of the critical manifold. Since  $M_0$  is a set of critical points, it must be contained in a center manifold—an invariant set containing a critical point in which there is no exponential decay to the critical point in forward or reverse time. Since the reduced problem defines the dynamics on  $M_0$ , it is essentially describing dynamics on a center manifold. The relationship between slow dynamics and behavior on a center manifold is one of the key concepts that led to the development of GSP. Indeed, this relationship leads to important distinctions between  $M_0$  and  $M_\epsilon$ .  $M_0$  is unique in that it is a set of equilibria of a dynamical system. Furthermore, the concepts of stable and unstable manifolds to  $M_0$ , denoted  $W^s(M_0)$  and  $W^u(M_0)$  respectfully, are natural to discuss. Because  $M_\epsilon$  is no longer a set of equilibria for  $\epsilon > 0$ , as a center manifold it is no longer unique. Additionally,  $M_\epsilon$  does not come equipped with stable and unstable manifolds *a priori*, therefore it is not obvious that the intuitive concept of “letting the fast dynamics equilibrate” has any rigorous justification. However, another theorem due to Fenichel provides this justification [30].

**THEOREM 1.3.2.** *If  $\epsilon > 0$  but sufficiently small, and  $M_0$  is (locally) normally hyperbolic, then*

- (1) *there exist manifolds  $W^s(M_\epsilon)$  and  $W^u(M_\epsilon)$  that lie within  $\mathcal{O}(\epsilon)$  of  $W^s(M_0)$  and  $W^u(M_0)$ , respectively,*
- (2)  *$W^s(M_\epsilon)$  and  $W^u(M_\epsilon)$  are  $C^k$*
- (3)  *$W^s(M_\epsilon)$  and  $W^u(M_\epsilon)$  are diffeomorphic to  $W^s(M_0)$  and  $W^u(M_0)$ , respectively, and*
- (4)  *$W^s(M_\epsilon)$  and  $W^u(M_\epsilon)$  are locally invariant under the flow (1.1).*

*Furthermore, the terminology “stable” and “unstable” manifolds are justified. That is, there exist a neighborhood  $D$  of  $M_0$ , and constants  $\kappa_s > 0$  and  $\alpha_s < 0$  such that if  $v \in W^s(M_\epsilon)$  and  $v \cdot [0, t] \subset D$ , with  $t > 0$ , then*

$$d(v \cdot t, M_\epsilon) \leq \kappa_s \exp(\alpha_s t).$$

*Similarly, there exist constants  $\kappa_u > 0$  and  $\alpha_u > 0$  such that if  $v \in W^u(M_\epsilon)$  and  $v \cdot [t, 0] \subset D$ , with  $t < 0$ , then*

$$d(v \cdot t, M_\epsilon) \leq \kappa_u \exp(\alpha_u t).$$

#### 1.4. Relaxation Oscillations, Fold Points, and Canards

Of course, much of the scientifically interesting behavior in a fast/slow system occurs where GSP theory breaks down, and this is the case in a relaxation oscillation. In the terminology of the previous section, a relaxation oscillation can be constructed from a singular periodic orbit—that is a periodic orbit in the singular limit that consists of trajectories from both the layer problem and the reduced problem. An example in the case where  $n = m = 1$  is depicted in Figure 1.4. The relaxation behavior is provided by a trajectory of the layer problem equilibrating to an attracting branch of  $M_0$ . The slow loss of stability occurs as the dynamics of the reduced problem send trajectories toward an extremum of the critical manifold.

A necessary component of a relaxation oscillation is a folded critical manifold [33, 34]. A *fold* is a co-dimension 1 subset  $\mathcal{F}$  of the critical manifold where the manifold is attracting on one side and repelling on the other. A necessary consequence

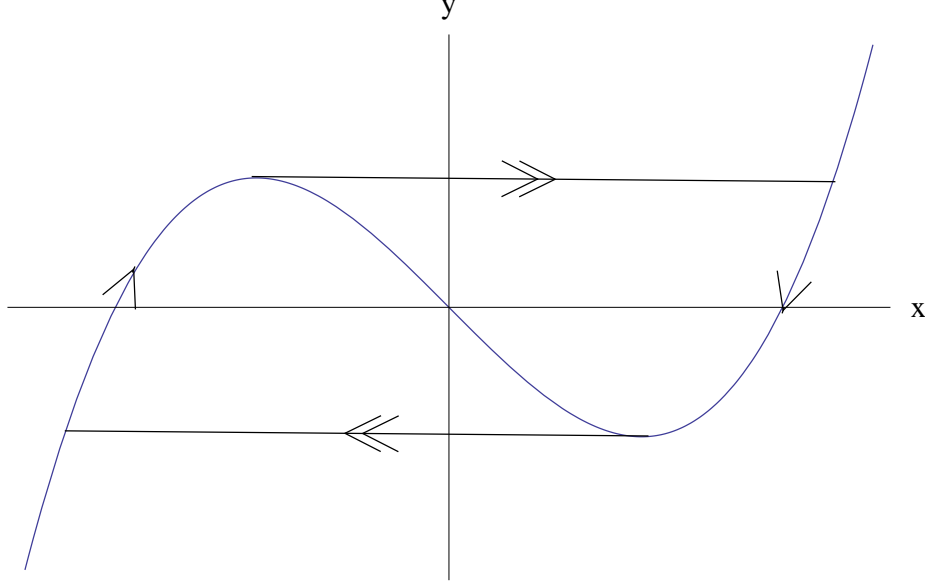


FIGURE 1.4. Relaxation oscillation. Oscillation pictured in the singular limit with an ‘S’-shaped critical manifold. The outer branches (where the curve is increasing) are stable, the middle branch is unstable. The double arrows indicate fast dynamics of the layer problem (relaxation behavior). The single arrows represent slow dynamics of the reduced problem.

is that for all  $p \in \mathcal{F}$ ,

$$\det \left( \frac{\partial f}{\partial x} \right) \Big|_p = 0.$$

Geometrically, a fold is a set where the critical manifold is tangent to trajectories of the layer problem. Therefore, along the fold, the fast and slow dynamics are tangent. Since the critical manifold cannot be written as  $\{x = h(y)\}$  at the fold, it is a singular set of the slow dynamics. The most common types of fold points are called *regular fold points*. At a regular fold point, the slow dynamics point toward the fold on both sides or away from the fold on both sides, so the fold point is an essential singularity [33]. A system containing regular fold points where the slow dynamics are directed toward can produce relaxation oscillations since trajectories will reach the sets where metastable states become unstable [34, 63].

In planar systems, there is a special type of fold point called a *canard point*. A *nullcline* is a set where the variation in a particular variable is trivial. For example, in (1.1), the  $y$  nullcline (or slow nullcline) is the set where  $g(x, y, \epsilon) = 0$ . A canard point

occurs when the slow nullcline intersects the critical manifold at the fold. When this happens, the slow dynamics point toward the fold on one side and away from the fold on the other. Because of this, a canard point is a removable singularity of the slow dynamics, and trajectories of the reduced problem may cross the fold from the stable branch of  $M_0$  to the unstable branch (or vice versa) [33]. Such a trajectory is called a *singular canard*, and it perturbs to canard solutions for  $\epsilon > 0$ .

‘Canard’ is a French word with two meanings. The literal translation in English is ‘duck,’ however canard can also mean ‘hoax’ or ‘deception.’ Somehow, both translations are appropriate when discussing canards in the mathematical sense. One definition of a canard solution—sometimes called the *maximal canard*—is a trajectory that lies in the intersection of a repelling slow manifold and an attracting slow manifold [33, 34]. A more inclusive definition of a canard solution is a trajectory that remains near a repelling slow manifold for  $\mathcal{O}(1)$  time. More precisely, the ratio of time spent near repelling slow manifolds to time spent near attracting slow manifolds is  $\mathcal{O}(1)$ . The existence of a canard solution can lead to a phenomenon known as *canard explosion*, whereby a system undergoes a rapid transition from a small limit cycle to relaxation oscillations through a series of canard cycles [3, 18, 19].

The singular canard cycles, built by a combination of pieces of  $M_0$  and transitions between different branches of  $M_0$ , often look like cartoon ducks (see Figure 2.3d), as in the case of the Van der Pol system. This is the reason the French mathematicians, who first discovered canard cycles, decided to call them ‘canards.’ In planar systems, the canard explosion phenomenon occurs in an exponentially small range of parameters, making canard cycles hard to detect. Because of this difficulty, canard trajectories were misunderstood for a long time. Additionally, it is extremely difficult, if not impossible, to verify their existence in physical experiments.

In smooth, planar systems there have been three methods used to analyze the canard phenomenon. It was first discovered by Benoit *et al* [3] using nonstandard analysis. Then Eckaus examined canards through the lens of matched asymptotic

expansions [19]. More recently, the popular mechanism for analyzing canards has been a combination of blow-up and dynamical systems techniques. This idea was introduced by Dumortier and Roussarie [18] and generalized by Krupa and Szmolyan [33, 34].

The popularity of the blow-up technique is largely due to the fact that it generalizes readily to higher-dimensional systems [62]. In higher dimensions, the analog of a canard point is a *folded equilibrium*. A folded equilibrium is not the projection of an equilibrium solution of (1.1) onto  $M_0$ , but rather results from desingularizing the slow dynamics so that they are defined along the fold  $\mathcal{F}$ . Certain types of folded equilibria, namely folded nodes, folded saddles, and folded saddle-nodes, result in singular canard orbits [14, 35, 62, 67]. In planar systems, the singular canard may only exist for one particular parameter value, so the effect of a singular canard is hardly seen away from the singular limit. In higher dimensions, a folded equilibrium may produce more than one singular canard orbit, and these orbits exist for a much larger parameter range. Because of this, canard phenomena (such as mixed-mode oscillations) are much more robust in higher dimensions.

This realization cast canards in a new light, spurring the increase of interest in canards over the last decade. Once canards were viewed as somehow being artificial—nuisances that would disappear under small perturbations. Now, canards are understood as a possible mechanism for producing more complicated behavior such as mixed-mode oscillations [4, 14]. Indeed, canard trajectories through a folded node are essential to the analysis of the model for glacial-interglacial cycles in Chapter 4—to our knowledge this is the first application of the theory of mixed-mode oscillations to a climate model.

In the last few years, the renewed interest in canards has caused mathematicians to examine canard phenomena in non-smooth systems [15, 44], however the research has been limited to piecewise-linear systems. There are significant differences between



canards in smooth systems and what are called *quasi-canards* in piecewise-linear systems. First, in the smooth case the explosion phase does not begin immediately upon bifurcation as it does in the piecewise-linear case. Second, during the explosion, the amplitudes of the periodic orbits in smooth systems grow exponentially, compared to the linear, albeit rapid, growth in the piecewise-linear case. Finally, the shape of the periodic quasi-canard orbits does not change during the explosion. In the smooth canard explosion, the maximal canard causes the periodic orbits to develop an inflection point. This is due to the existence of a strongly repelling slow manifold, an existence that depends on the nonlinearity of the vector field. The focus of Chapter 2 is on canard phenomena in a piecewise-smooth, planar, fast/slow system that is nonlinear. As in the case of smooth systems, a bifurcation occurs as the slow nullcline passes through the extremum of the critical manifold. Conditions are found under which such canard cycles are created from this bifurcation, and in nonlinear piecewise-smooth systems, the canard trajectories resemble smooth canards much more than quasi-canards. If these conditions are not met, the system will bifurcate from having a stable equilibrium to having a relaxation oscillation. This transition happens instantaneously, forgoing the canard explosion. This behavior, called super-explosion, was first discovered by Desroches *et al.* in piecewise-linear systems in [15]. A key development of this thesis is demonstrating super-explosion behavior in nonlinear piecewise-smooth systems as well as the possibility of a subcritical super-explosion (where the relaxation oscillation appears before the bifurcation).

Canards will play a central role in the remainder of this thesis. Chapter 2 presents theoretical results on canard phenomena in planar, piecewise-smooth systems. Chapter 3 applies these results to a thermohaline circulation model used to study D-O events. Chapter 4 relates glacial-interglacial cycles to mixed-mode oscillations.

## CHAPTER 2

# Canard-like Phenomena in Piecewise-Smooth Planar Systems

### 2.1. Introduction

In dynamical systems, a canard is a trajectory of a fast/slow system that remains near a repelling slow manifold for  $\mathcal{O}(1)$  time. In smooth, planar systems, a Hopf bifurcation may occur when the slow nullcline transversely intersects a fold (i.e. local extrema) of the fast nullcline, also called the *critical manifold*. If the fast nullcline is ‘S’-shaped, the Hopf cycles will grow to become relaxation oscillations. Canard cycles bridge the gap of the transition from Hopf cycles to relaxation oscillations, which happens in an exponentially small parameter range. Due to the rapid growth of the amplitudes of the periodic orbits, this phenomenon is called a *canard explosion*.

The theory used to analyze fast/slow systems is called geometric singular perturbation theory (GSP). For an introduction to GSP, we direct the reader to the paper by Jones [30]. In general, GSP theory breaks down at fold points of the critical manifold because the fast and slow dynamics become tangent (i.e. there is no separation of time scales locally). If the fast and slow nullclines do not intersect at a fold, then the fold point is an essential singularity of the reduced problem. At a Hopf bifurcation, however, the fold point becomes a removable singularity of the reduced problem and is called a *canard point* [33]. In the singular limit, a canard point allows trajectories to cross from a stable branch of the critical manifold to an unstable branch of the critical manifold (or vice versa). If the system is no longer smooth, but instead only piecewise smooth, the analog of a canard point may no longer be a removable singularity.

The generic nonsmooth, continuous dynamical system can be written as

$$(2.1) \quad \dot{z} = \begin{cases} F_L(z) & \text{on } \{h(z) \leq 0\} \\ F_R(z) & \text{on } \{h(z) \geq 0\} \end{cases}$$

where  $z \in \mathbb{R}^k$  and there exists an  $n$  such that

$$\left. \frac{d^n F_L}{dz^n} \right|_{\{h(z)=0\}} \neq \left. \frac{d^n F_R}{dz^n} \right|_{\{h(z)=0\}}.$$

The co-dimension one set of discontinuities of the  $n^{\text{th}}$  derivative (i.e.,  $\{h(z) = 0\}$ ) is called the *splitting manifold*. We will consider the specific case of planar fast/slow systems where  $n = 1$  and  $k = 2$ . In particular, we consider a nonlinear, piecewise-smooth Liénard system:

$$(2.2) \quad \begin{aligned} \dot{x} &= -y + F(x) \\ \dot{y} &= \epsilon(x - \lambda) \end{aligned}$$

where

$$F(x) = \begin{cases} g(x) & x \leq 0 \\ h(x) & x \geq 0 \end{cases}$$

with  $g, h \in C^r$ ,  $r \geq 1$ ,  $g(0) = h(0) = 0$ ,  $g'(0) < 0$  and  $h'(0) > 0$ , and we assume that  $h$  has a maximum at  $x_M > 0$ . The critical manifold

$$N_0 = \{y = F(x)\}$$

is ‘S’-shaped with a smooth fold at  $x_M$  and a corner (i.e., nonsmooth fold) along the splitting line  $x = 0$ . An example of such a critical manifold is shown in Figure 2.1. When  $\lambda = 0$  in (2.2), the slow nullcline passes through the corner of the critical manifold creating the analog of a canard point. There is still a ‘Hopf-like’ bifurcation at  $\lambda = 0$ , with a stable equilibrium existing for  $\lambda < 0$  and a stable periodic orbit for  $\lambda > 0$ , however the nonsmooth ‘canard point’ is no longer a removable singularity of the reduced problem.

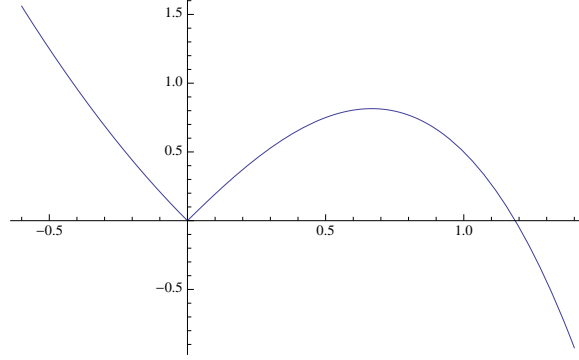


FIGURE 2.1. Example of a ‘2’ shaped critical manifold.

Nonsmooth systems are interesting in two ways: (1) the similarities they share with smooth systems or (2) the ways they differ from smooth systems. This paper addresses both of those issues with regard to systems of the form (2.2). First, we find conditions under which (2.2) exhibits canard phenomena similar to its smooth counterpart. Second, we describe the dynamics when those conditions are not met.

Recently, mathematicians have begun to consider the possibility of canard-like phenomena in nonsmooth systems [15], [44], [47], however the work to this point has been restricted to piecewise-linear systems. The smooth canard explosion phenomenon involves an interplay of local dynamics near a canard point and global dynamics leading to a periodic orbit. The examination of piecewise-linear systems is a large step in understanding the local dynamics near a nonsmooth fold, however it cannot account for the nonlinear global behavior. Indeed, nonlinearity is required for the transition from small canard cycles to the larger canards with heads (see Figure 2.3). We generalize the analysis to nonlinear, piecewise-smooth systems of the form (2.2).

In [15], Desroches *et al.* perform the local analysis near a nonsmooth canard point in a piecewise linear system. In doing so, they discover a new phenomenon—a nonsmooth bifurcation called a *super-explosion*. Under a super-explosion, the system bifurcates from having a stable equilibrium instantaneously into relaxation oscillations, forgoing the small canard cycles. We find this phenomenon in the nonlinear,

piecewise-smooth case as well, however our more general setting allows us to demonstrate a sub-critical super-explosion—the simultaneous existence of a stable equilibrium and a stable relaxation oscillation.

The method of proof employs a *shadow system*, or smooth system that agrees with (2.2) on one side of the splitting line. In most cases we will use

$$(2.3) \quad \begin{aligned} \dot{x} &= -y + h(x) \\ \dot{y} &= \epsilon(x - \lambda) \end{aligned}$$

as our shadow system. For  $x > 0$ , the systems (2.2) and (2.3) agree. It is often useful to consider a trajectory with initial conditions in the right half-plane, following the flow until the trajectory hits the splitting line  $\{x = 0\}$ . At this point, the vector fields no longer coincide, so the trajectory will behave differently in (2.2) than it will in (2.3). We will compare the different behavior for  $x < 0$ , utilizing what is known about canard cycles in smooth systems.

In Section 2.2 we provide the relevant background material required to prove the main results. In Section 2.3 we state and prove the main results about the existence or lack of canard cycles in nonsmooth systems. Finally, we conclude with a discussion in Section 2.4.

## 2.2. Background

In this section we provide the necessary background material that we will use to prove the results in Section 3.

**2.2.1. Canards in smooth, planar systems.** We begin by discussing the existing theory relating to canards in two dimensions. There are multiple approaches to demonstrating the existence of canard cycles in planar systems. Since the blow-up techniques of Krupa and Szmolyan [33, 34] have become standard, we use their statements of the theorems here.

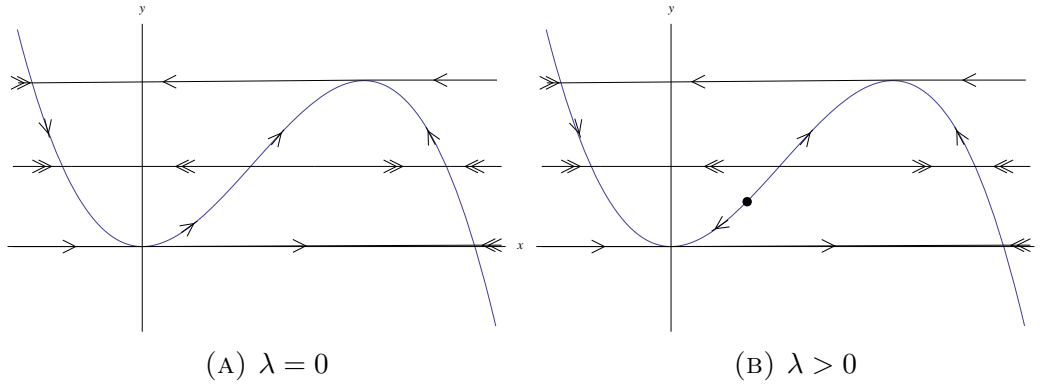


FIGURE 2.2. Fast and slow dynamics leading to canard explosion in the smooth case.

Consider a one-parameter family of singularly perturbed systems in the form

$$(2.4) \quad \begin{aligned} x' &= f(x, y, \lambda, \epsilon) \\ y' &= \epsilon g(x, y, \lambda, \epsilon) \end{aligned} \quad x \in \mathbb{R} \quad y \in \mathbb{R} \quad 0 < \epsilon \ll 1,$$

where  $f, g$  are  $C^k$  function with  $k \geq 3$  and  $\cdot = d/dt$ . For the system to undergo a canard explosion, (2.4) must satisfy a series of assumptions.

(A1) The critical manifold,  $S = \{f(x, y, \lambda, 0) = 0\}$  is ‘S’-shaped. That is, it can be written in the form  $y = \phi(x)$ , where  $\phi$  has precisely two critical points: a non-degenerate local maximum, and a non-degenerate local minimum. Without loss of generality, we assume that the minimum occurs at the origin and the maximum occurs for some  $x = x_M > 0$ . Then, the critical manifold can be broken into three pieces,  $S_l$ ,  $S_m$ , and  $S_r$ —left, middle, and right, respectively—separated by the local extrema of  $\phi$ . These three pieces are:

$$S^l = \{(x, \phi(x)) : x < 0\}$$

$$S^m = \{(x, \phi(x)) : 0 < x < x_M\}$$

$$S^r = \{(x, \phi(x)) : x > x_M\}.$$

(A2) In the layer problem, the outer branches  $S_l$  and  $S_r$  are attracting, and the middle branch  $S_m$  is repelling. That is,

$$\begin{aligned}\frac{\partial f}{\partial x}\Big|_{S^{l,r}} &< 0, \text{ and} \\ \frac{\partial f}{\partial x}\Big|_{S^m} &> 0.\end{aligned}$$

(A3) For some value  $\lambda = \lambda_0$  one of the folds is a non-degenerate canard point. Without loss of generality, we assume this happens for  $\lambda_0 = 0$  and for the fold point at the origin (i.e. the fold connecting  $S^l$  and  $S^m$ ).

Similar to (A2), the assumptions (A1) and (A3) can also be expressed in terms of partial derivatives. The condition that  $(0,0)$  is a fold point as well as a singularity when  $\lambda = 0$  gives us

$$f(0,0,0,0) = 0, \quad \frac{\partial f}{\partial x}(0,0,0,0) = 0, \quad g(0,0,0,0) = 0,$$

along with the non-degeneracy assumptions

$$\frac{\partial^2 f}{\partial x^2}(0,0,0,0) \neq 0, \quad \frac{\partial f}{\partial y}(0,0,0,0) \neq 0.$$

Also, for the canard point to be non-degenerate we get the conditions

$$\frac{\partial g}{\partial x}(0,0,0,0) \neq 0, \quad \frac{\partial g}{\partial \lambda}(0,0,0,0) \neq 0.$$

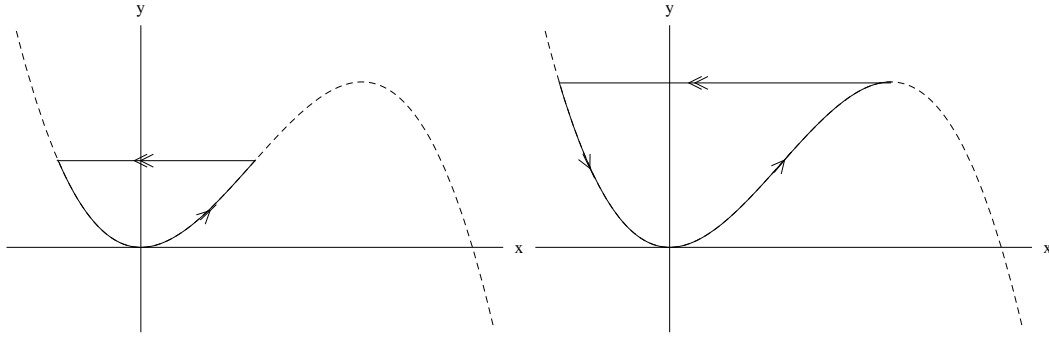
Finally, there is one last assumption required for the canard explosion theorems.

(A4) When  $\lambda = 0$ , the dynamics of the reduced problem have  $\dot{x} < 0$  on  $S^r$  and  $\dot{x} > 0$  on  $S^l \cup \{0\} \cup S^m$ .

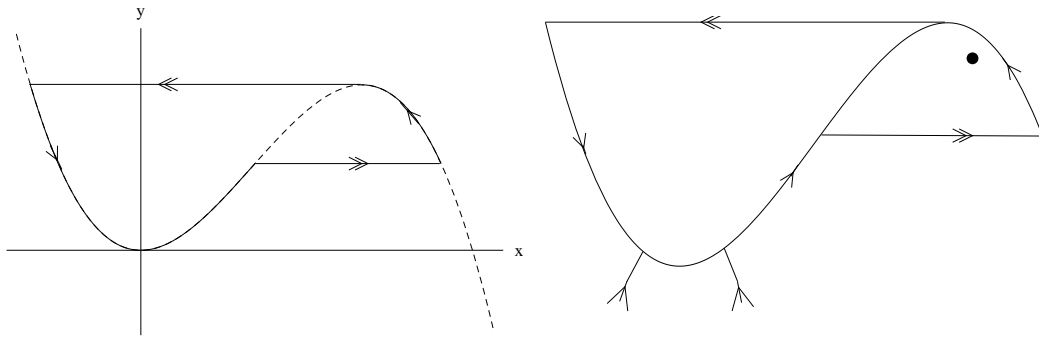
The flow in the reduced problem is given by the equation

$$(2.5) \quad \dot{x} = \frac{g(x, \phi(x), \lambda, 0)}{\phi'(x)}.$$

Note that when  $\lambda = 0$ , the right-hand side of (2.5) is smooth at the origin, and assumptions (A1)-(A4) imply that the fast and slow dynamics appear as in Figure



(A) Singular canard cycle  $\Gamma(s)$ ,  $s \in (0, y_M)$ . (B) Singular canard cycle  $\Gamma(s)$ ,  $s = y_M$ .



(C) Singular canard cycle  $\Gamma(s)$ ,  $s \in (y_M, 2y_M)$ . (D) A duck!

FIGURE 2.3. Examples of the three types of singular canard cycles: (a) canard without head, (b) maximal canard, and (c) canard with head.

2.2a. Directly calculating eigenvalues of the Jacobian shows that  $\lambda = 0$  is precisely when (2.4) undergoes a Hopf bifurcation. When  $\lambda = 0$ , the slow nullcline passes through fold, creating the canard point. In [34], Krupa and Szmolyan show that for some  $\lambda > 0$  (as in Figure 2.2b) the system (2.4) exhibits relaxation oscillations. The canard explosion is the rapid transition from the small periodic orbits created through the Hopf bifurcation to the large relaxation oscillation. This is shown through a family of singular periodic orbits  $\Gamma(s)$ , which we now describe.

Set  $\lambda = 0$  and define  $y_M = \phi(x_M)$ . For  $s \in (0, y_M)$  let  $x_l(s) < x_m(s) < x_r(s)$  be the roots of  $\phi(x) = s$  (i.e., the  $x$ -coordinates of the intersections of the line  $y = s$  with the critical manifold  $S$ ). For completeness, define  $x_l(0) = 0 = x_m(0)$  and



$x_m(y_M) = x_M = x_r(y_M)$ . We can now define  $\Gamma(s)$  piecewise for  $s \in [0, 2y_M]$ . First,

$$\Gamma(s) = \{(x, \phi(x)) : x \in [x_l(s), x_m(s)]\} \cup \{(x, s) : x \in [x_l(s), x_m(s)]\}, \text{ for } s \in [0, y_M].$$

This is a singular orbit like the one in Figure 2.3a (for  $s \neq y_M$ ), often referred to as a “canard without head.” Next,

$$\begin{aligned} \Gamma(s) = & \{(x, \phi(x)) : x \in [x_l(y_M), x_m(2y_M - s)]\} \\ & \cup \{(x, 2y_M - s) : x \in [x_m(2y_M - s), x_r(2y_M - s)]\} \\ & \cup \{(x, \phi(x)) : x \in [x_M, x_r(2y_M - s)]\} \\ & \cup \{(x, y_M) : x \in [x_l(y_M), x_M]\} \\ & \text{for } s \in [y_M, 2y_M]. \end{aligned}$$

In the second case (for  $s \neq y_M$ ),  $\Gamma(s)$  traces out an orbit like the one in Figure 2.3c, beginning at the left-most point and following the arrows in the directions indicated in the figure. Orbits of this type are called “canards with head.” When  $s = y_M$ , we get the maximal canard as shown in Figure 2.3b.

The idea behind the canard explosion theorems is explained by Krupa and Sz-molyan [34] as being

“to obtain a family  $\Gamma(s, \epsilon)$  of canard cycles existing for corresponding parameter values  $\lambda = \lambda(s, \epsilon)$  as a perturbation of the degenerate family  $\Gamma(s)$ ,  $\lambda = 0$  which exists for  $\epsilon = 0$ . As  $s$  sweeps through a suitable interval of the family of canard cycles  $\Gamma(s, \epsilon)$  connects the Hopf bifurcation to relaxation oscillations and canard explosion takes place.”

Near the non-degenerate canard point, there is a canonical form for (2.4):

$$\begin{aligned} (2.6) \quad x' &= -yh_1(x, y, \lambda, \epsilon) + x^2h_2(x, y, \lambda, \epsilon) + \epsilon h_3(x, y, \lambda, \epsilon) \\ y' &= \epsilon[xh_4(x, y, \lambda, \epsilon) - \lambda h_5(x, y, \lambda, \epsilon) + yh_6(x, y, \lambda, \epsilon)], \end{aligned}$$

where

$$\begin{aligned} h_3(x, y, \lambda, \epsilon) &= \mathcal{O}(x, y, \lambda, \epsilon) \\ h_j(x, y, \lambda, \epsilon) &= 1 + \mathcal{O}(x, y, \lambda, \epsilon), \quad j = 1, 2, 4, 5. \end{aligned}$$

Define the constants

$$\begin{aligned} a_1 &= \frac{\partial h_3}{\partial x}(0, 0, 0, 0), \quad a_2 = \frac{\partial h_1}{\partial x}(0, 0, 0, 0), \quad a_3 = \frac{\partial h_2}{\partial x}(0, 0, 0, 0), \\ a_4 &= \frac{\partial h_4}{\partial x}(0, 0, 0, 0), \quad a_5 = h_6(0, 0, 0, 0), \end{aligned}$$

and

$$(2.7) \quad A = -a_2 + 3a_3 - 2a_4 - 2a_5.$$

Finally, we define the function  $R(s)$ , which is called the “way in-way out” function in [3]. Similar to  $\Gamma(s)$ , we define  $R(s)$  for  $s \in [0, 2y_M]$ , but differently for  $s > y_M$  or  $s < y_M$ . We have

$$R(s) = \int_{x_l(s)}^{x_m(s)} \frac{\partial f}{\partial x}(x, \phi(x), 0, 0) \frac{\phi'(x)}{g(x, \phi(x), 0, 0)} dx \quad \text{for } s \in [0, y_M],$$

and

$$\begin{aligned} R(s) &= \int_{x_l(s)}^{x_m(2y_M-s)} \frac{\partial f}{\partial x}(x, \phi(x), 0, 0) \frac{\phi'(x)}{g(x, \phi(x), 0, 0)} dx \\ &+ \int_{x_r(2y_M-s)}^{x_M} \frac{\partial f}{\partial x}(x, \phi(x), 0, 0) \frac{\phi'(x)}{g(x, \phi(x), 0, 0)} dx \quad \text{for } s \in [y_M, 2y_M]. \end{aligned}$$

We are now ready to state the theorems of canard explosion. The first theorem describes the Hopf bifurcation, out of which the small canard cycles are born [34].

**THEOREM 2.2.1.** *Suppose (A1)-(A4) hold. Then there exist  $\epsilon_0 > 0$  and  $\lambda_0 > 0$  such that for each  $0 < \epsilon < \epsilon_0$  and each  $|\lambda| < \lambda_0$ , the system (2.4) has precisely one equilibrium  $p_e$  which converges to the canard point as  $(\epsilon, \lambda) \rightarrow 0$ . Moreover, there exists a curve  $\lambda_H(\sqrt{\epsilon})$  such that  $p_e$  is stable for  $\lambda < \lambda_H(\sqrt{\epsilon})$  and loses stability through*

a Hopf bifurcation as  $\lambda$  passes through  $\lambda_H(\sqrt{\epsilon})$ . The curve  $\lambda_H(\sqrt{\epsilon})$  has the expansion

$$\lambda_H(\sqrt{\epsilon}) = -\frac{a_1 + a_5}{2}\epsilon + \mathcal{O}(\epsilon^2).$$

The Hopf bifurcation is non-degenerate if  $A$  is nonzero. It is supercritical if  $A < 0$  and subcritical if  $A > 0$ .

The second theorem proves the existence of maximal canards. A maximal canard is a trajectory that connects a stable slow manifold to an unstable slow manifold. This happens precisely when slow manifolds  $S_\epsilon^l$  and  $S_\epsilon^m$  change their relative position. The existence of the slow manifolds is guaranteed by Fenichel theory, however they are, in general, not unique. In [33] it is demonstrated that the lack of uniqueness does not pose a problem in demonstrating the existence of a unique maximal canard.

**THEOREM 2.2.2.** *Suppose that (A1)-(A4) hold. Then there exists a smooth function  $\lambda_c(\sqrt{\epsilon})$  such that a solution starting in  $S_\epsilon^l$  connects to  $S_\epsilon^m$  if and only if  $\lambda = \lambda_c(\sqrt{\epsilon})$ . The function  $\lambda_c$  has the expansion*

$$\lambda_c(\sqrt{\epsilon}) = -\left(\frac{a_1 + a_5}{2} + \frac{1}{8}A\right)\epsilon + \mathcal{O}(\epsilon^{3/2}).$$

Theorem 2.2.2 is a result about local behavior near a canard point, and is proved using blow-up techniques in [33]. It is included here, as in [34], because it guarantees the existence of a maximal canard. Away from the singular limit, slow manifolds do not extend to the fold point (under Fenichel's theorems) due to the loss of normal hyperbolicity. Since they are invariant under the flow, however, slow manifolds can be extended using the flow—although the stability of the extensions may not hold. While the attracting and repelling branches of the critical manifold intersect at the fold in the singular limit, the extended slow manifolds may not intersect. Generically, one of the extended slow manifolds will lie above the other in the plane. The maximal canard occurs precisely when the attracting and repelling slow manifolds switch their relative positions, causing the transition from headless canard cycles to canards with heads. This transition is essential to the description of a canard explosion.

THEOREM 2.2.3. Fix  $\epsilon_0$  sufficiently small and  $v \in (0, 1)$ . Assume (A1)-(A4) hold, and assume  $A < 0$ . For  $\epsilon \in (0, \epsilon_0)$  there exists a family of periodic orbits

$$s \rightarrow (\lambda(s, \sqrt{\epsilon}), \Gamma(s, \sqrt{\epsilon})), \quad s \in (0, 2y_M)$$

which is  $C^k$  smooth in  $(s, \sqrt{\epsilon})$ , and such that

- (i) for  $s \in (0, \epsilon^v)$  the orbit  $\Gamma(s, \sqrt{\epsilon})$  is attracting and uniformly  $\mathcal{O}(\epsilon^v)$  close to the canard point and  $\lambda(s, \sqrt{\epsilon})$  is strictly increasing in  $s$ ,
- (ii) for  $s \in (2y_M - \epsilon^v, 2y_M)$  the orbit  $\Gamma(s, \sqrt{\epsilon})$  is a relaxation oscillation and  $\lambda(s, \sqrt{\epsilon})$  is strictly increasing in  $s$ ,
- (iii) if  $s \in [\epsilon^v, 2y_M - \epsilon^v]$ , then  $|\lambda(s, \sqrt{\epsilon}) - \lambda_c(\sqrt{\epsilon})| \leq e^{-1/\epsilon^{1-v}}$ ;
- (iv) as  $\epsilon \rightarrow 0$ , the family  $\Gamma(s, \sqrt{\epsilon})$  converges uniformly in Hausdorff distance to  $\Gamma(s)$ ;
- (v) any periodic orbit passing sufficiently close to the critical manifold  $S$  is a member of the family  $\Gamma(s, \sqrt{\epsilon})$  or a relaxation oscillation.

Theorem 2.2.3 guarantees a canard explosion takes place in the situation of a sub-critical Hopf bifurcation, so we can define the functions  $\lambda_s(\sqrt{\epsilon}) = \lambda(\epsilon^v, \sqrt{\epsilon})$  and  $\lambda_r(\sqrt{\epsilon}) = \lambda(2y_M - \epsilon^v, \sqrt{\epsilon})$ , which mark the beginning and end of the canard explosion. The subscripts  $s$  and  $r$  stand for *small* and *relaxation* cycles, respectively. The stability of the orbits and the monotonicity of the  $\lambda_j(s, \sqrt{\epsilon})$  depends on  $R(s)$ . For more information and figures of these curves, we direct the reader to Krupa and Szmolyan's work [34].

THEOREM 2.2.4. If the assumptions of Theorem 2.2.3 hold and  $R(s) < 0$  for all  $s \in (0, y_M]$ , then all canard cycles are stable and the functions  $\lambda_j$  (where  $j = H, s, c$ , or  $r$ ) are monotonic in  $s$ .

Next we state the theorems for the subcritical case,  $A > 0$ .

**THEOREM 2.2.5.** *Fix  $\epsilon_0$  sufficiently small and  $v \in (0, 1)$ . Assume (A1)-(A4) hold, and assume  $A > 0$ . For  $\epsilon \in (0, \epsilon_0)$  there exists a family of periodic orbits*

$$s \rightarrow (\lambda(s, \sqrt{\epsilon}), \Gamma(s, \sqrt{\epsilon})), \quad s \in (0, 2y_M)$$

*which is  $C^k$  smooth in  $(s, \sqrt{\epsilon})$ , and such that*

- (i) for  $s \in (0, \epsilon^v)$  the orbit  $\Gamma(s, \sqrt{\epsilon})$  is repelling and uniformly  $\mathcal{O}(\epsilon^v)$  close to the canard point and  $\lambda(s, \sqrt{\epsilon})$  is strictly increasing in  $s$ ,*
- (ii) for  $s \in (2y_M - \epsilon^v, 2y_M)$  the orbit  $\Gamma(s, \sqrt{\epsilon})$  is a relaxation oscillation and  $\lambda(s, \sqrt{\epsilon})$  is strictly increasing in  $s$ ,*
- (iii) if  $s \in [\epsilon^v, 2y_M - \epsilon^v]$ , then  $|\lambda(s, \sqrt{\epsilon}) - \lambda_c(\sqrt{\epsilon})| \leq e^{-1/\epsilon^{1-v}}$ ;*
- (iv) as  $\epsilon \rightarrow 0$ , the family  $\Gamma(s, \sqrt{\epsilon})$  converges uniformly in Hausdorff distance to  $\Gamma(s)$ ;*
- (v) any periodic orbit passing sufficiently close to the critical manifold  $S$  is a member of the family  $\Gamma(s, \sqrt{\epsilon})$  or a relaxation oscillation.*

The curves  $\lambda_s$  and  $\lambda_r$  are defined the same in the case of the subcritical Hopf bifurcation, however, the orientation of all of the  $\lambda_j$  curves is reversed [34].

**2.2.2. Quasi-canards in Piecewise Linear Systems.** In [15], Desroches *et al.* consider a piecewise-linear fast/slow Liénard system of the form:

$$(2.8) \quad \begin{aligned} x' &= -y + f(x) \\ y' &= \epsilon(x - \lambda), \end{aligned}$$

where

$$f(x) = \begin{cases} -x, & x < 0, \\ kx, & 0 \leq x \leq 2, \\ -x + 2(k+1), & x > 2, \end{cases}$$

where  $k > 0$  is a constant. Note that we have reoriented the system to correspond with the set-up from the previous subsection on smooth canards. To make this relationship more explicit, we have  $x_M = 2$ . Although the  $S$  in  $S^j$  denoting the various branches of the critical manifold in the smooth case from the previous section likely represents

the ‘S’-shape of the manifold, we will think of it as representing the smoothness. In a similar manner, we define

$$L^l = \{(x, f(x)) : x < 0\}$$

$$L^m = \{(x, f(x)) : 0 < x < 2\}$$

$$L^r = \{(x, f(x)) : x > 2\},$$

where the  $L$  stands for linear. The system will always have an equilibrium point at  $(\lambda, f(\lambda))$ . It is easy to check that for  $\lambda < 0$  (and  $\lambda > 2$ ) the equilibrium is stable. When  $0 < \lambda < 2$ , the equilibrium is unstable and Poincaré-Bendixson guarantees the existence of a stable periodic orbit. This is especially easy to see in the singular limit, and is not significantly more difficult for  $\epsilon > 0$ . Thus, when  $\lambda = 0$  (and  $\lambda = 2$ ), there must be a bifurcation by which the periodic orbits are created as  $\lambda$  increases (resp. decreases) through the bifurcation value. The main result of [15] characterizes this bifurcation.

Since the system is piecewise-linear,  $f'(x)$  is constant in each linear zone. That is,

$$f'(x) = \begin{cases} -1, & x < 0, \\ k, & 0 \leq x \leq 2, \\ -1, & x > 2. \end{cases}$$

Therefore, for fixed  $\epsilon$ , the eigenvalues of the system are also constant in each linear zone. A quick computation shows that the eigenvalues for an equilibrium on  $L^l$  or  $L^r$  are

$$\lambda_{\pm} = \frac{-1 \pm \sqrt{1 - 4\epsilon}}{2},$$

so for  $\epsilon \leq 1/4$ , the critical points will be nodes. Otherwise they will be stable foci. For an equilibrium on  $L^m$ , the eigenvalues are

$$\lambda_{\pm} = \frac{k \pm \sqrt{k^2 - 4\epsilon}}{2},$$

and the type of equilibrium (unstable focus or unstable node) is determined by the sign of  $k^2 - 4\epsilon$ .

**THEOREM 2.2.6.** *In the system (2.8), for  $0 < \epsilon \leq \frac{1}{4}$  and  $k > 0$  fixed, the following statements hold:*

- (i) *For  $\lambda < 0$  the equilibrium is globally asymptotically stable and, therefore, it is the global attractor of the system.*
- (ii) *For  $\lambda = 0$ , the equilibrium point is always the global attractor of the system; it is globally asymptotically stable when  $k^2 - 4\epsilon < 0$  (the focus case), but it is unstable for  $k^2 - 4\epsilon > 0$  (the node case). The instability of this latter case comes from the existence of a bounded continuum of homoclinic orbits to the equilibrium point, the most external homoclinic orbit defined by the unstable invariant manifold that coincides for  $0 \leq x \leq 2$  with the straight line*

$$y = \frac{k - \sqrt{k^2 - 4\epsilon}}{2}x$$

*and eventually coming back to the equilibrium, approaching it tangentially to the straight line*

$$y = -\frac{1 + \sqrt{1 - 4\epsilon}}{2}x$$

- (iii) *For  $0 < \lambda < 2$ , the equilibrium point is unstable and surrounded by a unique stable limit cycle.*

(a) *When  $k^2 - 4\epsilon \geq 0$  (the node case), the limit cycle always has points in each of the three linearity zones.*

(b) *When  $k^2 - 4\epsilon < 0$  (the focus case) the limit cycle is born of a “Hopf-like” bifurcation at  $\lambda = 0$ . The limit cycle only has points in the two linear zones meeting along the splitting line  $x = 0$  when  $\lambda > 0$  and small. In this case, if the peak-to-peak amplitude  $\alpha$  of the limit cycle is measured by taking its two intersections with the line  $x = 0$ , then  $\alpha(\lambda)$  is a linear function of  $\lambda$  as long as the limit cycle does not enter the third linear zone. More precisely, there exist*

two positive constants  $\lambda_G(k, \epsilon)$  and  $m(k, \epsilon)$  such that

$$\alpha(\lambda) = m(k, \epsilon) \cdot \lambda$$

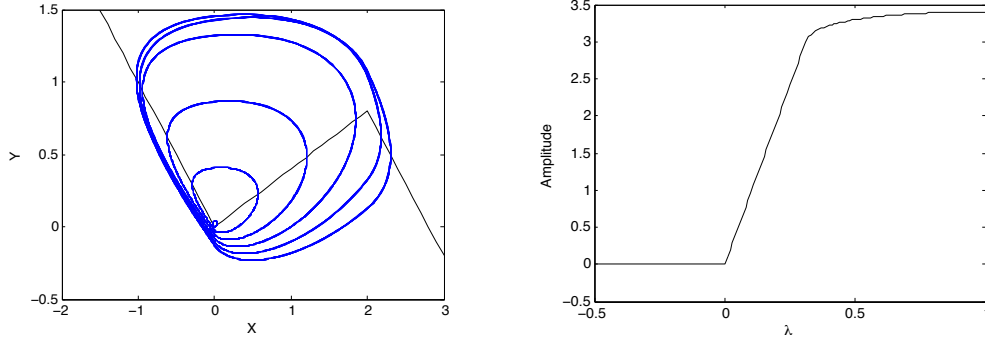
for  $0 < \lambda < \lambda_G$ . Furthermore, the length of the linear range  $\lambda_G$  and the linear growth rate  $m$  satisfy

$$\lim_{k \rightarrow 2\sqrt{\epsilon}^-} \lambda_G = 0 \quad \text{and} \quad \lim_{k \rightarrow 2\sqrt{\epsilon}^-} m = +\infty.$$

As the theorem states, the two possibilities for the bifurcation are (iii)(a) a transition from a stable node to an unstable node or (iii)(b) a transition from a stable node to an unstable focus. In the first case, the system transitions from having a globally attracting equilibrium to relaxation oscillations without undergoing anything resembling the canard explosion described in the previous subsection. Desroches *et al.* [15] coin the term *super-explosion* to describe this instantaneous jump. In the latter case,  $\lambda_G$  corresponds to  $\lambda_c$  in that it is the value of  $\lambda$  for which the stable periodic orbit intersects the local maximum of the critical manifold  $\{y = f(x)\}$ . In contrast to the smooth canard explosion (for the supercritical Hopf case), the “explosion” phase in the piecewise-linear case occurs immediately upon bifurcation and stops at  $\lambda_G$  (see Figure 2.4b). The subscript  $G$  denotes that this occurs precisely at the value of  $\lambda$  for which a grazing bifurcation occurs—this is, the value of  $\lambda$  for which the stable periodic orbit is tangent to the splitting line  $x = 2$ .

The piecewise-linear case as presented in [15] and the smooth case differ in some interesting ways. One difference is that in the piecewise linear case, Fenichel theory no longer guarantees the existence of a repelling slow manifold. The eigenvalue associated with the fast dynamics is an  $\mathcal{O}(\sqrt{\epsilon})$  constant in the middle linearity zone, precluding the clear separation of time scales required to have a repelling slow manifold. For this reason, Desroches *et al.* distinguish the trajectories that remain near the repelling branch of the critical manifold by calling them quasi-canards instead of canards. As a consequence of not having a repelling slow manifold, the quasi-canard cycles





(A) Canard cycles in the piecewise linear system (2.8) with  $k = 0.4$ ,  $\epsilon = 0.2$ . (B) Growth of amplitudes of periodic orbits as  $\lambda$  increases.

FIGURE 2.4. Depiction of the quasi-canard explosion.

never develop heads—the singular canard with head in smooth systems is depicted in Figure 2.3c. The inclusion of a fourth linear zone, one with a strongly repelling slow manifold between  $L^m$  and  $L^r$ , is enough to produce canards with heads [47]. Another important distinction, which was not discussed in [15], is the possibility of subcritical “Hopf-like” bifurcations. As we will see, it is possible to have a quasi-canard cycle or relaxation oscillation appear before the equilibrium loses stability, however this relies on the slope of  $L^l$  being sufficiently small.

**2.2.3. Nonsmooth Hopf Bifurcations.** Finally, we introduce the last big piece of the puzzle, a criterion for determining when a nonsmooth Hopf bifurcation is sub- or super-critical. Unlike the complicated criterion for smooth Hopf bifurcations that relies on third order mixed partials [25], Simpson and Meiss showed that the criterion for nonsmooth Hopf bifurcations is astoundingly simple [60].

The main result from [60] considers a planar, piecewise- $C^k$ , continuous system of ODEs with  $k \geq 1$  of the form

$$(2.9) \quad \dot{z} = \begin{cases} F_L(x, y; \lambda), & x \leq 0 \\ F_R(x, y; \lambda), & x \geq 0 \end{cases},$$

where  $z = (x, y) \in \mathbb{R}^2$ .

THEOREM 2.2.7. *Suppose that the vector field (2.9) is continuous and piecewise  $C^k$ ,  $k \geq 1$ , in  $(x, y, \lambda)$  and has an equilibrium that transversely crosses a one-dimensional switching manifold when  $\lambda = 0$  at a point  $z^*$  where the manifold is  $C^k$ . Suppose further that as  $\lambda \nearrow 0$  the eigenvalues of the equilibrium approach  $\mu_u \pm i\omega_u$  and as  $\lambda \searrow 0$  they approach  $-\mu_s \pm i\omega_s$ , where  $\mu_u, \mu_s, \omega_u, \omega_s > 0$ . Define*

$$\Lambda = \frac{\mu_u}{\omega_u} - \frac{\mu_s}{\omega_s}.$$

*Then if  $\Lambda < 0$  there exists an  $\epsilon > 0$  such that for all  $0 < \lambda < \epsilon$  there is an attracting periodic orbit whose radius is  $\mathcal{O}(\lambda)$  away from  $z^*$ , and for  $-\epsilon < \lambda < 0$  there are no periodic orbits near  $z^*$ .*

*If, on the other hand,  $\Lambda > 0$ , there exists an  $\epsilon > 0$  such that for all  $-\epsilon < \lambda < 0$  there is repelling periodic orbit whose radius is  $\mathcal{O}(\lambda)$  away from  $z^*$ , and for all  $0 < \lambda < \epsilon$  there are no periodic orbits near  $z^*$ .*

### 2.3. Main Results

As we state and prove our main results, we will consider systems of the form

$$(2.10) \quad \begin{aligned} \dot{x} &= -y + F(x) \\ \dot{y} &= \epsilon(x - \lambda) \end{aligned}$$

where

$$F(x) = \begin{cases} g(x) & x \leq 0 \\ h(x) & x \geq 0 \end{cases}$$

and the following assumptions hold

- (I)  $g, h \in C^k$ ,  $k \geq 1$ ,
- (II)  $g(0) = h(0) = 0$ ,
- (III)  $g'(0) < 0$ ,
- (IV)  $h'(0) > 0$ ,
- (V) and  $h$  has a maximum at  $x_M > 0$ .

The critical manifold

$$N_0 = \{y = F(x)\}$$

is ‘S’-shaped with a smooth fold at  $x_M$  and a corner along the splitting line  $x = 0$ .

As for the smooth and piecewise linear cases, we denote

$$N^l = \{(x, F(x)) : x < 0\} = \{(x, g(x)) : x < 0\}$$

$$N^m = \{(x, F(x)) : 0 < x < x_M\} = \{(x, h(x)) : 0 < x < x_M\}$$

$$N^r = \{(x, F(x)) : x > x_M\} = \{(x, h(x)) : x > x_M\}.$$

We will assume that  $h(x)$  can be extended into the region where  $x < 0$  and define the shadow system to be

$$(2.11) \quad \begin{aligned} \dot{x} &= -y + h(x) \\ \dot{y} &= \epsilon(x - \lambda). \end{aligned}$$

Since there are two distinct types of bifurcation that can lead to the formation of periodic orbits—one at the smooth fold and one at the corner—we will consider each of those cases separately. In both cases, we will consider the relative distance from the origin of trajectories in the nonsmooth system (2.10) and shadow system (2.11) that enter the left half-plane  $x < 0$  at the same point  $(0, y_*)$ . The following lemma describes the relationship of these trajectories.

LEMMA 2.3.1. *Consider the trajectory  $\gamma_n(t) = (x_n(t), y_n(t))$  of (2.10) that crosses the  $y$ -axis entering the left half-plane  $x < 0$  at  $\gamma_n(0) = (0, y_c)$ . Also consider the analogous trajectory  $\gamma_s$  of the shadow system (2.11). The condition on the slopes of  $g, h$  at 0 in (2.10) guarantee that  $g(x) > h(x)$  for some range of  $x$ 's where  $x < 0$ . Assume  $g(x) > h(x)$  arbitrarily far into the left half-plane. Then, the distance from the origin of  $\gamma_n$  is bounded by that of  $\gamma_s$ .*

PROOF. Define

$$R(x, y) = \frac{x^2 + y^2}{2}.$$

$R$  will evolve differently in the nonsmooth and shadow systems when  $x < 0$ , so we denote  $\dot{R}_n(x, y)$  and  $\dot{R}_s(x, y)$  as the time derivative of  $R$  in the nonsmooth and shadow systems, respectively. Then we have

$$\dot{R}_n(x, y) = x(g(x) - y) + \epsilon y(x - \lambda)$$

$$\dot{R}_s(x, y) = x(h(x) - y) + \epsilon y(x - \lambda).$$

Therefore, at a given point  $(x, y)$  where  $x \leq 0$ , we have

$$\dot{R}_n(x, y) - \dot{R}_s(x, y) = x[g(x) - h(x)] \leq 0,$$

since  $g(x) \geq h(x)$ , where equality only holds if  $x = 0$ . Thus,  $\gamma_n$  can never cross  $\gamma_s$  moving away from the origin for  $x < 0$  (i.e., in the left half-plane the vector field of (2.10) points “inward” on the trajectory  $\gamma_s$ ). Since  $\gamma_n$  and  $\gamma_s$  coincide at  $(0, y_c)$ , it suffices to show that  $R(\gamma_n(\delta t)) < R(\gamma_s(\delta t))$  for  $\delta t > 0$  sufficiently small. Since the vector fields of (2.10) and (2.11) coincide on the  $y$ -axis, we must use second order terms:

$$\begin{pmatrix} x_n(\delta t) \\ y_n(\delta t) \end{pmatrix} = \begin{pmatrix} 0 + \dot{x}_n \delta t + \ddot{x}_n \delta t^2 \\ y_c + \dot{y}_n \delta t + \ddot{y}_n \delta t^2 \end{pmatrix}$$

$$\begin{pmatrix} x_s(\delta t) \\ y_s(\delta t) \end{pmatrix} = \begin{pmatrix} 0 + \dot{x}_s \delta t + \ddot{x}_s \delta t^2 \\ y_c + \dot{y}_s \delta t + \ddot{y}_s \delta t^2 \end{pmatrix}.$$

We have already seen that  $(x_s(t), y_s(t))$  and  $(x_n(t), y_n(t))$  agree for the  $0^{th}$  and  $1^{st}$  order terms. Therefore, the important terms are

$$\ddot{x}_n = -\dot{y}_n + g'(0)\dot{x}_n = \epsilon\lambda - g'(0)y_c$$

$$\ddot{x}_s = -\dot{y}_s + h'(0)\dot{x}_s = \epsilon\lambda - h'(0)y_c$$

and

$$\ddot{y}_n = \epsilon\dot{x}_n = -\epsilon y_c$$

$$\ddot{y}_s = \epsilon\dot{x}_s = -\epsilon y_c.$$

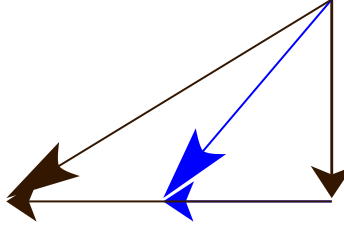


FIGURE 2.5. Relative slopes of vectors as discussed in the proof of Lemma 2.3.1.

Both vector fields point left ( $\dot{x} < 0$ ) if and only if  $y > 0$ , so  $y_c$  must be positive. Since  $\ddot{y}$  is the same in both systems, we look at the  $\ddot{x}$  terms. Since  $-g'(0) > 0 > -h'(0)$ , the smooth trajectory of the shadow system moves further left than the nonsmooth trajectory for the same vertical change as in Figure 2.5. This shows that the trajectory of the nonsmooth system enters the left half-plane immediately below (i.e., nearer to the origin than) the trajectory of the shadow system. Once  $\gamma_n$  is nearer to the origin than  $\gamma_s$ , it is bounded by  $\gamma_s$ , proving the result.  $\square$

**COROLLARY 2.3.2.** *Consider the trajectory  $\gamma_n(t) = (x_n(t), y_n(t))$  of (2.10) that crosses the  $y$ -axis entering the left half-plane  $x < 0$  at  $\gamma_n(0) = (0, y_c)$ . Also consider the analogous trajectory  $\gamma_s$  of the system*

$$(2.12) \quad \begin{aligned} \dot{x} &= -y + \tilde{F}(x) \\ \dot{y} &= \epsilon(x - \lambda) \end{aligned}$$

where

$$\tilde{F}(x) = \begin{cases} \tilde{g}(x) & x \leq 0 \\ h(x) & x \geq 0 \end{cases}$$

and  $\tilde{g}'(0) > g'(0)$ . Then, the radial distance from the origin of  $\gamma_n$  is bounded by that of  $\gamma_s$ .

**PROOF.** The proof of Lemma 2.3.1 only used that  $g'(0) < h'(0)$ , not requiring that  $g'(0)$  and  $h'(0)$  had different signs. Thus, using (2.10) as the shadow system, a similar proof to that of Lemma 2.3.1 gives the result.  $\square$

### 2.3.1. Canards at the smooth fold.

**THEOREM 2.3.3.** *Fix  $0 < \epsilon \ll 1$ . In system (2.10), assume (I) – (V) hold. Then there is a Hopf bifurcation when  $\lambda = x_M$ . If the Hopf bifurcation is non-degenerate, then it will produce canard cycles.*

**PROOF.** Direct calculation shows that (2.10) undergoes a Hopf bifurcation at  $\lambda = x_M$ . The criticality of the Hopf bifurcation is determined as usual [25], since it is a smooth Hopf bifurcation. Assume the criticality parameter is nonzero (i.e. the bifurcation is non-degenerate). Let  $\Gamma_\epsilon^n(\lambda)$  denote the family of stable periodic orbits in the nonsmooth system, and  $\Gamma_\epsilon^s(\lambda)$  denote the family for the smooth (shadow) system. For some  $\lambda_G(\epsilon)$ , the system undergoes a grazing bifurcation where the stable periodic orbit is tangent to the splitting line  $x = 0$  (which necessarily happens at  $(0, 0)$  since it happens on the  $x$  nullcline). If  $\Gamma^s(\lambda) \subset \{x > 0\}$  (which happens for all  $\lambda_G < \lambda < x_M$  in the supercritical case), then  $\Gamma^s = \Gamma^n$ .

Beyond the grazing bifurcation (i.e. for  $\lambda < \lambda_G$ ),  $\Gamma^s$  must cross the  $y$ -axis transversely. Let  $y_c > 0$  be the  $y$ -coordinate of the crossing into the left half-plane, and let  $y_d < 0$  be the  $y$ -coordinate where  $\Gamma^s$  re-enters the right half-plane. Define  $\gamma_n$  to be the trajectory of (2.10) through the point  $(0, y_d)$ . Without loss of generality, assume  $\gamma_n(0) = (0, y_d)$ . Then there exists a time  $t_c > 0$  so that  $\gamma_n(t_c) = (0, y_c)$  and for all  $t \in [0, t_c]$ ,  $\gamma_n$  coincides with  $\Gamma^s$ . By Lemma 2.3.1 for all  $t > t_c$ ,  $\gamma_n$  must be contained in the interior of  $\Gamma^s$ . In particular, there exists a pair  $(t_d, y_d^*)$  with  $t_d > t_c$  and  $y_d^* > y_d$ , such that  $\gamma_n(t_d) = (0, y_d^*)$ . Let  $V$  be the set enclosed by the closed curve

$$\partial V = \{\gamma_n(t) : 0 \leq t \leq t_d\} \cup \{(0, y) : y_d^* \leq y \leq y_c\}$$

The vector field of (2.10) is either tangent to or pointing inward on the  $\partial V$ , so Poincaré-Bendixson guarantees the existence of a stable periodic orbit on the interior of  $V$  (see Figure 2.6). This proves the result.  $\square$

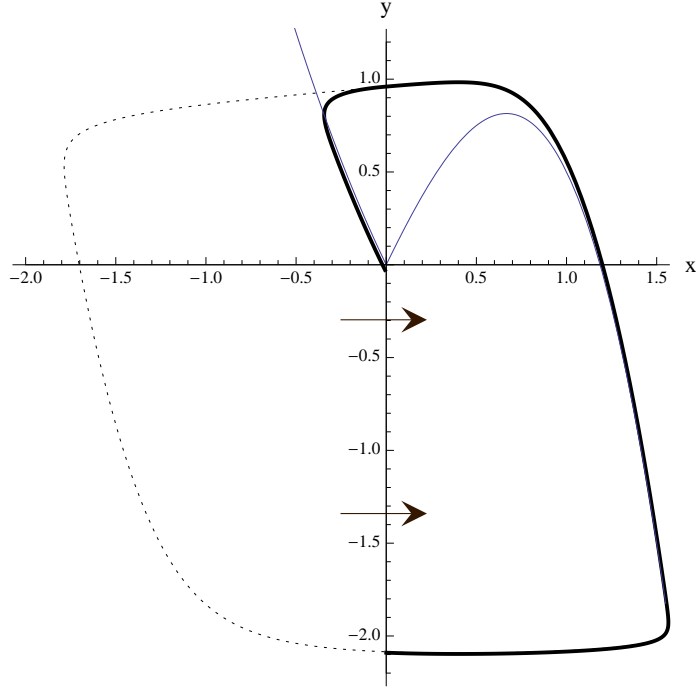


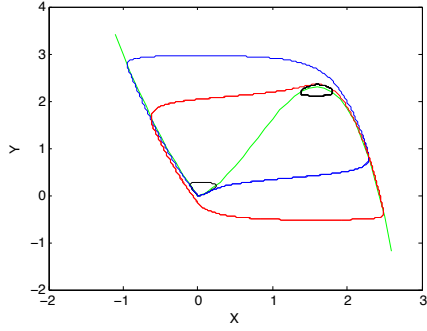
FIGURE 2.6. The set  $V$  for a given  $\lambda$ . The dashed curve is the periodic orbit of the shadow system. The bold curve is the trajectory in the nonsmooth system.  $V$  is the positively invariant set enclosed by the bold curve and the  $y$ -axis.

There is a simple corollary to Theorem 2.3.3.

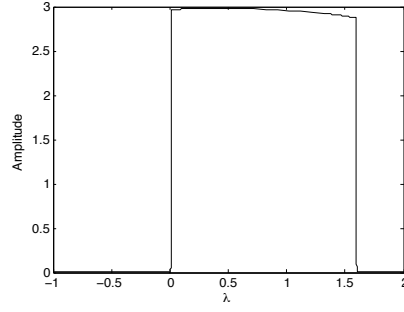
**COROLLARY 2.3.4.** *Assume the shadow system (2.11) satisfies assumptions (A1)-(A4). The parameter  $A$  (as defined in (2.7)) determines the criticality of the Hopf bifurcation according to Theorem 2.2.1. Furthermore, the  $\Gamma^n(\lambda)$  are bounded by the stable canard orbits.*

Given that canard explosion happens in smooth systems, the result should not be surprising. Perhaps more surprising is the possibility of having canard cycles arise as a result of a nonsmooth, Hopf-like bifurcation at  $\lambda = 0$ , explained in the following theorem. Figure 2.7 depicts the canard explosion at a smooth fold and a corner as a result of supercritical Hopf bifurcations in (2.10).

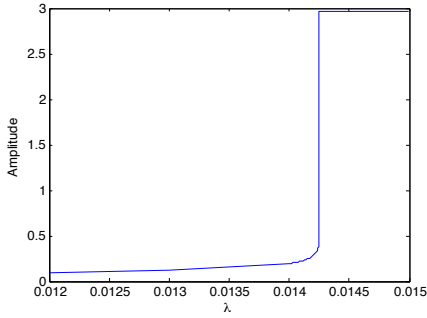
### 2.3.2. Conditions for the creation of canard cycles at the corner.



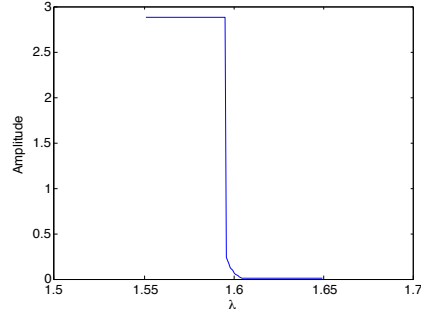
(A) Nonsmooth canard cycles in the supercritical case. The black orbits depict cycles before the explosion at both the smooth fold and the corner. The blue orbit is a post-explosion canard with head at the corner. The red orbit is a post-explosion canard with head at the smooth fold.



(B) Amplitudes of nonsmooth canard cycles in the supercritical case, showing the explosion at the corner (on the left) and smooth fold (on the right).



(C) A closer look at the explosion at the corner.



(D) A closer look at the explosion at the fold.

FIGURE 2.7. Images characterizing a nonsmooth canard explosion for  $\epsilon = 0.2$ . The bifurcations are supercritical at both the fold and the corner.

**THEOREM 2.3.5.** *In system (2.10), assume (I) – (V) hold. The system undergoes a bifurcation for  $\lambda = 0$  by which a stable periodic orbit  $\Gamma^n(\lambda)$  exists for  $0 < \lambda < x_M$ . There exists an  $\epsilon_0$  such that for all  $0 < \epsilon < \epsilon_0$  the nature of the bifurcation is described by the following:*

- (i) *If  $0 < h'(0) < 2\sqrt{\epsilon}$ , then canard cycles  $\Gamma^n(\lambda)$  are born of a Hopf-like bifurcation as  $\lambda$  increases through 0. The bifurcation is subcritical if  $|g'(0)| < |h'(0)|$  and supercritical if  $|g'(0)| > |h'(0)|$ .*



(ii) If  $h'(0) > 2\sqrt{\epsilon}$ , the bifurcation at  $\lambda = 0$  is a super-explosion. The system has a stable periodic orbit  $\Gamma^n(\lambda)$ , and  $\Gamma^n(\lambda)$  is a relaxation oscillation. If  $|g'(0)| \geq 2\sqrt{\epsilon}$ , the bifurcation is supercritical in that no periodic orbits appear for  $\lambda < 0$ . However, if  $|g'(0)| < 2\sqrt{\epsilon}$  the bifurcation is subcritical, in that a stable periodic and stable critical point coexist simultaneously for some  $\lambda < 0$ .

PROOF. The system always has a unique critical point  $p_\lambda = (\lambda, F(\lambda))$ , and direct computation of the corresponding eigenvalues shows that

$$(2.13) \quad \mu_\pm(\lambda) = \begin{cases} \frac{g'(\lambda) \pm \sqrt{[g'(\lambda)]^2 - 4\epsilon}}{2}, & \lambda < 0 \\ \frac{h'(\lambda) \pm \sqrt{[h'(\lambda)]^2 - 4\epsilon}}{2}, & \lambda > 0. \end{cases}$$

For  $0 < \lambda < x_M$  we have  $h'(\lambda) > 0$ , so both eigenvalues have  $\text{Re}(\mu_\pm) > 0$  and the critical point  $p_\lambda$  is unstable. To demonstrate the existence a stable periodic orbit  $\Gamma^n(\lambda)$ , it suffices to show that there is a positively invariant set containing  $p_\lambda$ . Consider the set  $W$  as shown in Figure 2.8. The boundary  $\partial W$  is composed of six line segments  $l_j$  for  $j = 1, 2, \dots, 6$ . Choose any point  $(\hat{x}, 0)$  with  $\hat{x} < 0$ .

$$l_1 = \{(x, y) : y = m_1(x - \hat{x}), m_1 < 0 \text{ is } \mathcal{O}(1), \hat{x} \leq x \leq \lambda\}$$

$$l_2 = \{(x, y_1) : y_1 = m_1(\lambda - \hat{x}), \lambda \leq x \leq x_2 = (h^{-1}(y_1) + 1)\}$$

$$l_3 = \{(x_2, y) : y_1 < y < y_3 = h(x_M)\}$$

$$l_4 = \left\{ (x, y) : y = m_4(x - x_2) + y_3 \text{ where } m_4 > \frac{g(\hat{x}) - y_3}{\lambda - x_2} \text{ is } \mathcal{O}(1) \right\}$$

$$l_5 = \{(x, y_5) : y_5 = m_4(\lambda - x_2) + y_3, \hat{x} < x < \lambda\}$$

$$l_6 = \{(\hat{x}, y) : 0 < y < y_5\}$$

Note that  $W$  can be made as large as needed. The vector field points inward on  $\partial W$  and Poincaré-Bendixson guarantees the existence of an attracting periodic orbit

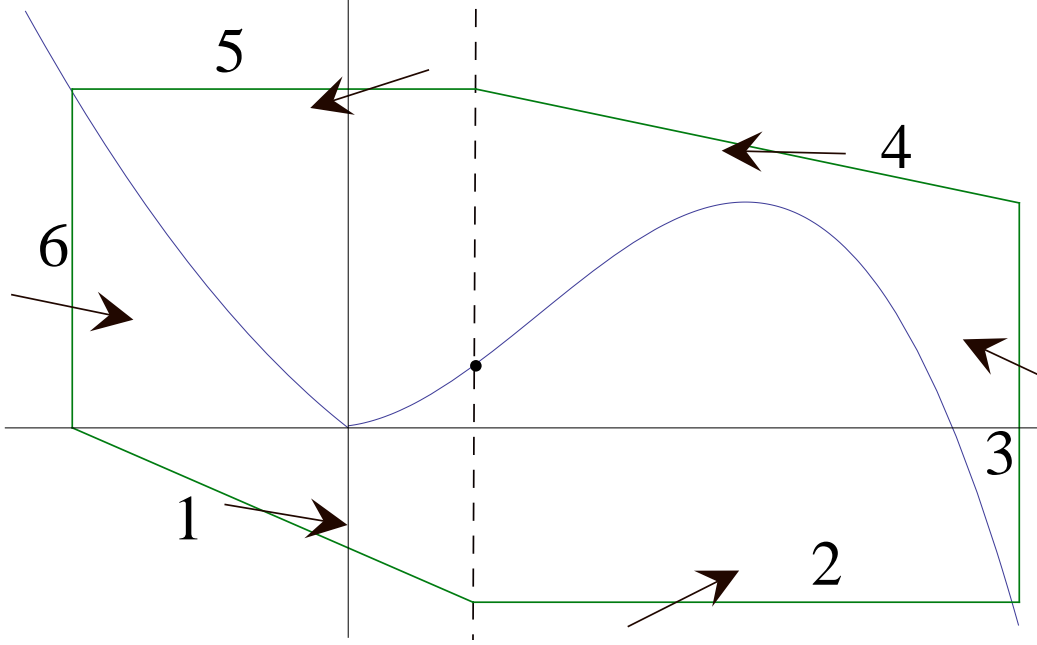


FIGURE 2.8. An example of a set  $W$  which is positively invariant. The numbers indicate the 6 line segments  $l_i$  forming the boundary  $\partial W$ .

$\Gamma^n(\lambda)$  for  $0 < \lambda < x_M$ . The  $\Gamma^n$  created through the bifurcation at  $\lambda = 0$  will differ in amplitude depending on  $h'(0)$ .

First, we consider the case where  $0 < h'(0) < 2\sqrt{\epsilon}$ . If  $|g'(0)| < 2\sqrt{\epsilon}$  as well, the bifurcation at  $\lambda = 0$  is the nonsmooth Hopf bifurcation discussed in Section 2.3, and Theorem 2.9 applies. In correspondence with Theorem 2.9, we have

$$\mu_u = h'(0)$$

$$\mu_s = |g'(0)|$$

$$\omega_u = \sqrt{(4\epsilon - [h'(0)]^2)}$$

$$\omega_s = \sqrt{(4\epsilon - [g'(0)]^2)},$$

and

$$\Lambda = \frac{\mu_u}{\omega_u} - \frac{\mu_s}{\omega_s}.$$

Thus

$$\begin{aligned}
\Lambda < 0 &\iff \frac{\mu_u}{\omega_u} < \frac{\mu_s}{\omega_s} \\
&\iff h'(0)\sqrt{[4\epsilon - g'(0)]^2} < |g'(0)|\sqrt{4\epsilon - [h'(0)]^2} \\
&\iff 4\epsilon[h'(0)]^2 - [h'(0)]^2 \cdot [g'(0)]^2 < 4\epsilon[g'(0)]^2[h'(0)]^2 \cdot [g'(0)]^2 \\
&\iff [h'(0)]^2 < [g'(0)]^2.
\end{aligned}$$

Therefore, there is a subcritical nonsmooth Hopf bifurcation when  $h'(0) < |g'(0)|$  and supercritical nonsmooth Hopf bifurcation when  $h'(0) > |g'(0)|$ . Corollary 2.3.2, also guarantees the existence of canard cycles for the case where  $|g'(0)| > 2\sqrt{\epsilon}$ . The bifurcation in that case is a stable node-to-unstable focus. The canard cycles in the system with a node will be contained in the cycles for the system with a nonsmooth Hopf (stable focus-to-unstable focus) bifurcation. This proves assertion (i).

Next, we consider the case where  $h'(0) \geq 2\sqrt{\epsilon}$ . In this case, for  $\lambda > 0$  (but bounded away from  $x_M$ ), the critical point  $p_\lambda$  is an unstable node. Let  $\mu_2 \geq \mu_1 > 0$  be the strong and weak unstable eigenvalues corresponding to  $p_\lambda$ . Also, let  $v_{1,2} = (x_{1,2}, y_{1,2})$  be the associated eigenvectors. Then for  $i = 1, 2$  we have

$$\begin{aligned}
h'(\lambda)x_i - y_i &= \mu_i x_i \\
\epsilon x_i &= \mu_i y_i.
\end{aligned}$$

This implies that the slope of the eigenvector

$$v_2 = \frac{\epsilon}{\mu_2}.$$

Now,  $\mu_2$  depends on  $\epsilon$ , however  $\mu_2 \rightarrow 2h'(\lambda)$  as  $\epsilon \rightarrow 0$ . Thus for  $\epsilon$  sufficiently small, we can make the slope of  $v_2$  as flat as we like. Therefore, there exists an  $\epsilon_0$  such that for all  $0 < \epsilon < \epsilon_0$ , the strong unstable trajectory must enter the region of phase space  $x > x_M$ , pass over the point  $(x_M, h(x_M))$  and proceed to the left-half plane. Since the vector field of (2.10) points into the left half-plane along the  $y$ -axis for  $y > 0$ , the strong unstable trajectory must re-enter the right half-plane somewhere below

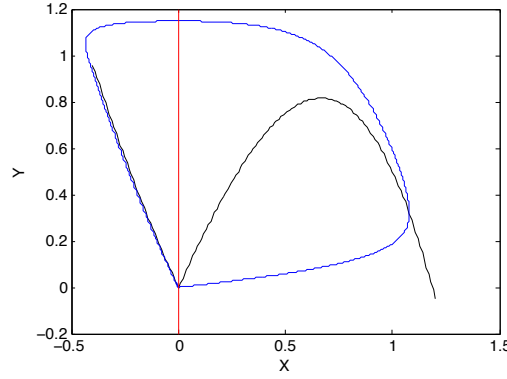


FIGURE 2.9. The stable orbit of a super-explosion (blue) for  $\epsilon = 0.2$ . The line  $x = \lambda$  (red) is the slow nullcline. Here  $\lambda = 0.001$ .

$y = 0$ . Following the trajectory further, it must continue downward to the right until it reaches the  $y$ -nullcline  $x = \lambda$  at some point  $(\lambda, \hat{y})$  where  $\hat{y} < h(\lambda)$ . Let  $V$  be the region enclosed by the trajectory described above and the line segment along  $x = \lambda$  connecting  $\hat{y}$  and  $h(\lambda)$ . All trajectories in  $W$  that start outside of  $V$  are bounded outside of  $V$  (see Figure 2.10a). Therefore  $\Gamma^n(\lambda)$  must be a relaxation oscillation, and the bifurcation must be a super-explosion, as depicted in Figure 2.9.

Suppose also that  $g'(0) \geq 2\sqrt{\epsilon}$ . Then, for  $\lambda < 0$  the equilibrium  $p_\lambda$  is a stable node. It is the global attractor of the system (as in Theorem 2.2.6) since, the strong stable trajectory to  $p_\lambda$  bounds trajectories above the node in the left half-plane. Since no stable periodic orbits can coexist with  $p_\lambda$ , we say the bifurcation is supercritical.

On the other hand, if  $g'(0) < 2\sqrt{\epsilon}$ ,  $p_\lambda$  is a stable focus. For  $\lambda < 0$ ,  $|\lambda|$  sufficiently small, there exists a  $\beta \in (g(\lambda), h(x_M))$  such that the trajectory through  $(0, \beta)$  spirals around  $p_\lambda$  and enters the right half plane below  $(0, 0)$ . The dynamics in the right half-plane are governed by an unstable node in the shadow system (2.11). After entering the right half-plane, the trajectory through  $\beta$  must proceed to cross  $N^r$  and reenter the left half-plane at  $(0, \beta')$  where  $\beta' > \beta$ . If we let  $V'$  denote the region enclosed by the trajectory through  $(0, \beta)$  and the line segment along the  $y$ -axis connecting  $\beta$  to  $\beta'$ , then  $V'$  is a negatively invariant set. We can choose  $W$  large enough so that  $V' \subset W$ . The set  $W \setminus V'$  is positively invariant and contains no stable critical points

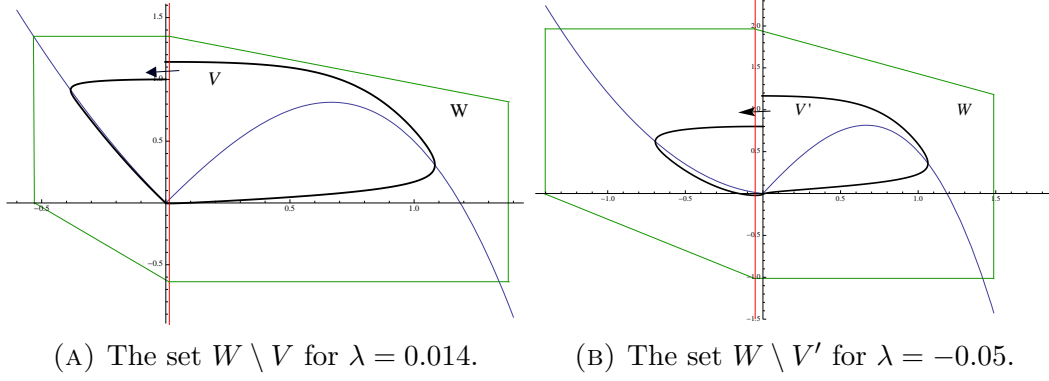


FIGURE 2.10. Positively invariant sets. These sets demonstrate the existence of attracting periodic orbits for (a) the standard (supercritical) super-explosion and (b) the subcritical super-explosion.  $W$  is the region bounded by the six (green) line segments as in Figure 2.8. The sets enclosed by the bold trajectory are (a)  $V$  or (b)  $V'$ .

(see Figure 2.10b). Therefore, there must be an attracting periodic orbit  $\Gamma^n(\lambda)$  inside  $W \setminus V'$ . Since an attracting critical point and an attracting periodic orbit coexist simultaneously, we call this a subcritical super-explosion. This proves assertion (ii).

□

There are two simple corollaries to Theorem 2.3.5.

COROLLARY 2.3.6. *Consider the system with two corners and no smooth folds*

$$(2.14) \quad \begin{aligned} \dot{x} &= -y + F(x) \\ \dot{y} &= \epsilon(x - \lambda) \end{aligned}$$

where

$$F(x) = \begin{cases} g(x) & x \leq 0 \\ h(x) & 0 \leq x \leq x_M \\ f(x) & x_M \leq x \end{cases}$$

with  $g, h, f \in C^k$ ,  $k \geq 1$ ,  $g(0) = h(0) = 0$ ,  $f(x_M) = h(x_M)$ ,  $g'(0) < 0$ ,  $h'(x) > 0$  for all  $0 < x < x_M$ , and  $f'(x_M) < 0$ . The system undergoes a bifurcation for  $\lambda = 0$  by which a stable periodic orbit  $\Gamma^n(\lambda)$  exists for  $0 < \lambda < x_M$ . There exists an  $\epsilon_0$  such that for all  $0 < \epsilon < \epsilon_0$  the nature of the bifurcation is described by the following:

- (i) If  $0 < h'(0) < 2\sqrt{\epsilon}$ , then canard cycles  $\Gamma^n(\lambda)$  are born of a Hopf-like bifurcation as  $\lambda$  increases through 0. The bifurcation is subcritical if  $|g'(0)| < |h'(0)|$  and supercritical if  $|g'(0)| > |h'(0)|$ .
- (ii) If  $h'(0) > 2\sqrt{\epsilon}$ , the bifurcation at  $\lambda = 0$  is a super-explosion. The system has a stable periodic orbit  $\Gamma^n(\lambda)$ , and  $\Gamma^n(\lambda)$  is a relaxation oscillation. If  $|g'(0)| \geq 2\sqrt{\epsilon}$ , the bifurcation is supercritical in that no periodic orbits appear for  $\lambda < 0$ . However, if  $|g'(0)| < 2\sqrt{\epsilon}$  the bifurcation is subcritical, in that a stable periodic and stable critical point coexist simultaneously for some  $\lambda < 0$ .

PROOF. The proof is the same as that of Theorem 2.3.5, only we use (2.10) as our shadow system.  $\square$

The second corollary is an immediate application of Lemma 2.3.1.

COROLLARY 2.3.7. Fix  $\epsilon > 0$ . Assume the shadow system (2.11) satisfies the assumptions (A1)-(A4) for a canard point at  $(x_m, h(x_m))$  where  $x_m < 0$ . Then for fixed  $\lambda \in (0, x_M)$ ,  $\Gamma^n(\lambda)$  is bounded by the periodic orbit  $\Gamma^s$  of the shadow system. Furthermore, if  $A < 0$  and  $|x_m| < \lambda_s(\sqrt{\epsilon})$ , then (2.10) will undergo a canard explosion.

We have demonstrated that there are two types of nonsmooth bifurcations in which periodic orbits appear before the parameter reaches the bifurcation value. We will show that these are truly subcritical bifurcations. In other words, as the bifurcation parameter moves away from the bifurcation value, the periodic orbits are destroyed.

PROPOSITION 2.3.8. In a system of the form (2.10) for which there exists an  $m < 0$  such that  $g'(x) \leq m < 0$  for all  $x < 0$ . Then there exists a  $K > 0$  such that if  $\lambda < -K$ , the system has no periodic orbits.

PROOF. The idea of the proof is amounts to using a variation of Dulac's criterion [25] for the non-existence of periodic orbits. Define

$$G(x, y) = (F(x) - y, \epsilon(x - \lambda)),$$

so  $G(x, y)$  is the vector field. We will need to use the divergence  $\nabla \cdot G$  often, and direct computation shows

$$\nabla \cdot G = F'(x).$$

First, if  $\lambda < 0$ , the only critical point lies in the left half-plane. Since any periodic orbit of a planar system must encircle a critical point, there can be no periodic orbits entirely contained the set  $x \geq 0$ .

Secondly, there can be no periodic orbits entirely contained in the left half-plane. We will show this by contradiction. Suppose there is a periodic orbit  $\Gamma$  contained entirely in the left half-plane, and define  $D$  to be the region enclosed by  $\Gamma$ . Then

$$\nabla \cdot G \geq m \quad \text{for all } x < 0.$$

Therefore,

$$\int \int_D \nabla \cdot G dx dy < 0.$$

But by the divergence theorem

$$\int_{\Gamma} (n \cdot F) ds = \int \int_D \nabla \cdot F dx dy.$$

However,  $\Gamma$  is a trajectory, so

$$\int_{\Gamma} (n \cdot G) ds = 0,$$

and we have a contradiction.

We will show that there are no periodic orbits that cross  $x = 0$  in a similar way. Suppose there is a periodic orbit that crosses  $x = 0$ . Then it must do so twice; let  $p_1 = (0, y_1)$ ,  $p_2 = (0, y_2)$  with  $y_1(\lambda) > 0 > y_2(\lambda)$  be the points where  $\Gamma$  intersects the  $y$ -axis. Also, define  $B(\lambda) = y_1(\lambda) - y_2(\lambda)$ . Note that  $B(\lambda)$  is the maximum vertical amplitude of the periodic orbit in the region  $x \geq 0$ . Let  $k$  be the maximum slope of  $h(x)$  on the interval  $0 \leq x \leq x_M$ . Since  $F'(x) \geq 0$  only the set  $x \in [0, x_M]$ , we know

$$\int \int_{D \cap \{x \geq 0\}} \nabla \cdot G dx dy \leq \int \int_{R(\lambda)} \nabla \cdot G dx dy \leq k x_M B(\lambda),$$

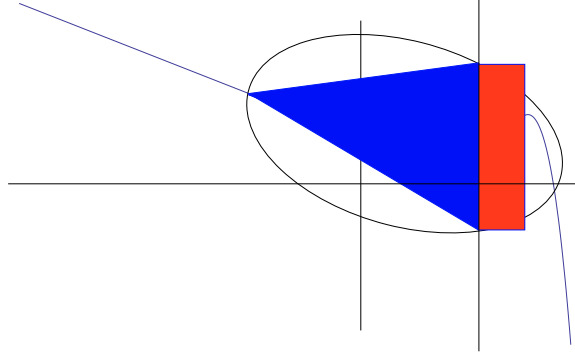


FIGURE 2.11. Important sets for the proof of Proposition 2.3.8.  $\nabla \cdot G < 0$  is negative on the interior of the triangle  $D^*(\lambda)$  (blue).  $\nabla \cdot G|_D > 0$  on a region bounded by the rectangle  $R(\lambda)$  (red).

where  $R(\lambda)$  is the rectangle with  $B(\lambda)$  forming the left side and having width  $x_M$ . Next, let  $p_0 = (x_0, y_0)$  be the point where  $\Gamma$  intersects the fast nullcline  $y = g(x)$ , for  $x_0 < \lambda$ . Define  $B_1(\lambda)$  to be the line segment connecting  $p_0$  to  $p_1$  and  $B_2(\lambda)$  to be the line segment connecting  $p_0$  to  $p_2$ . Then  $B_1$  and  $B_2$  have constant slope (for fixed  $\lambda$ ). Let  $D^*(\lambda)$  be the interior of the triangle enclosed by  $B(\lambda)$ ,  $B_1(\lambda)$ , and  $B_2(\lambda)$ . Then  $D^*$  must lie entirely inside  $D$ . Along  $B_1$  near  $p_1$ , the vector field must point out of  $D^*$ . Since the slopes of the vectors are monotonically decreasing along  $B_1$ , if  $\Gamma$  were ever to cross  $B_1$  somewhere other than the endpoints,  $\Gamma$  would be trapped inside  $D^*$ . This would contradict that  $p_0$  lies on  $\Gamma$ . A similar argument in reverse time shows that  $\Gamma$  cannot cross  $B_2$ . Figure 2.11 areas of the sets  $D^*(\lambda)$  and  $R(\lambda)$ .

If we let  $A(\lambda)$  be the area of the region  $D^*(\lambda)$ , then

$$A(\lambda) > \frac{|\lambda|}{2} B(\lambda).$$

Since  $g'(x) \leq m < 0$ , we have

$$\int \int_{D \cap \{x < 0\}} \nabla \cdot G dx dy < \int \int_{D^*} \nabla \cdot G dx dy < m \frac{\lambda}{2} B(\lambda).$$

Thus, if  $\lambda < 2x_M \frac{k}{m}$ , we can conclude

$$\int \int_D G dx dy < 0.$$



Therefore, by the divergence theorem,  $\Gamma$  cannot be a periodic orbit.  $\square$

## 2.4. Discussion

In this chapter, we have demonstrated the existence of canard cycles in planar non-smooth fast/slow systems with a piecewise-smooth ‘S’-shaped critical manifold, pushing the theory beyond piecewise linear systems. Through comparison with smooth shadow systems, we have shown that the amplitudes of canard cycles in nonsmooth systems are bounded by the amplitudes of canard cycles in corresponding smooth systems. As we see in Figure 2.7, it is possible for a corner to produce canards with head, and there is a delay between the bifurcation and the explosion phase. This is a contrast to the piecewise linear case, where the quasi-canards are unable to produce the variety with heads, and the explosion phase begins immediately upon bifurcation. In this respect, canards in piecewise smooth systems are more like their cousins in smooth systems. On the other hand, the splitting line is essential for super-explosion. The instantaneous transition from a globally attracting equilibrium point to relaxation oscillations is a product of the nonsmooth nature of the system. One can think of this work as bridging the gap between what is known about canards in smooth systems on one side and piecewise linear systems on the other side.

This work does not put to bed entirely the theory of canards in piecewise-smooth planar systems. We considered specifically the case where the splitting line and slow nullcline were both vertical lines (i.e. orthogonal to the fast direction). It is probably not too difficult to generalize the work of this paper to the more general case where the splitting line and slow nullcline are parallel. Potentially more difficult would be generalizing the work here to a situation where the slow nullcline intersects the splitting line or even is piecewise-smooth itself.

While in planar systems, canard phenomena are difficult to detect due to the exponentially narrow window of the explosion phase, in three dimensional smooth systems canards are more robust. Furthermore, canard solutions in the singular limit can lead to much more complicated periodic solutions called *mixed-mode oscillations*.

For a survey on mixed-mode oscillations and the role of canards, see [14]. These mixed-mode oscillations have important applications in biology, specifically in neural models. As we will see in Chapter 3.5, these complicated oscillations have a role in climate science as well.

## CHAPTER 3

# Relaxation Oscillations in an Idealized Ocean Circulation Model

### 3.1. Introduction

An important aspect of the climate system is the variability in the climate record. An understanding of this variability, specifically with regard to glacial millennial climate change, has remained elusive (see [11]). In different eras of Earth's history, the variations themselves change in both period and amplitude. It is even possible to have small oscillations superimposed over larger oscillations. Increasingly, scientists are utilizing improved technology to study the climate system through high-powered computer simulations. Large scale oscillations and critical transitions, however, are often better understood by examining conceptual models that can be studied analytically. Crucifix reviews key dynamical systems concepts and their applications to paleoclimate problems in [12], mentioning relaxation oscillations in particular.

Over the last 100 kyr the climate record shows a series of Dansgaard-Oeschger (D-O) events. In [11], Cronin describes the temperature change corresponding with D-O events as “characterized by an initial sharp increase over only a few decades or less followed by a gradual decline...and finally a sharp drop.” Figure 3.1 depicts Dansgaard-Oeschger events during the last glacial period. The description provided by [11] along with the plateaus at bottoms of the cycles seen in Figure 3.1 are reminiscent of relaxation oscillations.

Since the effects of these critical climate transitions are most dramatic in the North Atlantic, scientists have hypothesized that D-O events are accompanied by changes in ocean circulation in the North Atlantic. The bistability of the circulation in the North

Atlantic was first demonstrated by Stommel in 1961 [61]. Physical oceanographers have provided a vast array of models capturing various mechanisms that can cause the circulation to oscillate between the two steady states in Stommel’s model. Dijkstra and Ghil surveyed many of these models in [17]. Some models generate oscillations as a result of intrinsic ocean dynamics [10]. Other models generate oscillations due to changes in freshwater forcing, be it periodic [24] or stochastic [7]. In [55], Saltzman, Sutera, and Evenson argue that thermal effects are the driving force behind the oscillations. Additionally, Saha shows that an ocean-ice feedback mechanism can generate oscillations [50, 51].

The aims of this chapter of the thesis are to prove the existence of attracting periodic orbits in two adaptations of Stommel’s model. In the first adaptation, we incorporate the ‘freshwater forcing’ parameter—actually a ratio of precipitation forcing to thermal forcing—as a dynamic slow variable. The adapted model is a three time-scale model with three variables (1 fast, 1 intermediate, and 1 slow). We use GSP to reduce the model to a 2D fast/slow system and show that, for a certain parameter range, the reduced system has an ‘S’-shaped fast nullcline. We then find conditions under which the model has either a relaxation oscillation or a canard cycle.

In the second adaptation of the model, we incorporate the precipitation and thermal forcing terms as separate dynamic variables. The model is a three time-scale model with four variables (1 fast, 1 intermediate, and 2 slow). Again, we use GSP to reduce the model by one dimension. The reduced model is a fast/slow system with two slow variables, and the fast nullcline has a bistable, ‘S’-shaped region. The nullcline also has a cusp point where the boundaries of both stable regions meet. The ‘S’-shape of the nullcline allows for a periodic orbit with two relaxation phases, and we find conditions under which the model has an attracting orbit of this type. The cusp theoretically allows for the possibility of a periodic orbit with only one relaxation phase, however we show that this is impossible for physically relevant parameters.

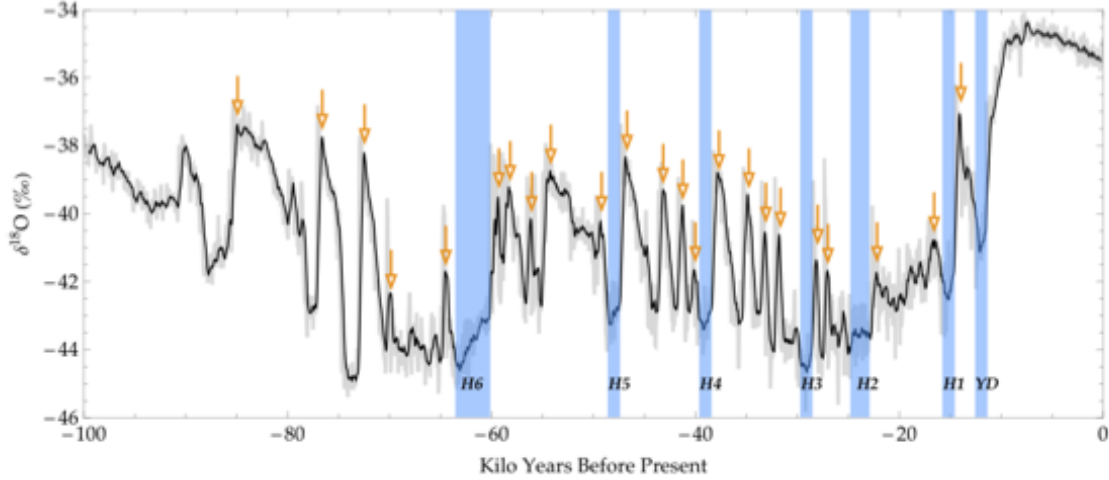


FIGURE 3.1. Oxygen isotope data from Greenland (NGRIP). Orange arrows indicate thermal maxima of Dansgaard-Oeschger cycles over the last 100,000 years. Figure courtesy of Saha [50].

The relevant background material from GSP theory is discussed in section 2. Section 3 describes the physical mechanisms in Stommel’s 1961 model. We also analyze the model using geometric singular perturbation theory, following the analysis of Glendinning [26]. In Section 4, we develop and analyze the first adapted model. Section 5 focuses on the second adapted model. Finally, the chapter concludes with further discussion in Section 6.

### 3.2. Stommel’s Model

Investigating changes in ocean circulation begins with Stommel’s 2-box model. Stommel modeled the North Atlantic by partitioning it into an equatorial and a polar region. He assumed that water near the equator would become warmer and saltier due to its interaction with the atmosphere. Water near the pole would lose its heat to the atmosphere and have its salt concentration diluted by incoming freshwater. Oceanic circulation causes the water in the two regions to mix, preventing either box from equilibrating with its surrounding environment. The density difference between the boxes drives the circulation, and it is the salinity and temperature of each box that determines the density. The analysis in this section follows [26] and [32]. It

is included here as a reminder of the mechanics of Stommel's model and a means of setting up the equations for the main results of this paper.

The equations describing the model are

$$\begin{aligned}
(3.1) \quad \frac{d}{dt}T_e &= R_T(T_e^a - T_e) + |\psi|(T_p - T_e) \\
\frac{d}{dt}T_p &= R_T(T_p^a - T_p) + |\psi|(T_e - T_p) \\
\frac{d}{dt}S_e &= R_S(S_e^a - S_e) + |\psi|(S_p - S_e) \\
\frac{d}{dt}S_p &= R_S(S_p^a - S_p) + |\psi|(S_e - S_p).
\end{aligned}$$

Here,  $T$ 's are temperatures and  $S$ 's are salinities. The subscripts  $e$  and  $p$  denote the box at the equator and pole, respectively, while the superscript  $a$  denotes an atmospheric forcing term. The strength of the circulation is given by  $|\psi|$ , where

$$\psi = \psi_0 \left( \frac{\rho_p - \rho_e}{\rho_0} \right).$$

The density of box  $i$  is denoted  $\rho_i$ , and it is calculated using a linear equation of state with reference values  $T_0$ ,  $S_0$  and  $\rho_0$ . So,

$$\rho_i = \rho_0[1 - \alpha(T_i - T_0) + \beta(S_i - S_0)].$$

Thus  $\psi$  is easily computed to be

$$(3.2) \quad \psi = \psi_0[\alpha(T_e - T_p) - \beta(S_e - S_p)].$$

Next, the system is reduced to have only two degrees of freedom by looking at the temperature and salinity differences between the boxes. This comes from assuming that  $T_e + T_p = T_e^a + T_p^a$  and similarly for the salinity terms. The assumption is justified by conservation of heat and conservation of salt, which are similar to conservation of energy and mass, respectively. Defining

$$\begin{aligned}
T &= T_e - T_p, & S &= S_e - S_p, \\
T^a &= T_e^a - T_p^a, & S^a &= S_e^a - S_p^a,
\end{aligned}$$

reduces (3.1) to

$$(3.3) \quad \begin{aligned} \frac{d}{dt}T &= R_T(T^a - T) - 2|\psi|T \\ \frac{d}{dt}S &= R_S(S^a - S) - 2|\psi|S, \end{aligned}$$

and (3.2) becomes

$$\psi = \psi_0(\alpha T - \beta S).$$

To non-dimensionalize the system, set

$$x = \frac{T}{T^a}, \quad y = \frac{\beta S}{\alpha T^a}, \quad \tau = R_S t, \quad \mu = \frac{\beta S^a}{\alpha T^a}, \quad A = \frac{2\psi_0 \alpha T^a}{R_S}.$$

Then the system (3.3) becomes

$$(3.4) \quad \begin{aligned} \epsilon \dot{x} &= 1 - x - \epsilon A|x - y|x \\ \dot{y} &= \mu - y - A|x - y|y, \end{aligned}$$

where

$$\epsilon = \frac{R_S}{R_T} \ll 1$$

is a small parameter and the dot (  $\dot{\phantom{x}}$  ) denotes differentiation with respect to  $\tau$ . The system (3.4) is a fast/slow system set up to be analyzed using GSP. In the limit as  $\epsilon \rightarrow 0$ ,  $\{x = 1\}$  is a globally attracting, and therefore normally hyperbolic, critical manifold. The reduced problem has one degree of freedom, so the dynamics are entirely characterized by equilibria. The system is

$$(3.5) \quad \dot{y} = \mu - y - A|1 - y|y.$$

Critical points occur at

$$(3.6) \quad \mu = \begin{cases} (1 + A)y - Ay^2 & \text{for } y < 1 \\ (1 - A)y + Ay^2 & \text{for } y > 1 \end{cases}$$

and the nature of the system depends on  $A$ , as seen in Figure 3.2. Taking a derivative

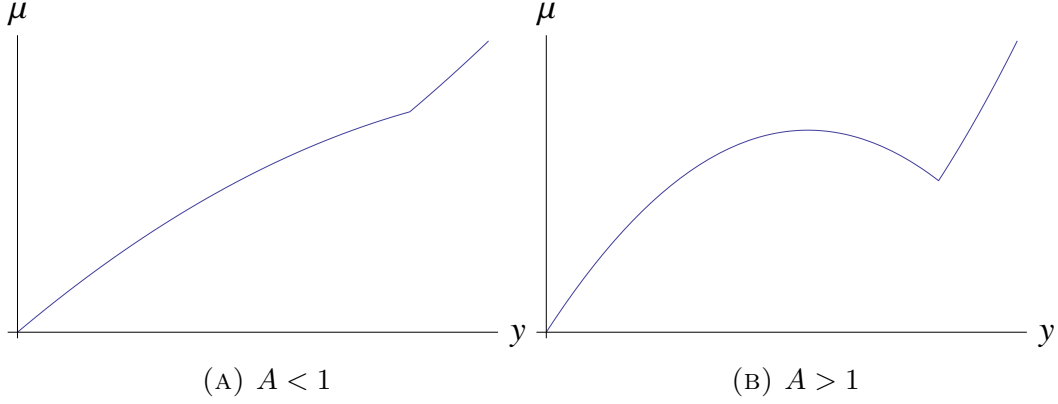


FIGURE 3.2. Graphs of (3.6) for (a)  $A < 1$  and (b)  $A > 1$ .

gives

$$\frac{d\mu}{dy} = \begin{cases} (1 + A) - 2Ay & \text{for } y < 1 \\ (1 - A) + 2Ay & \text{for } y > 1. \end{cases}$$

If  $A < 1$ , then the curve of equilibria  $\mu = \mu(y)$  is monotone increasing. The system (3.5), and consequently (3.4), has a unique equilibrium solution. The equilibrium is globally attracting, and it is important to remember that the solution corresponds to a unique stable circulation state (i.e., direction and strength).

However, if  $A > 1$  the system exhibits bistability for a range of  $\mu$  values. While  $\mu(y)$  is still monotone increasing for  $y > 1$ , the curve has a local maximum at  $y = (1 + A)/(2A) < 1$ . Thus for  $1 < \mu < (1 + A)^2/(4A)$  there are three equilibria. The system is bistable with the outer two equilibria being stable, and the middle equilibrium being unstable. The stable equilibrium for  $\psi < 0$  is called the haline state, since the circulation is driven by the salinity difference. When  $\psi > 0$ , the circulation is driven by temperature, and the system is in the thermal state. In the bistable regime, there is a stable thermal state as well as an unstable thermal state. As mentioned in the introduction, some oceanographers attempt to explain oscillations using only oceanic processes, however Figure 3.3 suggests  $\mu$  is the key to generating such oscillations.



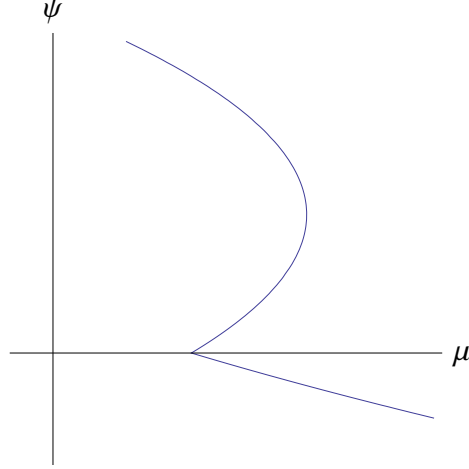


FIGURE 3.3. Bifurcation diagram for (3.4).  $\psi = x - y$ .

### 3.3. Dynamic Oscillations with 1 Slow Variable

If  $\mu$  is the key to oscillations, there may be an intrinsic feedback mechanism that causes  $\mu$  to change. Recall that  $\mu$  is the ratio of the effect of atmospheric salinity forcing on density to that of atmospheric temperature forcing on density. The idea is to consider how the state of the ocean affects its interaction with the atmosphere. Typically, in a coupled ocean-atmosphere model, the atmosphere is the fast component and the ocean is the slow component (see [66], for example). However, in Stommel's model,  $\mu$  is considered constant. Therefore, if a model is going to incorporate  $\mu$  as a dynamic variable, it should vary on a slower time scale than the other variables in the model. The physical intuition is to consider the variation of long term average behavior in the atmosphere. A general system of this form is

$$\begin{aligned}
 x' &= 1 - x - \epsilon A|x - y|x \\
 y' &= \epsilon(\mu - y - A|x - y|y) \\
 \mu' &= \epsilon \delta f(x, y, \mu, \delta, \epsilon),
 \end{aligned}
 \tag{3.7}$$

where  $\delta \ll 1$  is another small parameter. This system is a three time-scale model where  $x$  is fast,  $y$  is intermediate, and  $\mu$  is slow. If  $f(x, y, \mu, 0, 0)$  behaves in a desirable manner, one can turn the hysteresis loop in the bifurcation diagram into a true periodic orbit. The important question to answer is “how do variations in  $x$  and  $y$

affect  $\mu$ ?" One way the ocean can affect the atmosphere is through clouds, and here we list (reasonable) assumptions about long-term ocean-atmosphere feedback. An increase in ocean temperature should lead to increased evaporation, and thus increased cloud formation. An increase in salinity should cause a decrease in evaporation and decreased cloud formation. Clouds are important because they reflect sunlight back to space before it reaches the Earth's surface. Therefore an increase in clouds will decrease the effect of heat forcing near the equator where the sun's effect is strongest. Near the poles, clouds serve as a blanket, preventing heat from escaping. Thus, more clouds mean a decrease in  $T^a$  (from (3.3)). Having more clouds is a result of more evaporation at the equator and leads to more precipitation at high latitudes. So more clouds also mean an increase in  $S^a$  (also from (3.3)). Mathematically, the effects are

$$\frac{\partial T^a}{\partial T} < 0 \quad \frac{\partial T^a}{\partial S} > 0$$

$$\frac{\partial S^a}{\partial T} > 0 \quad \frac{\partial S^a}{\partial S} < 0$$

since  $T$  larger means a greater temperature difference between boxes (for the same average temperature) and thus a warmer equator. Similarly, larger  $S$  means a saltier equator. Recalling that

$$\mu = \frac{\beta S^a}{\alpha T^a},$$

the dependence of  $f$  on  $x$  and  $y$  must be

$$(3.8) \quad \frac{\partial f}{\partial x} > 0 \quad \text{and} \quad \frac{\partial f}{\partial y} < 0.$$

If this condition is implemented in the simplest possible way, then there is a parameter regime in which the system has a unique periodic orbit. Taking  $f$  to be a linear function of  $x$  and  $y$ , (3.7) becomes

$$(3.9) \quad \begin{aligned} x' &= 1 - x - \epsilon A|x - y|x \\ y' &= \epsilon(\mu - y - A|x - y|y) \\ \mu' &= \epsilon\delta(1 + ax - by). \end{aligned}$$

As in the previous section,  $\{x = 1\}$  is still an attracting critical manifold. However, the reduced problem,

$$(3.10) \quad \begin{aligned} \dot{y} &= \mu - y - A|1 - y|y \\ \dot{\mu} &= \delta(1 + a - by), \end{aligned}$$

is now itself a fast/slow system which is analyzed using GSP. The shape of the critical manifold of (3.10) depends on the parameter  $A$ , similar to the previous section. In fact, the critical manifolds will be precisely the curves in Figure 3.2. Above the curve, the fast dynamics (fixed  $\mu$  trajectories) will move to the right. Below the curve, the fast dynamics moves to the left. As expected, the sections of the curves which corresponded to stable equilibria in (3.4) (and consequently (3.5)) are now attracting branches of a critical manifold in (3.10). The decreasing portion of the graph in Figure 3.2b, which contains the unstable equilibrium for the bistable regime in (3.4) is now a repelling branch of a critical manifold. Let

$$(3.11) \quad M_0 = \{\mu = y + A|1 - y|y\}$$

denote the critical manifold.

The dynamics on  $M_0$  depend only on parameters and  $y$ , which is fast in the reduced problem. Therefore, the key to resolving the slow flow is the location of the  $\mu$  nullcline. The cases  $A < 1$  and  $A > 1$  are treated separately, due to the different shape of the critical manifold as depicted in Figure 3.2.

**3.3.1. Globally Attracting Critical Manifold.** Here we consider the case where  $A < 1$ . Since the only two branches of  $M_0$  are both attracting for  $A < 1$ , one expects that it should behave as a 1-dimensional system. The intersection of the  $\mu$  nullcline and the critical manifold should be a globally attracting critical point, however GSP cannot be applied “out of the box” due to the non-differentiability of the vector field. Instead, we consider two distinct smooth dynamical systems: (1) where  $|1 - y| = 1 - y$  and (2) where  $|1 - y| = y - 1$ . The system where  $|1 - y| = 1 - y$  agrees with (3.10)

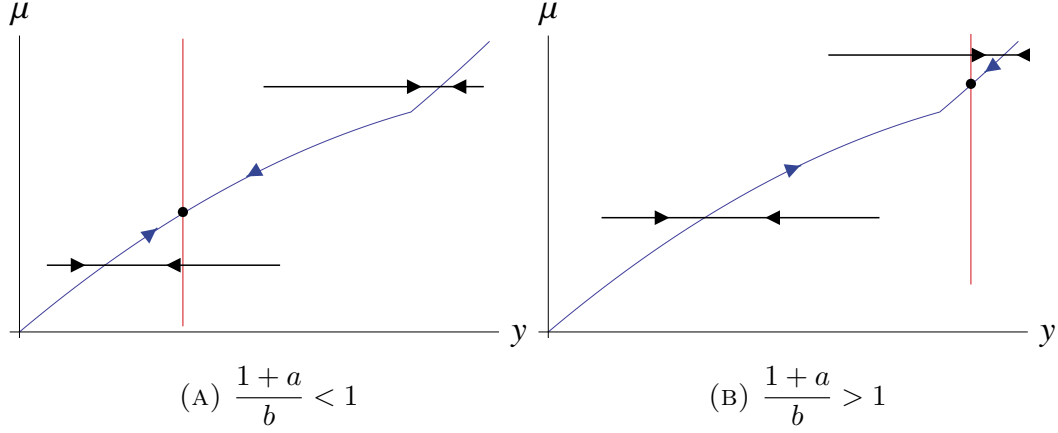


FIGURE 3.4. Possible phase spaces of (3.10) for  $A < 1$  and  $1 + a \neq b$ . The red line is the  $\mu$  nullcline. The black arrows indicate fast dynamics, and the blue arrows indicate slow dynamics.

when  $y < 1$ . Similarly the system where  $|1 - y| = y - 1$  agrees with (3.10) when  $y > 1$ .

The dynamics of (3.10) is obtained by taking trajectories from the two smooth systems and cutting them along the line  $y = 1$ —called the splitting line—where both smooth systems agree with the system of interest. We then paste the relevant pieces together along the splitting line. Since the right-hand side in (3.10) is Lipschitz, trajectories pass through the splitting line in a well-defined manner due to uniqueness of solutions.

Now, GSP can be applied to both of the smooth systems, which will produce two critical manifolds that intersect (in the singular limit) when  $y = 1$ .  $M_0$  defined in (3.11) is obtained by taking the relevant critical manifold on either side of the splitting line. The  $\mu$  nullcline is the vertical line

$$y = \frac{1+a}{b}.$$

We see that  $\mu$  is increasing to the left of this line, and decreasing to the right of this line as in Figure 3.4. Therefore the system has a globally attracting equilibrium if  $A < 1$ .

**3.3.2. Bistable Critical Manifold.** If  $A > 1$ , the system is much more interesting due to the ‘S’-shaped critical manifold. To simplify the analysis, we rewrite (3.10) as

$$(3.12) \quad \begin{aligned} \dot{y} &= \mu - y - A|1 - y|y \\ \dot{\mu} &= \delta_0(\lambda - y), \end{aligned}$$

where  $\delta_0 = \delta b$  and  $\lambda = (1 + a)/b$ .

**THEOREM 3.3.1.** *Consider the system (3.12) with  $A > 1$ ,  $0 < \delta_0 \ll 1$ , and  $\lambda > 0$  fixed. Then the following statements hold:*

- (A) *For  $\lambda \geq 1$ , there is a globally attracting equilibrium in the haline state.*
- (B) *For  $(1 + A)/(2A) < \lambda < 1$  the equilibrium is unstable and surrounded by a unique stable periodic orbit created through a non-smooth bifurcation at  $\lambda = 1$ .*
  - (i) *When  $A < 1 + 2\sqrt{\delta_0}$ , the bifurcation creates non-smooth canard cycles.*
  - (ii) *When  $A > 1 + 2\sqrt{\delta_0}$ , the bifurcation is a super-explosion and the periodic orbit is a relaxation oscillation for*

$$\frac{1 + A + 2\sqrt{\delta_0}}{2A} < \lambda < 1.$$

- (C) *For  $\lambda \leq (1 + A)/(2A)$  there is an attracting equilibrium in the thermal state.*

**PROOF.** Define  $F_{\pm}(y) = y \pm A(1 - y)y$ , and

$$F(y) = \begin{cases} F_+(y) & y < 1 \\ F_-(y) & y > 1 \end{cases}$$

Then (3.12) always has a unique equilibrium at  $(y_0, \mu_0) = (\lambda, F(\lambda))$ . Direct computation shows that the Jacobian of (3.12) is

$$(3.13) \quad J(\lambda, F(\lambda)) = \begin{pmatrix} -F'(\lambda) & 1 \\ \delta_0 & 0 \end{pmatrix},$$

We see that  $\det J > 0$  everywhere, and  $\text{Tr}(J) < 0$  when  $F'(\lambda) > 0$ . Therefore, for  $\lambda > 1$ , we have an attracting equilibrium. When  $\lambda = 1$  the equilibrium is attracting from

the right (haline state), but repelling from the left (thermal state). All trajectories in the thermal state will eventually be returned to the haline state above the  $y$  nullcline. Since  $F'_-(1) > 1$ , we can assume  $[F'_-(1)]^2 > 4\delta_0$ , so the equilibrium will be a node. The proof of Theorem 2.3.5 (which is Theorem 3.5 in [46]) shows that all trajectories entering the haline state above the nullcline will be attracted to the equilibrium along the splitting line. This proves assertion (A). Also, when  $\lambda < 1$  we see that  $F'(\lambda) > 0$  if and only if  $\lambda < (1 + A)/(2A)$ . This proves assertion (C).

When  $(1 + A)/(2A) < \lambda < 1$ ,  $F'(\lambda) < 0$  and the equilibrium is unstable. If  $A < 1 + 2\sqrt{\delta_0}$ , then  $F'_+(1) < 2\sqrt{\delta_0}$  and the equilibrium will be an unstable focus near the fold. By Theorem 2.3.5, the bifurcation will create canard cycles as shown in Figure 3.5c. However, if  $A < 1 + 2\sqrt{\delta_0}$ , then  $F'_+(1) > 2\sqrt{\delta_0}$ . The bifurcation turns a stable node into an unstable node. Theorem 2.3.5 from the previous chapter indicates that this will be a super-explosion whereby a stable relaxation orbit (bounded away from the equilibrium) appears instantaneously upon bifurcation. The relaxation oscillation resulting from the super-explosion is depicted in Figure 3.5d.  $\square$

**REMARK 1.** *The bifurcation at  $\lambda = (1 + A)/(2A)$  is degenerate, and therefore Theorem 2.3.3 does not apply. When the slow nullcline intersects the critical manifold on the unstable branch, we will still have an attracting periodic orbit guaranteed by the Poincaré-Bendixson Theorem. However, whether the orbit is a canard cycle or a relaxation oscillation is undetermined.*

### 3.4. Separating the Forcing Terms

In the previous section we explored how incorporating a parameter as a slow dynamic variable can produce relaxation oscillations. In actuality, the parameter  $\mu$  was a ratio of two forcing parameters from system (3.3). In this section we explore what happens if the two forcing parameters are allowed to vary independently, with the goal of finding conditions under which the system exhibits relaxation oscillations. Using a similar nondimensionalization as the one that produces (3.4), we will consider

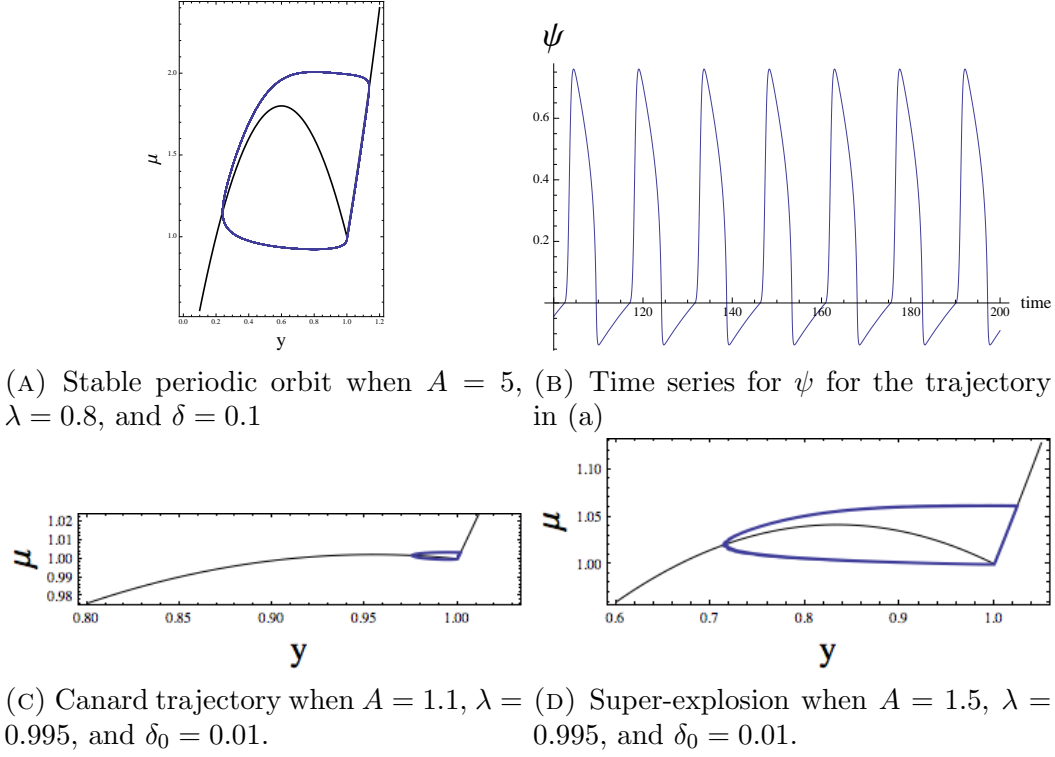


FIGURE 3.5. Oscillatory behavior in (3.12).

a system of the form

$$\begin{aligned}
 \frac{dx}{dt} &= z - x - \epsilon A |x - y| x \\
 \frac{dy}{dt} &= \epsilon(u - y - A |x - y| y) \\
 \frac{dz}{dt} &= \epsilon \delta (ay - bx + c) \\
 \frac{du}{dt} &= \epsilon \delta (px - qy + r),
 \end{aligned}
 \tag{3.14}$$

where  $0 < \epsilon, \delta \ll 1$ . The new model (3.14) is still a three time-scale system, with  $x$  fast,  $y$  intermediate, and  $z, u$  slow. As in the case with only one slow variable (3.9), we will be able to perform two reductions using GSP. The first reduction occurs as  $\epsilon \rightarrow 0$ . We see that the critical manifold is now the set

$$\{x = z\}$$

so the fast variable is slave to a slow variable. Similar to (3.9), this critical manifold is globally attracting, and the dynamics on the manifold are described by

$$\begin{aligned}
 (3.15) \quad & y' = u - y - A|z - y|y \\
 & z' = \delta(ay - bz + c) \\
 & u' = \delta(pz - qy + r).
 \end{aligned}$$

Note that in this reduced system, the circulation variable  $\psi = z - y$ , and the set  $\{y = z\}$  is the splitting surface.

**3.4.1. The Critical Manifold.** Define the function

$$F(y, z, u) = u - y - A|z - y|y.$$

Then the critical manifold

$$S = \{F(y, z, u) = 0\} = \{u = y + A|z - y|\}.$$

To determine where  $S$  is attracting, we consider

$$F_y = \begin{cases} -1 - A(z - 2y) & z > y \\ -1 - A(2y - z) & z < y \end{cases}.$$

Wherever  $F_x < 0$  (resp.  $F_x > 0$ ), the critical manifold  $S$  will be attracting (resp. repelling). When  $z < y$ , which corresponds to the haline circulation state ( $\psi < 0$ ), we have

$$\begin{aligned}
 -1 - A(2y - z) &< -1 - A(2z - z) \\
 &< 0.
 \end{aligned}$$

So the haline state is always attracting. When  $z > y$ , corresponding to the thermal state ( $\psi > 0$ ), we have

$$F_y < 0 \Leftrightarrow z > 2y - \frac{1}{A}.$$



The quantity  $A^{-1}$  will become important later, and we now define  $\rho = A^{-1}$ . The lines  $z = y$  and  $z = 2y - \rho$  intersect at the point  $(\rho, \rho)$ , producing a cusp on  $S$ . For all  $z < \rho$ ,  $S$  is stable. However for all  $z > \rho$ ,  $S$  is an ‘S’-shaped manifold, with two attracting branches and an unstable branch. We denote

$$S_A^- = \{z > 2y - \rho\} \cap \{z > \rho\}$$

$$S_R = \{y < z < 2y - \rho\}$$

$$S_A^+ = \{y > z > \rho\},$$

where the subscript  $A$  (resp.  $R$ ) indicates an attracting (resp. repelling) branch of  $S$ . The ‘fold lines’  $L^\pm$  separate  $S_A^\pm$  and  $S_R$ , where  $L^- = \{z = 2y - \rho : z > \rho\} \cap S$  is a smooth fold and  $L^+ = \{z = y : z > \rho\} \cap S$  is a corner. Therefore, we can write

$$S|_{z>\rho} = S_A^- \cup L^- \cup S_R \cup L^+ \cup S_A^+.$$

**3.4.2. The Reduced Problem and Singularities.** Since  $F_y$  is either zero or undefined on  $L^\pm$ , we cannot describe the critical manifold as  $\{y = h(z, u)\}$  where  $h$  is globally defined. Thus we cannot formulate the reduced problem in terms of only the variables  $z$  and  $u$ . However, we can utilize the fact that  $F_u \equiv 1$  to formulate the reduced problem in terms of  $y$  and  $z$ . That is, the reduced problem can be written as

$$-F_y \dot{y} = F_z \dot{z} + F_u \dot{u}$$

$$\dot{z} = ay - bz + c.$$

Still,  $F_y$  is defined piecewise, so we obtain different equations of the reduced problem for the thermal and haline states. In the thermal state ( $z > y$ ) we have the subsystem

$$\begin{aligned} (3.16) \quad [1 + A(z - 2y)]\dot{y} &= -Ay(ay - b + c) + (pz - qy + r) \\ \dot{z} &= ay - bz + c, \end{aligned}$$

and in the haline state ( $z \leq y$ ) we have the subsystem

$$(3.17) \quad \begin{aligned} [1 + A(2y - z)]\dot{y} &= Ay(ay - b + c) + (pz - qy + r) \\ \dot{z} &= ay - bz + c \end{aligned}$$

Note that these systems are defined on all of  $S$ , not just where  $z \leq \rho$ . These systems may have five different types of singularities:

- ordinary singularities—these are equilibria of (3.15)
- regular fold points—also called jump points,
- folded equilibria—these behave like equilibria in (3.16) but are not equilibria of (3.15)
- corner points—these behave like jump points for  $z > \rho$ .
- the cusp at  $(\rho, \rho)$ .

Note that fold points (either regular or folded equilibria) happen when the coefficient of  $\dot{y}$  is zero; this only happens in (3.16). We can rescale the time variable by  $[1 + A(z - 2y)]p^{-1}$  in the haline subsystem and  $p[1 + A(2y - z)]p^{-1}$  in the thermal subsystem to obtain the desingularized problem,

$$(3.18) \quad \begin{aligned} \dot{y} &= -\frac{A}{p}y(ay - b + c) + \left(z - \frac{q}{p}y + \frac{r}{p}\right) \\ \dot{z} &= \frac{1}{p}[1 + A(z - 2y)](ay - bz + c), \end{aligned}$$

and

$$(3.19) \quad \begin{aligned} \dot{y} &= \frac{A}{p}y(ay - b + c) + \left(z - \frac{q}{p}y + \frac{r}{p}\right) \\ \dot{z} &= \frac{1}{p}[1 + A(2y - z)](ay - bz + c). \end{aligned}$$

Defining

$$(3.20) \quad \begin{aligned} \gamma &= \frac{Ab}{p}, \quad \alpha = \frac{a}{b}, \quad \beta = \frac{q}{p}, \\ k &= \frac{r}{p}, \quad m = \frac{c}{b}, \end{aligned}$$

we can reformulate the subsystems (3.18) and (3.19) as

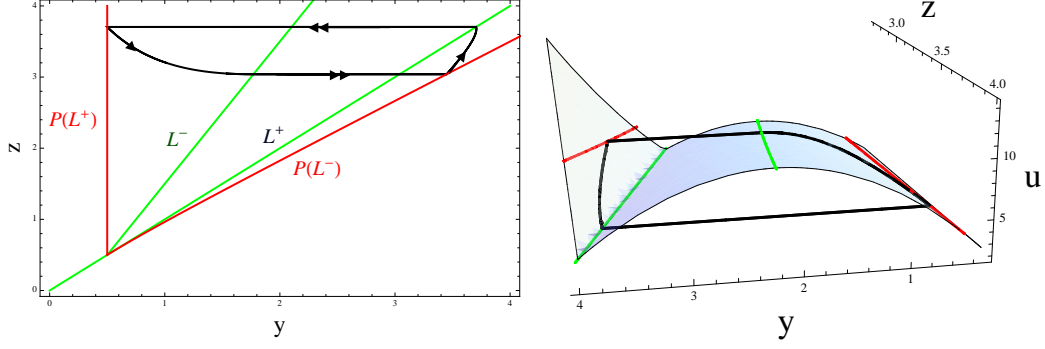
$$(3.21) \quad \begin{aligned} \dot{y} &= -\gamma y(\alpha y - z + m) + (z - \beta y + k) \\ \dot{z} &= \gamma(\rho - 2y + z)(\alpha y - z + m), \end{aligned}$$

and

$$(3.22) \quad \begin{aligned} \dot{y} &= \gamma y(\alpha y - z + m) + (z - \beta y + k) \\ \dot{z} &= \gamma(\rho + 2y - z)(\alpha y - z + m), \end{aligned}$$

respectively. In these systems it is easy to classify the different types of singularities. Ordinary singularities occur when  $(\alpha y - z + m) = 0 = (z - \beta y + k)$ . Folded equilibria occur when  $\dot{z} = 0$  due to the rescaling. Thus they are only possible in the thermal subsystem (3.21) (or equivalently (3.18)), occurring when  $(\rho - 2y + z) = 0$  and  $\dot{y} = 0$ . If  $(\rho - 2y + z) = 0$  but  $\dot{y} \neq 0$ , then the fold point is a regular fold point. Note that regular fold points are no longer singularities in (3.21), which is why we call it the desingularized problem. The haline subsystem has no fold points, so (3.22) is not truly a desingularized problem. We perform the rescaling in the haline subsystem so that the analysis is similar to that of the thermal subsystem.

Corner points occur when  $z = y$ . Even in the desingularized systems, the corner points are still singularities for  $z \leq \rho$  since the vector fields have different limits on either side of the split. The theory has not been developed to analyze exactly what happens in the case of a ‘corner equilibrium.’ That is, if the desingularized flow on either side of the corner is tangent to the corner, the dynamics are unclear. However, in the case that the desingularized flow crosses the corner in the same direction, then we know what trajectories will do so along the corner. If  $\dot{z} - \dot{y} > 0$  in both systems, the desingularized reduced flow sends trajectories from the haline to the thermal state along the fold. If  $\dot{z} - \dot{y} < 0$  in both systems, then the desingularized reduced flow sends trajectories from the thermal to haline state along the fold. The case we would like to avoid is the one where  $\dot{z} = \dot{y}$ . In the case of both systems (3.21) and (3.22),



(A) Projection of the singular orbit onto the critical manifold, with projections of space. Colored lines correspond to those in (a). (B) Singular orbit  $\Gamma$  in the full 3D phase space. Colored lines correspond to those in (a).

FIGURE 3.6. Example of a singular periodic orbit.  $\Gamma$  for  $\gamma = 1$ ,  $\alpha = 0.5$ ,  $\beta = 1.75$ ,  $m = 2$ ,  $\rho = 0.5$ , and  $k = 1.5$ .

we have

$$(3.23) \quad (\dot{z} - \dot{y})|_{\{z=y\}} = \gamma\rho[(\alpha - 1)z + m] + (\beta - 1)z - k.$$

Having trajectories cross the fold in the desingularized flow has different implications for different regions of  $S$ . When  $z < \rho$ , trajectories will cross in the way we expect. However for  $z > \rho$ , the corner is adjacent to  $S_R$  where trajectories have been reversed. Along the corner in this region, crossing in the desingularized system means trajectories are either directed towards the fold on both sides or away from the fold on both sides in the actual system (3.15). Therefore, the corner will behave as a standard jump point.

**3.4.3. Strategy.** In order to show that the model (3.15) exhibits relaxation oscillations, we need to construct a singular periodic orbit  $\Gamma$ , consisting of heteroclinic orbits of the layer problem and a segment on each of the stable branches  $S_A^\pm$ . The heteroclinic orbits consist of trajectories that connect a fold  $L^\pm$  to its projection  $P(L^\pm)$  on the opposite stable branch. An example of a singular periodic orbit  $\Gamma$  is shown in Figure 3.6. The following theorem due to Szmolyan and Wechselberger [63] provides conditions under which  $\Gamma$  perturbs to a relaxation oscillation in a smooth system of 3 variables.

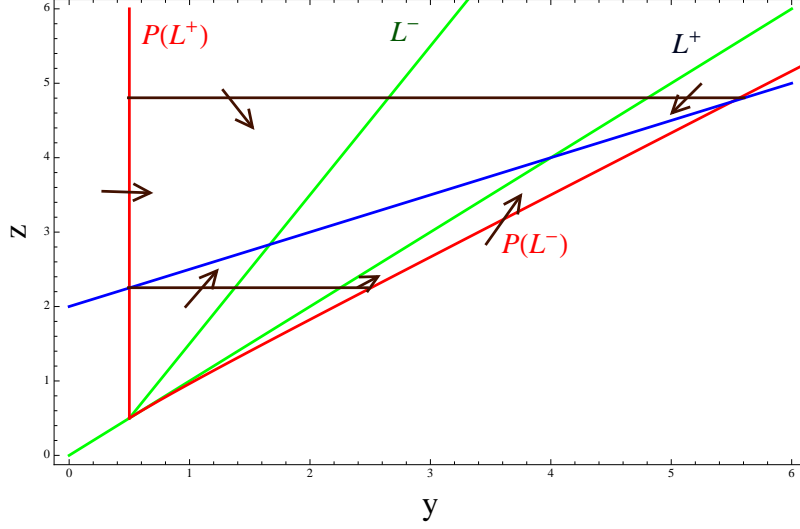


FIGURE 3.7. Existence of a stable singular periodic orbit. The blue line is the  $z$  nullcline. The regions between  $P(L^\pm)$  and  $L^\mp$  are locally positively invariant, so there must be a stable singular periodic orbit.

THEOREM 3.4.1. *Assume a fast/slow system with small parameter  $0 < \epsilon \ll 1$  satisfies the following conditions:*

- (A1) *The critical manifold is ‘S’-shaped,*
- (A2) *the fold curves  $L^\pm$  are given as graphs  $(y^\pm(z), z, u^\pm(z))$  for  $y \in I^\pm$  for certain intervals  $I^\pm$  where the points on the fold curves  $L^\pm$  are jump points,*
- (A3) *the reduced flow near the fold curves is directed towards the fold curves,*
- (A4) *the reduced flow is transversal to the curve  $P(L^\pm)|_{I^\pm} \subset S_A^\mp$ , and*
- (A5) *there exists a hyperbolic singular periodic orbit  $\Gamma$ .*

*Then there exists a locally unique hyperbolic relaxation orbit close to the singular orbit  $\Gamma$  for  $\epsilon$  sufficiently small.*

Currently, there is no analog for this theorem that applies to piecewise-smooth systems. We will find conditions such that (3.15) satisfies (A1)–(A5) by showing that the dynamics appear as in Figure 3.7. While this will demonstrate the existence of a singular periodic orbit  $\Gamma$ , it will not constitute a rigorous proof that (3.15) exhibits relaxation oscillations because the vector field of (3.15) is not smooth.

We have already shown that the critical manifold  $S$  is ‘S’-shaped for  $z > \rho$ , so (A1) is satisfied. Clearly, we can write the fold curves as graphs for  $z > \rho$ . Next, we find conditions so that there are no folded equilibria on the smooth fold  $L^-$ .

LEMMA 3.4.2. *Assume that*

- (a)  $0 < \alpha < 1$  and
- (b)  $k > \gamma\rho^2(\alpha - 1) + (\gamma m + \beta - 1)\rho$ .

*Then (3.21) has no folded equilibria for  $z > \rho$ .*

PROOF. Folded equilibria occur when the line  $z = 2y - \rho$  intersects the parabola  $-\gamma y(\alpha y - z + m) + (z - \beta y + k) = 0$  for some  $z > \rho$ . Therefore, at folded equilibrium we have

$$\gamma(2 - \alpha)y^2 + [2 - \beta - \gamma(\rho + m)]y + k - \rho = 0.$$

So, the  $y$  coordinates of the intersections are

$$y_{\pm} = \frac{\gamma(\rho + m) + \beta - 2 \pm \sqrt{[\gamma(\rho + m) + \beta - 2]^2 - 4\gamma(2 - \alpha)(k - \rho)}}{2\gamma(2 - \alpha)}.$$

Algebraic manipulation shows that  $y_+ < \rho$  precisely when

$$k > \gamma\rho^2(\alpha - 1) + (\gamma m + \beta - 1)\rho.$$

□

REMARK 2. *In fact, we only need  $\alpha < 2$  to prove Lemma 3.4.2. The stricter condition  $\alpha < 1$  will be required for the next lemma.*

Lemma 3.4.2 provides conditions so that (A2) is satisfied. Next, we find conditions so that (A3) – (A4) are satisfied. In order to do so, we need to find equations for  $P(L^{\pm})$ .  $P(L^-)$  is the projection of the line  $y = (z + \mu)/2$  onto  $S_A^+ = \{u =$

$y + \rho^{-1}(y - z)y\}$ . Therefore we want

$$\begin{aligned} u &= \frac{z + \rho}{2} + \frac{z + \rho}{2\rho} \left( \frac{z - \rho}{2} \right) \\ &= \frac{(z + \rho)^2}{4\rho}. \end{aligned}$$

Plugging this back into the equation for  $S_A^+$  we see that  $P(L^-)$  is the curve

$$(3.24) \quad y = \frac{z - \rho + \sqrt{2(z^2 + \rho^2)}}{2}$$

on  $S_A^+$ . Similarly,  $P(L^+)$  is the projection of the line  $y = z$  onto  $S_A^- = \{u = y + \rho^{-1}(z - y)y\}$ . Therefore, on  $P(L^+)$  we have  $u = z$ . From this we see  $P(L^+)$  is the line  $y = \rho$  on  $S_A^-$ . We define  $z_*$  to be the  $z$  coordinate of the intersection of the  $z$  nullcline  $z = \alpha y + m$  with the curve  $P(L^-)$ , which will play an important role in constructing locally invariant sets.

LEMMA 3.4.3. *Assume conditions (a)-(b) from Lemma 3.4.2. Define  $R^-$  to be the region bounded by  $P(L^+)$  on the left,  $L^-$  on the right, the line  $z = \alpha\rho + m$  below, and the line  $z = z_*$  above. Also assume*

(c)  $m > (1 - \alpha)\rho$ .

*Then, the vector field of (3.21) is transverse to  $P(L^+)$ , and  $R^-$  is locally positively invariant.*

PROOF. Since  $z > \rho$  on  $P(L^+)$

$$\begin{aligned} \dot{y}|_{\{y=\rho\}} &= -\gamma\rho(\alpha\rho - z + m) + z - \beta\rho + k \\ &> -\gamma\rho[(\alpha - 1)\rho + m] + (1 - \beta)\rho + k. \end{aligned}$$

Therefore, (b) implies  $\dot{y}|_{\{y=\rho\}} > 0$  and the vector field is transverse to  $P(L^+)$ .

Conditions (a) and (c) guarantee that the  $z$  nullcline will intersect  $L^-$ . Below the nullcline the vector field points upward, and above it points downward. Therefore, the vector field points into  $R^-$  along all boundaries except (possibly) the fold  $L^-$ .

The only way to leave  $R^-$  is by hitting the fold and jumping to  $S_A^+$ , so  $R^-$  is locally positively invariant.  $\square$

Next, we show a similar result for the analogous region  $R^+$  on  $S_A^+$ .

LEMMA 3.4.4. *Assume conditions (a)-(c) from Lemmas 3.4.2-3.4.3. Define  $R^+$  to be the region bounded by  $P(L^-)$  on the right,  $L^+$  on the left, the line  $z = \alpha\rho + m$  below, and the line  $z = z_*$  above. Also assume*

(d)  $k < (\beta - 1)(\alpha\rho + m)$ , and

(e)  $1 < \beta < 2$ .

*Then the vector field of (3.22) is transverse to  $P(L^-)$ , and  $R^+$  is locally positively invariant.*

PROOF. Conditions (a)-(c) imply that the line  $z = \alpha\rho + m$  lies below the  $z$  nullcline on  $S_A^+$ , so the vector field points into  $R^+$  here. The line

$$z = \frac{m}{1 - \alpha}$$

is the  $z$ -coordinate of the intersection of the  $z$  nullcline with  $P(L^-)$ . Therefore the line lies above the nullcline and the vector field points down into  $R^+$ .

Showing that the vector field points into  $R^+$  on  $P(L^-)$  is slightly more difficult, and to do so we need to use the slopes of the tangent lines along  $P(L^-)$ . Differentiating (3.24) we get

$$\begin{aligned} 2dy &= \left( 1 + \frac{2z}{\sqrt{2(z^2 + \rho^2)}} \right) dz \\ &= \frac{2y + \rho + z}{2y + \rho - z} dz. \end{aligned}$$

This tells us that the vector field points upward into  $R^+$  if

$$(2y + \rho + z)\dot{z} - 2(2y + \rho - z)\dot{y} > 0.$$



Plugging in  $\dot{z}$  and  $\dot{y}$  from (3.22), this condition simplifies to

$$\gamma(\alpha y - z + m)(\rho + z) - 2(z - \beta y + k) > 0.$$

The first term on the LHS is positive since the  $z$  nullcline lies above  $P(L^-)$  on the interval under consideration. Therefore it is sufficient to show that the line  $z = \beta y - k$  lies above the  $P(L^-)$  as well. Since  $\beta > 1$  this can be done by showing that the line  $z = \beta y - k$  crosses the corner  $L^+$  to for some  $y < \alpha\rho + m$  (or equivalently  $z < \alpha\rho$ ). This happens precisely when  $k < (\beta - 1)(\alpha\rho + m)$ .  $\square$

REMARK 3. *Again, the conditions of Lemma 3.4.4 are more strict than required to prove the lemma. In particular, we only need  $\beta > 1$ —not  $\beta < 2$ . The stricter conditions will be used to show the lack of a stable equilibrium on  $S_A^\pm$  in the following lemma.*

We have constructed two locally positively invariant regions as shown in Figure 3.7. Once a trajectory reaches  $R^\pm$  the only way it can leave is by hitting the fold at a jump point, where the fast dynamics will take it from  $R^\pm$  to  $R^\mp$ . In fact, unless there is a stable critical point in  $R^\pm$ , the only possibility is for trajectories to reach the folds.

LEMMA 3.4.5. *Under the conditions (a)-(e) of Lemmas 3.4.2-3.4.4, the only critical points of the systems (3.21)-(3.22) will lie on  $S_R$ .*

PROOF. If the line  $z = \beta y - k$  crosses the corner  $z = y$  to the right of the cusp (i.e. for  $y, z > \rho$ ), then it will be trapped in the unstable region since  $\beta < 2$ . Furthermore, it will enter the unstable region below the  $z$  nullcline, so its only intersection with the  $z$  nullcline will be on the unstable branch. This happens when

$$k > (\beta - 1)\rho,$$

but that is already guaranteed by conditions (b) and (c).  $\square$

### 3.4.4. Evidence of Stable Relaxation Orbit.

CONJECTURE 3.4.6. *Assume (3.15) satisfies (a)-(e) of Lemmas 3.4.2-3.4.4. Then (3.15) there exists a singular periodic orbit  $\Gamma$  and an attracting relaxation orbit close to  $\Gamma$  for  $\delta$  sufficiently small.*

Lemmas 3.4.2, 3.4.3, and 3.4.5 imply that  $R^-$  is a locally positively invariant set containing no critical points. Since there are no equilibria along the fold (where  $\dot{z} = 0$ ), we know  $\dot{y} \neq 0$  and that the fold consists only of jump points in  $R^-$ . When combined with the fact that  $\dot{y} > 0$  at the intersection of the fold with the line  $y = \rho$ , we know that the flow must be directed at the fold in  $R^-$ . Also, from Lemmas 3.4.2, 3.4.4, and 3.4.5 we know that  $R^+$  is a positively locally invariant set with no critical points. Using equation (3.23), we see that condition (e) implies the flow will be directed at the corner in  $R^+$  and that the corner will behave like regular fold points (i.e. jump points). We define the intervals  $I^\pm = L^\pm \cap R^\pm$

We define the following maps:

$$\pi_- : P(L^+)|_{R^-} \rightarrow L^-$$

$$\pi^- : \text{Im}(\pi_-) \rightarrow P(L^-)$$

$$\pi_+ : \text{Im}(\pi^-) \rightarrow L^+$$

$$\pi^+ : \text{Im}(\pi_+) \rightarrow P(L^+)$$

where  $\pi_\pm$  are the maps induced by the reduced flow, and  $\pi^\pm$  are the maps induced by the layer problem. Furthermore we define  $\Pi : P(L^+) \rightarrow P(L^+)$  by

$$\Pi = \pi^+ \circ \pi_+ \circ \pi^- \circ \pi_-.$$

Through the use of Wazewski maps, we see that  $\Pi(L^+) \subset L^+$ . By uniqueness of solutions of the flow gives, we see that for any two points  $P, Q \in P(L^+)|_{R^-}$ , there is a  $K < 1$  such that

$$|\Pi(P) - \Pi(Q)| < K|P - Q|.$$

Therefore  $\Pi$  is a contraction, so it has a unique fixed point. The fixed point corresponds to a singular periodic orbit  $\Gamma$  and  $\Pi$  is the Poincaré map. Furthermore, since  $\Pi$  is a contraction,

$$\lim_{P \rightarrow Q} \Pi'(Q) \leq K < 1,$$

so  $\Gamma$  is hyperbolic.

This shows that under the conditions (a)-(e), (3.15) satisfies the assumptions (A1) – (A5) of Theorem 3.4.1. In order to prove our conjecture, we would need to show that Theorem 3.4.1 generalizes to piecewise-smooth systems. We leave this to future work and provide further justification by simulating the model. Figure 3.9 depicts a stable periodic orbit near the singular orbit in Figure 3.6. Figure 3.8 shows portions of phase space that satisfy conditions (a)-(e).

**3.4.5. Lack of a Periodic Orbit with only One Relaxation Phase.** Since the critical manifold  $S$  has a cusp, it is theoretically possible to have a periodic orbit  $\Gamma'$  with exactly one relaxation phase, where the slow dynamics flow the orbit around the cusp. In order for such an orbit to relate to D-O events, the relaxation phase should be a rapid transition from the haline to the thermal state. However this is not possible in our model if parameters have physically meaningful values (i.e.,  $\alpha$ ,  $\beta$ ,  $k$ , and  $m$  positive), and we will demonstrate that here.

**THEOREM 3.4.7.** *There is no periodic orbit in system (3.15) that contains exactly one relaxation phase characterized by a rapid transition from the haline state to the thermal state.*

**PROOF.** Such a periodic orbit requires that the vector field point left somewhere on  $P(L^+) = \{y = \rho\}$ . Since the restriction of  $\dot{y}$  to  $P(L^+)$  is an increasing function of  $z$ , a necessary condition for  $\Gamma'$  is that the vector field (3.21) points left at the cusp  $(\rho, \rho)$ . This happens when

$$(a') \quad 0 < k < \gamma\rho[(\alpha - 1)\rho + m] + (\beta - 1)\rho.$$

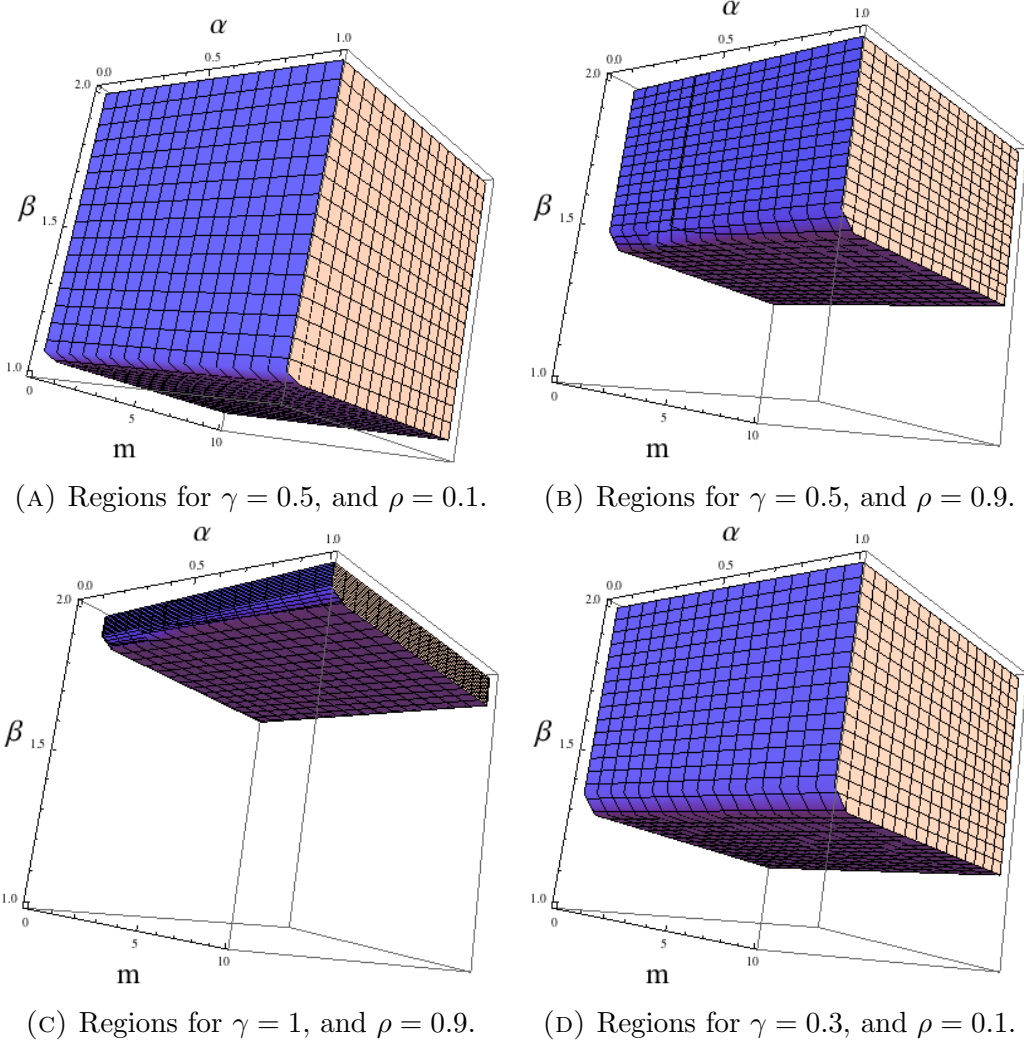
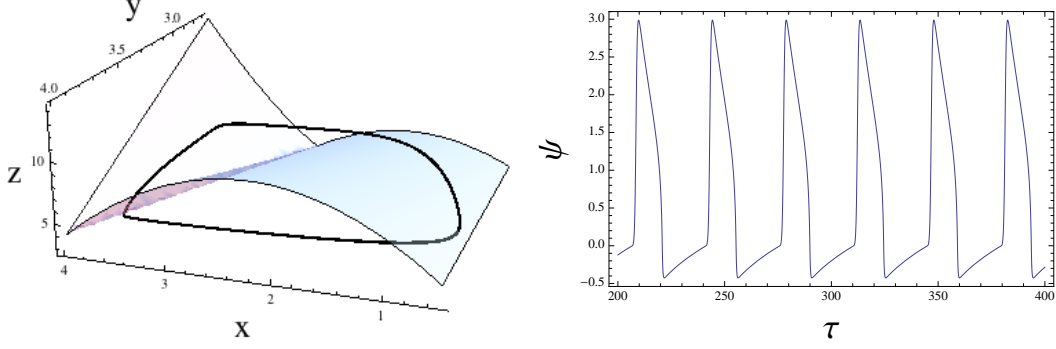


FIGURE 3.8. Regions of phase space that satisfy conditions (a)-(e).

Next, we consider the position of the  $z$  nullcline. The requirement that  $k, m > 0$  implies that the line  $z = \alpha y + m$  lies above the line  $z = \beta y - k$  near  $y = 0$ . They will intersect if and only if  $\beta > \alpha$ . In the event they do intersect, the point of intersection will be a critical point of the reduced flow (and the full system), and it will occur for some  $y = y_0 > 0$ . We can calculate the stability of this critical point by looking at the Jacobian of the subsystem where the intersection occurs. The Jacobian in the thermal subsystem (3.21) is

$$J_T(y_0, z_0) = \begin{pmatrix} -\gamma\alpha y_0 - \beta & \gamma y_0 + 1 \\ \gamma\alpha(z_0 - 2y_0 + \rho) & -\gamma(z_0 - 2y_0 + \rho) \end{pmatrix}.$$



(A) The stable periodic orbit in phase space. (B) Time series for  $\psi$  for the orbit in (a).

FIGURE 3.9. Example of the 3D stable periodic orbit.  $\delta = 0.1$ ,  $\gamma = 1$ ,  $\alpha = 0.5$ ,  $\beta = 1.75$ ,  $m = 2$ ,  $\rho = 0.5$ , and  $k = 1.5$ .

If the intersection happens on the attracting branch of  $S$  in the thermal state, then  $z_0 - 2y_0 + \rho > 0$ . Therefore it is easy to see that the trace  $\text{Tr}(J_T) < 0$ . Also the determinant  $\det(J_T) = \gamma(\beta - \alpha)(z_0 - 2y_0 + \rho) > 0$ , so the equilibrium is attracting if it lies on the stable branch. A similar calculation shows that any critical points on in the haline state will be attracting as well. Therefore, in order to obtain the orbit  $\Gamma'$ , we either need all critical points (if any exist) to lie on the unstable branch. This has important consequences for the dynamics on the stable branches.

There are two possibilities for the  $z$  nullcline: either it intersects the line  $y = \rho$  above the cusp or it intersects below the cusp. We will show that both possibilities preclude the existence of an orbit such as  $\Gamma'$ . First, suppose the  $z$  nullcline intersects  $y = \rho$  above the cusp. We know from the lack of critical points on  $S_A^-$  that the line  $z = \beta - k$  lies below the  $z$  nullcline for all  $y < \rho$ . Therefore the vector field points to the right along the  $z$  nullcline. This implies that somewhere between the cusp and the  $z$  nullcline, the vector field switches from pointing left to point right along  $P(L^+)$ . All trajectories that land on  $P(L^+)$  in the region where the vector field points left lie below the  $z$  nullcline, and therefore the flow takes them up and the left. However, they are unable to turn downwards since they are bounded below the  $z$  nullcline, so they forced to cross  $P(L^+)$  above the cusp. Upon doing so they enter the invariant

region  $R^-$  and are prevented from ever crossing from the thermal state to the haline state below the cusp.

Second, we consider the case where the  $z$  nullcline crosses the line  $y = \rho$  below the cusp. This implies that  $\alpha < 1$ , and the  $z$  nullcline never enters the unstable region. Since any critical point will be attracting, we require  $\beta < \alpha < 1$  to ensure that no critical points will exist. However, this contradicts condition (a'), since the RHS is negative.  $\square$

### 3.5. Discussion

Incorporating the environmental forcing parameters as dynamic variables in Stommel's 1961 thermohaline circulation model produces a relaxation oscillator. Stommel would not have seen this since his model is based on a tangible experiment—a rarity in climate science—in which the environment that forced the system was not actually a gaseous atmosphere but rather baths of water with prescribed temperatures and salinities. As demonstrated by Theorems 3.3.1 and 3.4.6, the relaxation oscillation is present regardless of whether the forcing parameters are incorporated together as a single slow variable or allowed to vary independently. Indeed, the time series for  $\psi$  with only one slow variable, shown in Figure 3.5b, is remarkably similar the time series found in Figure 3.9b. Both figures appear to be qualitatively similar to Figure 3.1, including the asymmetric nature of the behavior within the stable states.

In both cases, the key to generating relaxation oscillations in the model is the (non-smooth) 'S'-shaped  $y$  nullcline. In the model with a 1D critical manifold, the 'S'-shape relies on the parameter  $A > 1$ . In the model (3.15) where the critical manifold is a surface, it will always have a bistable, 'S'-shaped region. However, we were unable to find any parameter regime with  $\rho > 1$  (corresponding to  $A < 1$ ) in which the model exhibited relaxation oscillations. Although it is not entirely clear from conditions (a)-(e) of Theorem 3.4.6 that this should be the case, the picture for  $\rho > 1$  analogous to those of Figure 3.8 is just an empty box.

In some sense, this chapter is a case study for the usefulness of conceptual models. We have demonstrated that two conceptual models produce a qualitative pattern similar to the paleoclimate data. The qualitative difference in output between our two models appears negligible, suggesting that the simpler model is ‘good enough.’ Additionally, we are able to find the requirement that  $A > 1$  analytically. Furthermore, we see *why* it is required; there is only one stable state when  $A < 1$ .

Since the limit cycle is seen in the reduced system (3.10), the oscillation can be described by a system with two degrees of freedom, which is the minimum requirement for an oscillator. Aside from the non-differentiability due to the absolute value term, the equations are relatively simple. In reality, the non-smooth nature of the vector field is fortuitous since the necessary ‘S’ shape of the critical manifold comes from the lack of differentiability of the absolute value function. If the critical manifold were a smooth cubic, the system would be indistinguishable from the van der Pol system. In fact, that is the way scientists have assumed (3.7) would behave, despite the GSP theory breaking down at one of the jump points. In essence, this provides rigorous justification for that assumption.

## CHAPTER 4

# Mixed-mode Oscillations in a Conceptual Climate Model

### 4.1. Introduction

There has been a significant amount of research aimed at explaining oscillations in various historical periods of the climate system. Crucifix surveys some of the work on oscillators found in conceptual climate models in [12]. Maasch and Saltzman have a series of papers on the Mid-Pleistocene transition, a change from oscillations with a dominant period of 40 kyr to oscillations with a dominant period of 100 kyr [52, 53, 54]. Paillard and Parrenin also seek to explain the Mid-Pleistocene transition and the glacial-interglacial cycles of the late Pleistocene, with a discontinuous and piecewise linear model [42]. Their work, and the work of Hogg [28], use Milankovitch forcing—changes in solar forcing due to variation in the Earth’s orbit—to generate oscillations. However the vast majority of research on oscillations in climate data has focused on relaxation oscillations or some other mechanism that only explains oscillations of a single amplitude [52, 53, 54].

Looking at Figure 4.1, each 100 kyr cycle contains a sharp increase leading into the interglacial period (denoted by the red spikes). This relaxation behavior clearly indicates the existence of multiple time-scales in the underlying problem. There are also smaller, structured oscillations in the glacial state that are repeated in each 100 kyr cycle. The presence of the large relaxation oscillation and the small amplitude oscillations suggests that these are mixed-mode oscillations (MMOs)—a pattern of  $L_1$  large amplitude oscillations (LAOs) followed by  $s_1$  small amplitude oscillations (SAOs), then  $L_2$  large spikes,  $s_2$  small cycles, and so on. The sequence  $L_1^{s_1} L_2^{s_2} L_3^{s_3} \dots$  is known as the MMO signature. A reasonable expectation for a model that claims to



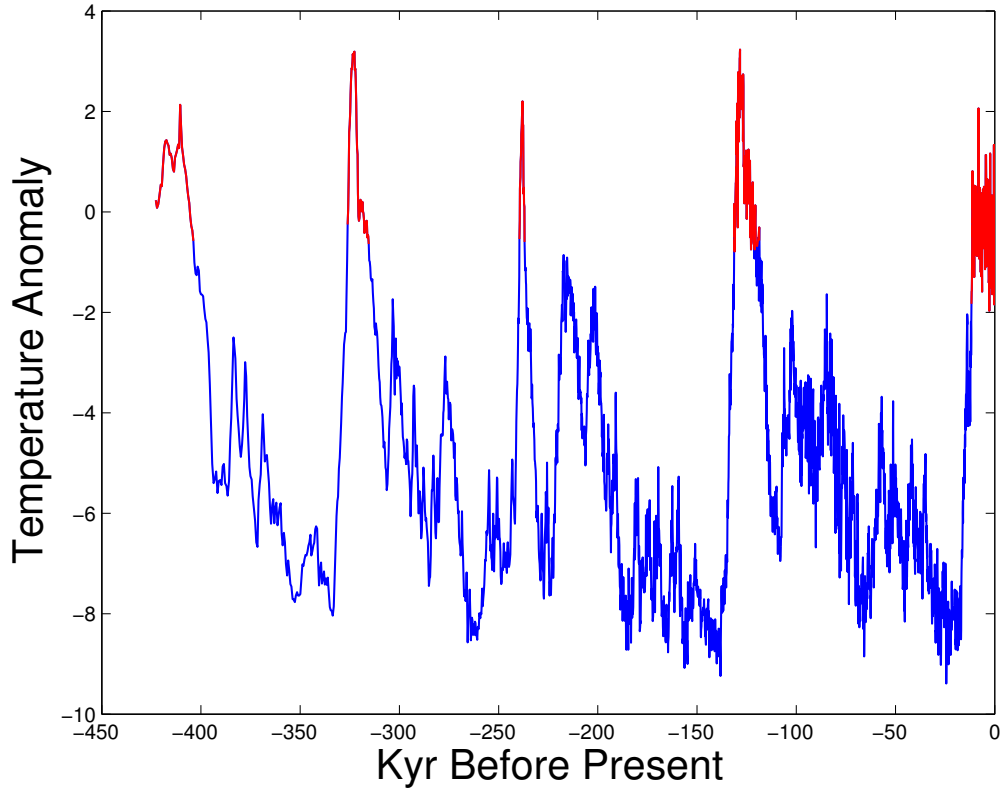


FIGURE 4.1. Temperature record depicting interglacial periods [43].

explain the 100 kyr glacial-interglacial cycles would be to explain the largest of the SAOs—i.e., the largest cycles that do not enter the interglacial state.

This chapter tests the scientific hypothesis that oscillatory behavior in climate data can be interpreted as MMOs, and we take the data in Figure 4.1 as a case study. Desroches et al. survey the mechanisms that can produce MMOs in systems with multiple time-scales [14]. From the data set shown in Figure 4.1, we know that the underlying model has a multiple time-scale structure. If we want to find MMOs, the model must have at least three state variables. Assuming we can find a global time-scale splitting, there are three distinct ways to have a 3D model with multiple time scales: (a) 1 fast, 2 slow; (b) 2 fast, 1 slow; and (c) 1 fast, 1 intermediate, 1 slow (i.e., a three time-scale model). Each of these options can create MMOs through different mechanisms. Models with 1 fast and 2 slow variables can create MMOs through a folded node or folded saddle-node with a global return mechanism that

repeatedly sends trajectories near the singularities. Models with 1 slow and 2 fast variables can create MMOs through a delayed Hopf mechanism that also requires a global return. MMOs in three time-scale models are reminiscent of MMOs due to a folded saddle-node type II—where one of the equilibria is a folded singularity—although the amplitudes of the SAOs are more pronounced in this case.

To verify our hypothesis, we have to strike a delicate balance. The model needs to be complex enough to exhibit the desired behavior, but if it is too complex we will be unable to *prove* that it does so. It is clear from [11] that temperature and atmospheric carbon should be two variables in any model that describes glacial-interglacial cycles. We consider a physical, conceptual model that incorporates these two components of the climate system as well as oceanic carbon. Since this approach has never been used in a climate-based model, our desire is that the analysis is clear enough to replicate. This is a major reason for our choice of such a simplistic 3D model. Indeed, we omit time-dependent forcing such as Milankovitch cycles, leaving these effects to future work. Even so, a minimal model is able to provide insight into key mechanisms behind the MMOs. We include oceanic carbon as the third variable because the model was able to produce MMOs. However, we were unable to find MMOs in other minimal models with, for example, deep ocean temperature.

We know from the data shown in Figure 4.1 that temperature ( $T$ ) shows relaxation behavior, so we can assume that  $T$  is a fast variable within our conceptual model. The main task is to obtain the “global” time-scale separation between the temperature evolution and the evolution of the carbon equations denoted by  $\epsilon_1$  and  $\epsilon_2$ . In general, a time-scale separation can be revealed through dimensional analysis. The process should relate a small parameter  $\epsilon_i$  to physical parameters of the dimensional model. In applications such as neuroscience, it is often possible to get a handle on the “smallness” of the  $\epsilon_i$  because there are accepted values or ranges for many of the physical parameters. Unfortunately, parameters in paleoclimate models are not

as constrained. We rely on the intuition of physicists, geologists, and atmospheric scientists to determine a reasonable separation of time-scales.

While it may be unsettling to not have a more concrete argument, the ambiguity regarding parameter values—and even the governing equations—allows more freedom. With this in mind we take a different approach than is often sought in the paleoclimate literature. In the vast majority of climate science papers, the authors simulate models with judiciously chosen parameters. Our approach is different in that we assume nothing about any parameters except that they are physically meaningful. Then, through the analysis, we find conditions under which the model behaves qualitatively like the data. The idea is not to pinpoint specific parameter values, but to find a range of possible parameters. There are two advantages to this approach. First, the parameter range can be used to constrain (or maybe constrain further) previous parameter estimates, which may tell us something previously unknown about the climate system. It can be used to inform parameter choices for large simulations. Second, a parameter range is useful to eliminate options. That is, if the only parameter range which produces the correct qualitative behavior is entirely unreasonable, the model needs to be changed.

The outline of the paper is as follows: In section 2 we set up the model and provide relevant background from the paleoclimate literature. Then we nondimensionalize the model and discuss assumptions on some of the parameters. We analyze the dimensionless model in section 3, with a focus on finding conditions for MMOs. We conclude with a discussion in section 4.

## 4.2. Setting up the Model

We start with a model of the form

$$(4.1) \quad \frac{dT}{dt} = \frac{1}{C_p} [Q(1 - \alpha(T)) - (B_0 - B_1A + B_2T)]$$

$$(4.2) \quad \frac{dA}{dt} = B_3[P(T - T_*)^2 - B_4 - A] - (L + B_5A - B_6H)$$

$$(4.3) \quad \frac{dH}{dt} = L + B_5A - B_6H.$$

$T$  is globally averaged temperature in degrees Celsius,  $A$  is PgC (Petagrams of Carbon) in the atmosphere, and  $H$  is PgC in the mixed layer of the ocean. Often atmospheric carbon is discussed as carbon concentration in the atmosphere in ppm (parts per million) [6]. However when discussing land-atmosphere flux, as we will do, it makes sense to discuss carbon in terms of mass, hence the choice of PgC [59]. Equation (4.1) is a minor variant of the standard global energy balance equation due to Budyko [5] and Sellers [57].  $C_p$  is planetary heat capacity and  $Q$  is the total incoming solar radiation—abbreviated “insolation” in the climate literature—that reaches the Earth. The albedo,  $\alpha(T)$  is the proportion of this incoming shortwave radiation that is immediately reflected back to space. The functional dependence of albedo on temperature will be explored shortly. Since whatever radiation is not

Variable/Parameter	Unit	Parameter	Unit
$t$	$yr$	$B_0$	$Wm^{-2}$
$T$	$K$ (Kelvin)	$B_1$	$Wm^{-2}PgC^{-1}$
$A$	$PgC$	$B_2$	$Wm^{-2}K^{-1}$
$H$	$PgC$	$B_3$	$yr^{-1}$
$C_p$	$JK^{-1}m^{-2}$	$B_4$	$PgCyr^{-1}$
$Q$	$Wm^{-2}$	$B_5$	$yr^{-1}$
$\alpha_1$	1	$B_6$	$PgCyr^{-1}$
$\alpha_2$	1	$P$	$PgCK^2$
$T_*, \tilde{T}$	$K$	$L$	$PgCyr^{-1}$

TABLE 1. Summary of the parameters, variables and their units.

reflected must be absorbed, the quantity  $Q(1 - \alpha(T))$  is the absorbed insolation. The  $(B_0 - B_1A + B_2T)$  term is the linearized outgoing longwave radiation. The amount of heat radiated by a blackbody is proportional to its temperature to the fourth power ( $T^4$ ). Due to atmospheric greenhouse gases, however, the Earth does not radiate heat as a perfect blackbody. It is a standard practice in paleoclimate to linearize the outgoing radiation term [64] as

$$(4.4) \quad \tilde{A} + BT,$$

where the dependence on atmospheric greenhouse gases is implicitly built into  $\tilde{A}$ .

While the climate system is far more complicated than merely a stable temperature, one can think of a climate as a fixed point of equation (4.1). These fixed points occur precisely when there is an energy balance, i.e. when the absorbed insolation is equal to the outgoing longwave radiation. Clearly, the values of  $T$  for which fixed points occur depend on the nonlinear albedo function,  $\alpha(T)$ . In general, the albedo function is unknown and the subject of current research. What is known is that ice reflects much more radiation than land or water, so the average albedo of a cold Earth should be much higher than that of a warm Earth. However, many other factors such as clouds and vegetation affect the albedo as well, albeit in a manner that is not entirely understood. For the purposes of paleoclimate models, the albedo is often taken to be a step function [1, 64] or a piecewise linear ramp function [29]. When smoothness of the vector field is required, a hyperbolic tangent may be used [69]. Since our analysis will require continuous derivatives, we have taken

$$(4.5) \quad \alpha(T) = \frac{\alpha_M + \alpha_m}{2} - \frac{\alpha_M - \alpha_m}{2} \tanh\left(\frac{T - \tilde{T}}{D}\right),$$

where  $\alpha_M$  and  $\alpha_m$  are the maximum and minimum planetary albedos, respectively, and  $\tilde{T}$  is half the activation temperature of  $\alpha$ . Figure 4.2 plots the absorbed radiation (for  $\alpha(T)$  modeled with a hyperbolic tangent) and outgoing radiation. A quick examination of Figure 4.2 shows that there are two stable climates ( $T_w$ ,  $T_c$ ) and

## Radiation

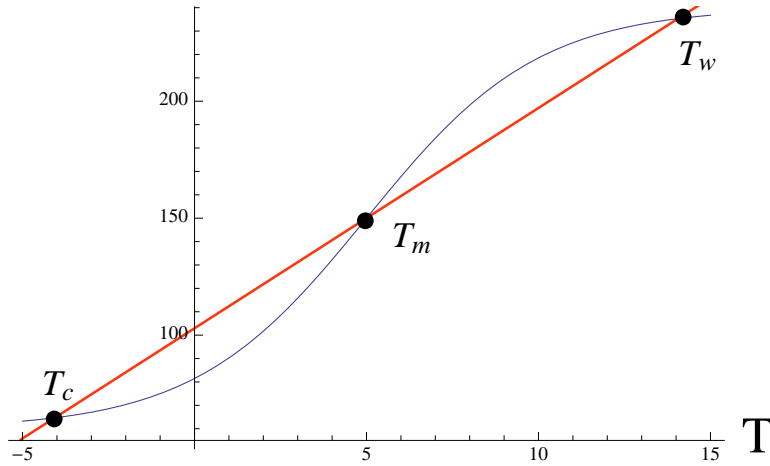


FIGURE 4.2. Energy balance. The blue curve represents absorbed incoming shortwave radiation as a function of temperature. The red line is the linearized outgoing long wave radiation. Intersections of these curves ( $T_w$ ,  $T_m$ ,  $T_c$ ) represent energy balance (i.e., stable climates).

an intermediate unstable climate ( $T_m$ ). The standard energy balance equation that leads to (4.1) is one of the paradigmatic sources of bistability in conceptual climate models. This bistability plays an important role in demonstrating the capability for MMOs.

As mentioned previously, the outgoing radiation term is usually linearized as in (4.4). Our variation,  $(B_0 - B_1A + B_2T)$ , explicitly includes a dependence of outgoing radiation on atmospheric greenhouse gases  $A$ —also known as climate sensitivity. This allows us to include  $A$  as a state variable that evolves according to (4.2). Equation (4.2) can be decomposed into two terms: the land-atmosphere flux,

$$B_3[P(T - T_*)^2 - B_4 - A],$$

and the ocean-atmosphere flux

$$L + B_5A - B_6H.$$

Notice that the ocean-atmosphere flux is balanced in equation (4.3). That is, whatever carbon is outgassed from (or absorbed by) the ocean must be transferred to (or from)

the atmosphere. While the ocean has numerous carbon reservoirs of various sizes (e.g. the mixed layer and the deep ocean [59]), we assume that the carbon exchange between atmosphere and ocean follows a simple linear equation as described in [58]. The air-sea exchange of carbon is temperature dependent [37]; in our model this means that the coefficients  $B_5$  and  $B_6$  may depend on temperature, but for the sake of simplicity, we suppress this dependence.

The terrestrial, or land-atmosphere, flux depends on plants (among other things) [38]. Therefore, the carbon drawdown is most efficient at  $T_*$ , the temperature at which  $\text{CO}_2$ -absorbing life is most prolific. As a testament to how difficult it is to pin down actual parameter values for climate models, especially in paleoclimate problems, we point to the literature with regards to  $T_*$ . In [38], Lenton and Huntingford state that  $T_*$  should be a temperature in the warm, interglacial state (i.e.  $T_* \approx T_w$ ). That is, carbon drawdown should be most effective during the large spikes in Figure 4.1. However in [40], Lovelock calls the interglacial states “fevers,” suggesting that carbon drawdown is most efficient in the climate’s “natural,” glacial state (i.e.  $T_* \approx T_c$ ).

The reason there is no governing equation for terrestrial PgC is that the total carbon content of the system should be conserved. While there can be subdivisions within them [59], we are considering three carbon stores: atmosphere, land, and ocean. Since there is a conserved quantity, only the two governing equations are needed.

In an effort to simplify calculations, we will first translate  $T$  by  $\tilde{T}$ , giving the albedo function  $\alpha$  odd symmetry about the vertical axis. We introduce the variable

$$S = T - \tilde{T}$$

as well as the parameter

$$S_* = T_* - \tilde{T}.$$

In terms of the variables  $S, A, H$ , the system (4.1)-(4.3) becomes

$$(4.6) \quad \frac{dS}{dt} = \frac{1}{C_p} [Q(1 - \alpha(S)) - (B_0 + B_2\tilde{T} - B_1A + B_2S)]$$

$$(4.7) \quad \frac{dA}{dt} = B_3[P(S - S_*)^2 - B_4 - A] - (L + B_5A - B_6H)$$

$$(4.8) \quad \frac{dH}{dt} = L + B_5A - B_6H,$$

where

$$(4.9) \quad \alpha(S) = \frac{\alpha_M + \alpha_m}{2} - \frac{\alpha_M - \alpha_m}{2} \tanh\left(\frac{S}{D}\right).$$

Secondly, we observe that the RHS of (4.6) can be reasonably approximated by a cubic (see Figure 4.3). Thus we simplify the system (4.6)-(4.8) to

$$(4.10) \quad \frac{dS}{dt} = \frac{1}{C_p} \left[ B_1A - \frac{Q(\alpha_M - \alpha_m)}{6D^3} S^3 + \left( \frac{Q(\alpha_M - \alpha_m)}{2D} - B_2 \right) S + K \right]$$

$$(4.11) \quad \frac{dA}{dt} = B_3[P(S - S_*)^2 - B_4 - A] - (L + B_5A - B_6H)$$

$$(4.12) \quad \frac{dH}{dt} = L + B_5A - B_6H,$$

where

$$K = Q \left( 1 - \frac{\alpha_M + \alpha_m}{2} \right) - (B_0 + B_2\tilde{T}),$$

and the RHS of (4.10)-(4.12) are all polynomials.

Thirdly, based on the observation made in Figure 4.1, the model (4.10)-(4.12) should evolve on multiple time-scales. Such a separation of time-scales can only be identified in a dimensionless model. Therefore, we define the dimensionless quantities

$$x = \frac{S}{S_0}, \quad y = \frac{A}{A_0}, \quad z = \frac{H}{H_0}, \quad \text{and} \quad s = \frac{t}{t_0}$$



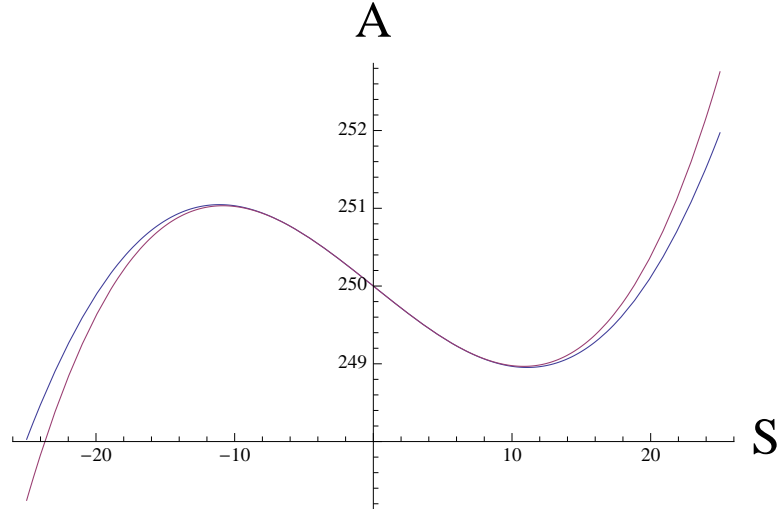


FIGURE 4.3. Cubic approximation of (4.10). Blue: the  $S$  nullcline in the  $SA$ -plane where  $\alpha(S)$  is a tanh function. Red: cubic approximation of the  $S$  nullcline.

where

$$\begin{aligned}
 S_0 &= \left( \frac{D^3(Q(\alpha_M - \alpha_m) - 4DB_2)}{Q(\alpha_M - \alpha_m)B_1} \right)^{\frac{1}{2}} \\
 A_0 &= \left( \frac{D^3(Q(\alpha_M - \alpha_m) - 4DB_2)^3}{Q(\alpha_M - \alpha_m)B_1^3} \right)^{\frac{1}{2}} \\
 H_0 &= \frac{B_5}{B_6} \left( \frac{D^3(Q(\alpha_M - \alpha_m) - 4DB_2)^3}{Q(\alpha_M - \alpha_m)B_1^3} \right)^{\frac{1}{2}} \quad \text{and} \\
 t_0 &= \frac{1}{B_5}.
 \end{aligned}$$

Then equations (4.10)-(4.12) become

$$(4.13) \quad \epsilon \dot{x} = y - x^3 + 3x - k$$

$$(4.14) \quad \dot{y} = p(x - a)^2 - b - my - (\lambda + y) + z$$

$$(4.15) \quad \dot{z} = r(\lambda + y - z),$$

where the dot (  $\dot{\phantom{x}}$  ) denotes  $\frac{d}{ds}$ . The new dimensionless parameters relate to the physical parameters of equations (4.10)-(4.12) in the following way:

$$k = \frac{K}{B_1 A_0}, \quad p = \frac{B_3 P S_0^2}{B_5 A_0}, \quad a = \frac{S_*}{S_0}, \quad b = \frac{B_3 B_4}{B_5 A_0}$$

$$m = \frac{B_3}{B_5}, \quad \lambda = \frac{L}{B_5 A_0}, \quad r = \frac{B_6}{B_5}, \quad \text{and} \quad \epsilon = \frac{B_5 C_p S_0}{B_1 A_0}.$$

Any time-scale separation is determined by  $\epsilon_1 = \epsilon$  and  $\epsilon_2 = \epsilon r$ . As mentioned earlier, parameter values in paleoclimate problems are the subject of some debate. In accordance with our observation based on Figure 4.1, we assume that temperature evolves on a faster time-scale than carbon, implying  $0 < \epsilon \ll 1$ . This assumption is further supported by [6]. If  $r = \mathcal{O}(1)$  we have 1 fast and 2 slow variables, and if  $r \ll 1$  we are in the three time-scale case. Depending on which parameters hold the key to having  $0 < \epsilon \ll 1$ , other parameters (e.g.  $p$ ,  $b$ , or  $\lambda$ ) may be small as well. Again, our approach is to assume as little as possible about the parameters, so we will keep this in mind as we perform the analysis.

REMARK 4. *The dimensionless form of the model is a variant of the Koper model, an electrochemical model that is known to exhibit MMOs [31, 36]. Many other models in chemistry and neuroscience also demonstrate MMOs (e.g. the Hodgkin-Huxley equations [49]). Indeed, many mechanisms in other areas such as mass balance in chemical reactions or gated ion channels in neural models behave similarly to certain climate mechanisms such as conservation of mass or exchange of carbon dioxide across the ocean-atmosphere surface.*

### 4.3. Analyzing the System

In this section we will analyze the system (4.13)-(4.15). We assume that the system is singularly perturbed with singular perturbation parameter  $\epsilon$ . We also assume that  $r = \mathcal{O}(\epsilon^n)$  where  $n = 0$  or  $n = 1$  (although fractional powers may be acceptable as well). Hence we are using a 2 slow/1 fast approach that allows for the case where  $r = \mathcal{O}(\epsilon)$ . We will comment on the case where  $r$  is small when appropriate. The

method of analyzing singularly perturbed systems—*geometric singular perturbation theory* (GSP)—was first developed by Fenichel. We will introduce the important concepts from GSP as required by the analysis. For further details on the theory, we direct the reader to the survey by Jones [30].

The following quantities will appear often in our calculations, so we define

$$h(x) = x^3 - 3x + k,$$

$$f(x) = p(x - a)^2 - b,$$

as well as

$$F(x, y) = y - h(x).$$

**4.3.1. The Layer Problem.** To begin the analysis, we rescale the time variable  $s$  by  $\epsilon^{-1}$  to obtain the system

$$(4.16) \quad x' = y - x^3 + 3x - k$$

$$(4.17) \quad y' = \epsilon(p(x - a)^2 - b - my - (\lambda + y) + z)$$

$$(4.18) \quad z' = \epsilon r(\lambda + y - z),$$

where the prime ( $'$ ) denotes  $d/d\tau$  and  $\tau = \epsilon^{-1}s$ . As long as  $\epsilon > 0$ , the new system (4.16)-(4.18) is equivalent to (4.13)-(4.15) in the sense that the paths of trajectories are unchanged—they are merely traced with different speeds. However, in the singular limit (i.e. as  $\epsilon \rightarrow 0$ ) the systems are different.

When  $\epsilon = 0$ , the system (4.16)-(4.18) becomes

$$x' = F(x, y)$$

$$y' = 0$$

$$z' = 0,$$

which is called the *layer problem*. Notice that the dynamics in the  $y$  and  $z$  directions are trivial. The *critical manifold*,

$$M_0 = \{F(x, y) = 0\} = \{y = h(x)\},$$

is the set of critical points of the layer problem.  $M_0$  is attracting (resp. repelling) whenever  $F_x < 0$  (resp.  $F_x > 0$ ), which corresponds to the  $x$ -values where the cubic  $h(x)$  is increasing (resp. decreasing). A simple calculation shows  $h'(x) = 0$  when  $x = \pm 1$ , so  $M_0$  is attracting on the outer branches where  $|x| > 1$ , repelling on the middle branch where  $|x| < 1$  and folded at  $x = \pm 1$ . To make this more explicit,  $M_0$  is ‘S’-shaped with two attracting branches

$$M_A^\pm = \{\pm x > 1\}$$

and a repelling branch

$$M_R = \{-1 < x < 1\}.$$

The attracting and repelling branches are separated by the folds

$$L^\pm = \{x = \pm 1\}.$$

At the folds  $L^\pm$ , the critical manifold is degenerate and the basic GSP theory for normally hyperbolic critical manifolds breaks down. As is so often the case, the scientifically and mathematically interesting behavior arises where the standard theory does not apply. In our case, the folds allow for more complicated dynamics such as relaxation oscillations or MMOs.

**4.3.2. The Reduced Problem.** The layer problem, which describes the fast dynamics off the critical manifold, was obtained by considering the  $\epsilon = 0$  limit of equations (4.16)-(4.18). The dynamics on the critical manifold, or slow dynamics, are obtained by looking at the system (4.13)-(4.15) as  $\epsilon \rightarrow 0$ . In the singular limit, the

system becomes

$$(4.19) \quad 0 = y - x^3 + 3x - k$$

$$(4.20) \quad \dot{y} = p(x - a)^2 - b - my - (\lambda + y) + z$$

$$(4.21) \quad \dot{z} = r(\lambda + y - z).$$

The first equation (4.19) provides an algebraic condition for a manifold on which this new system is defined. The critical manifold  $M_0$  is precisely the set that satisfies the algebraic condition, so equations (4.20)-(4.21) describe the dynamics on the manifold  $M_0$ . The two dimensional dynamical system (4.20)-(4.21) is called the *reduced problem*. Two equations are required to describe the dynamics on the 2D surface  $M_0$ , and with the algebraic condition we should be able to (locally) write the vector field of the reduced problem in terms of only the variables  $y$  and  $z$ . Since  $F_x = 0$  for some points on  $M_0$ , we cannot universally write  $x$  as a function of  $y$  and  $z$  on  $M_0$ —the function would have to be defined separately on each branch. However,  $F_y \equiv 1$ , so we can write  $y$  as a function of  $x$  (namely,  $y = h(x)$ ) on  $M_0$ . In order to exploit this functional dependence, we would like to formulate the reduced problem in terms of  $x$  and  $z$  instead of  $y$  and  $z$ . This is done by differentiating the algebraic condition in (4.19), and substituting it for the  $\dot{y}$  equation (4.20). Doing so produces

$$\begin{aligned} -F_x \dot{x} &= F_y \dot{y} + F_z \dot{z} \\ \dot{z} &= r(\lambda + y - z). \end{aligned}$$

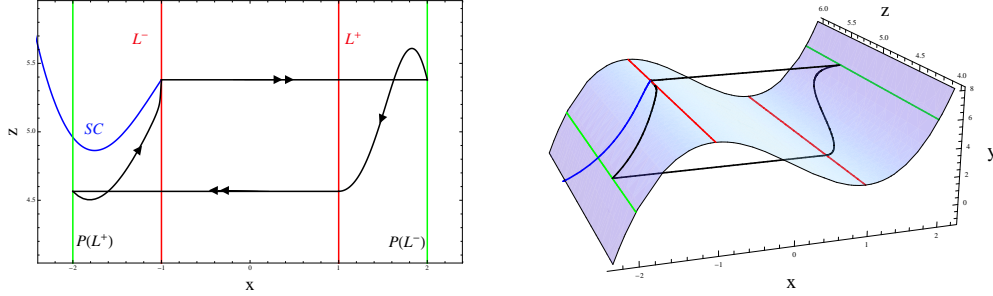
Substitution provides

$$(4.22) \quad \begin{aligned} h'(x) \dot{x} &= f(x) - (m + 1)h(x) - \lambda + z \\ \dot{z} &= r(\lambda + h(x) - z), \end{aligned}$$

and now the reduced problem is formulated as two equations in terms of two variables.

System (4.22) has three different types of singularities:

- ordinary singularities—these are equilibria of the full system (4.13)-(4.15)



(A) Projection of the singular orbit onto the critical manifold. Fold lines are denoted  $L^\pm$  and projections of the fold lines onto the opposite stable branches are denoted  $P(L^\pm)$ . The funnel lies below the strong canard  $\gamma_s$  (denoted SC).

(B) Singular orbit  $\Gamma$  in the full 3D phase space. Colored lines correspond to those in (a).

FIGURE 4.4. Example of a singular periodic orbit.  $\Gamma$  for  $a = 0.8$ ,  $p = 3$ ,  $b = 2.1$ ,  $k = 4$ ,  $r = 1$ ,  $m = 1$ , and  $\lambda = 1$ .

- regular fold points—also known as jump points, and
- folded equilibria—points along  $L^\pm$  that behave like equilibria (nodes, saddles, or foci) in the reduced problem, but are not equilibria of the full system (4.13)-(4.15).

Since  $h'(\pm 1) = 0$ , (4.22) describes a singular system. We can rescale the time variable  $s$  by  $h'(x)$  to obtain the desingularized system

$$(4.23) \quad \begin{aligned} \dot{x} &= f(x) - (m+1)h(x) - \lambda + z \\ \dot{z} &= rh'(x)(\lambda + h(x) - z). \end{aligned}$$

The rescaling reverses trajectories on  $M_R$  because this is precisely the set where  $h'(x) < 0$ , but the benefit of being able to define dynamics on the folds outweighs the cost. From system (4.23), it is now easy to classify the different singularities of the reduced problem. Ordinary singularities occur where  $z = h(x) + \lambda$  and  $f(x) = mh(x)$ . Folded singularities are equilibria of (4.23) where  $\dot{z} = 0$  as a result of the rescaling. That is, folded singularities occur where  $h'(x) = 0$ ,  $\lambda + h(x) - z \neq 0$ , and  $\dot{x} = 0$ . When  $h'(x) = 0$ , but  $\dot{x} \neq 0$ , we have regular fold points.

**4.3.3. Strategy.** Folded nodes (as well as folded saddle-nodes) can produce MMOs with a suitable global return mechanism. We establish a global return mechanism by constructing a singular periodic orbit  $\Gamma$ , consisting of heteroclinic orbits of the layer problem and a segment on each of those stable branches  $M_A^\pm$ . The heteroclinic orbits of the layer problem take trajectories from a fold  $L^\pm$  to its projection  $P(L^\pm)$  on the opposite stable branch. An example of a singular periodic orbit  $\Gamma$  is shown in Figure 4.4. Assuming there is a folded node on  $L^-$  (wlog), we can construct  $\Gamma$  by following the fast fiber from the node to the stable branch  $M_A^+$ . From there, the trajectory follows the slow flow on  $M_A^+$  as described by (4.23) until it reaches the fold  $L^+$ . If it reaches  $L^+$  at a jump point, we follow the fast fiber back to  $M_A^-$ . We want the landing point on  $M_A^-$  to be in the *singular funnel*—that is, the region bounded by the strong stable trajectory  $\gamma_s$  and the fold  $L^-$  that contains the weak stable trajectory  $\gamma_w$ . The trajectory  $\gamma_s$  is also called the strong canard (denoted ‘SC’ in Figure 4.4a), and it forms the boundary of the funnel. The region is called a funnel because all trajectories in the region get funneled through the folded node. Therefore, any singular orbit from the folded node which returns to the funnel will necessarily be a singular periodic orbit.

A node (in a 2D system) has two real eigenvalues of the same sign, a weak eigenvalue  $\mu_w$  and a strong eigenvalue  $\mu_s$  such that  $|\mu_w| < |\mu_s|$ . The ratio of these eigenvalues

$$\mu = \frac{\mu_w}{\mu_s} < 1,$$

is important in determining the number of small-amplitude oscillations in the MMO signature. This is made explicit in the following theorem due to Brøns *et al* [4] that provides conditions under which a system has a stable MMO orbit.

**THEOREM 4.3.1.** *Suppose that the following assumptions hold in a fast/slow system,*

(A1)  $0 < \epsilon \ll 1$  is sufficiently small with  $\epsilon^{1/2} \ll \mu$

(A2) the critical manifold is ‘S’-shaped, i.e.  $M_0 = M_A^- \cup L^- \cup M_R \cup L^+ \cup M_A^+$ ,

(A3) there is a (stable) folded node  $N$  on (wlog)  $L^-$ ,

(A4) there is a singular periodic orbit  $\Gamma$  such that  $\Gamma \cap M_A^-$  lies in the interior of the singular funnel to  $N$ , and

(A5)  $\Gamma$  crosses  $L_\pm$  transversally.

Then there exists a stable periodic orbit of MMO type  $1^s$ , where

$$(4.24) \quad s = \left\lfloor \frac{(1 + \mu)}{2\mu} \right\rfloor,$$

and the right-hand side of (4.24) denotes the the greatest integer less than  $(1 + \mu)/(2\mu)$ .

In [35], Krupa and Wechselberger show that the folded node theory still applies in the parameter regime where  $\mu = \mathcal{O}(\epsilon^{1/2})$  if the global return mechanism is still in tact (i.e  $\Gamma \cap M_A^-$  lies in the interior of the singular funnel). Note that in this parameter regime, the MMO signature can be more complicated. Figure 4.10 depicts a few of the more interesting MMO patterns generated by (4.13)-(4.15) when  $\mu = \mathcal{O}(\epsilon^{1/2})$ .

The remainder of this section will focus on finding conditions on the parameters of equations (4.13)-(4.15) so that the system satisfies (A1)-(A5). Since  $\mu$  is calculated in the singular limit, we can always choose  $\epsilon$  small enough to satisfy condition (A1). Also, we have already discussed the ‘S’-shape of the critical manifold, demonstrating that condition (A2) is satisfied. The next task will be find conditions so that equations (4.13)-(4.15) have a folded node singularity.

**4.3.4. Folded Node Conditions.** The data in Figure 4.1 show small amplitude oscillations occurring at low temperatures, so we seek parameters for which (4.22) has a stable folded node along the lower fold  $L^-$ .

LEMMA 4.3.2. *Define*

$$(4.25) \quad \delta = f(-1) - mh(-1) = p(a + 1)^2 - b - m(k + 2).$$

Assume the parameters of the system (4.13)-(4.15) satisfy

(a)  $p > 0$ ,



(b)  $a > -1$ ,

(c)  $\delta > 0$ , and

(d)  $p^2(a+1)^2 - 6r\delta > 0$ .

Then there is a folded node at  $(-1, z_-)$  where

$$z_- = 2 + k + \lambda - \delta.$$

PROOF. The linearization of (4.23) at any fixed point  $(x_0, z_0)$  is

$$(4.26) \quad J(x_0, z_0) = \begin{pmatrix} f'(x_0) - (m+1)h'(x_0) & 1 \\ r[(h'(x_0))^2 + h''(x_0)(\lambda + h(x_0) - z_0)] & -r h'(x_0) \end{pmatrix}.$$

There is a folded singularity at  $(-1, z_-)$  where

$$z_- = (m+1)h(-1) + \lambda - f(-1).$$

Since  $h'(-1) = 0$ , we have the linearization

$$(4.27) \quad J(-1, z_-) = \begin{pmatrix} f'(-1) & 1 \\ -6r[f(-1) - mh(-1)] & 0 \end{pmatrix}.$$

For  $(-1, z_-)$  to be a stable folded node,  $J(-1, z_-)$  must satisfy three conditions:

- (1)  $\text{Tr}(J(-1, z_-)) < 0$ ,
- (2)  $\det(J(-1, z_-)) > 0$ , and
- (3)  $[\text{Tr}(J(-1, z_-))]^2 - 4\det(J(-1, z_-)) > 0$ .

The requirement on the trace implies that  $f'(-1) < 0$ , or  $p(-1-a) < 0$ . Assuming  $p > 0$ , we arrive at condition (b)  $a > -1$ . The requirement on the determinant gives us  $6r[f(-1) - mh(-1)] > 0$ . Since  $r > 0$ , we will have  $\det(J(-1, z_-)) > 0$  whenever  $\delta = f(-1) - mh(-1) > 0$ . That is precisely condition (c). Conditions (a)-(c) are enough to guarantee that the folded equilibrium is stable, but they do not distinguish between stable a stable node or a stable focus. This is determined by the discriminant

condition, which is satisfied if

$$p^2(a+1)^2 - 6r[f(-1) - mh(-1)] = p^2(a+1)^2 - 6r\delta > 0.$$

□

Note that  $|\delta|$  is precisely the distance along the fold from the node to the intersection of the true  $z$  nullcline with the fold at  $x = -1$ . If  $\delta > 0$ , which is required by condition (b), then the node lies under the  $z$  nullcline on  $M_0$ . That is, if  $z_n$  is the intersection of the  $z$  nullcline with the fold (i.e.,  $z_n = h(-1) + \lambda$ ), then  $z_n > z_-$  with  $z_n = z_- + \delta$ . As we will see, the parameter  $r$  will not appear in the remaining calculations. Thus we strive to find conditions on  $\delta$ ,  $a$ , and  $p$ . Choosing values that satisfy those conditions, (c) then provides an upper bound on  $r$ .

**REMARK 5.** *In each of the limiting cases  $r \rightarrow 0$  and  $\delta \rightarrow 0$ , the Jacobian (4.27) will have a zero eigenvalue and the system will have a folded saddle-node of type II. Near the  $r = 0$  limit we are in the three time-scale case with a global three time-scale separation. Near the  $\delta = 0$  limit, we have a local three time-scale split at the folded singularity. In either case, the ratio of eigenvalues  $\mu$  will be small, so near the saddle-node limit, we use the theory for  $\mu = \mathcal{O}(\epsilon^{1/2})$ .*

Having found conditions for a folded node, it remains to be shown that these conditions are consistent with a return mechanism satisfying (A4) and (A5) from Theorem 4.3.1. As indicated by (A4), the singular funnel is a vital component of the global return mechanism. Typically, the functionality of the return mechanism is demonstrated numerically [36, 48]. We are able to find sufficient conditions analytically by linearly approximating the boundary of the funnel, however there are drawbacks to this approach. We will explore these consequences further in the discussion.

**4.3.5. Estimate of the Funnel.** Assuming the node conditions (a)-(d) from Lemma 4.3.2 are met, the folded singularity will have a strong stable eigenvalue (eigenvector) and a weak stable eigenvalue (eigenvector). Let  $\mu_{s,w}$  be the eigenvalues, where  $s$  and

$w$  denote strong and weak, respectively. Then

$$\mu_s < \mu_w < 0.$$

Also let  $(x_{s,w}, z_{s,w})$  denote the corresponding eigenvector. A simple computation shows the slope of the eigenvector

$$m_i = \frac{z_i}{x_i} = \frac{-6r\delta}{\mu_i} > 0,$$

where  $i$  can be either  $s$  or  $w$ . Then we have the following relationships

$$0 < m_s < m_w < -f'(-1),$$

where  $-f'(-1)$  is the slope of the  $x$  nullcline at the node. Recall that the singular funnel is the region bounded by the fold  $L^-$  and the strong canard  $\gamma_s$  (the trajectory that approaches the node with slope  $m_s$ ) that contains the weak canard. In our case, locally near the folded node, the funnel will lie below the strong canard. Following  $\gamma_s$  away from the node in reverse time, we see that if  $\gamma_s$  intersects the  $x$  nullcline, it will turn down and to the right until it intersects the fold  $L^-$ . We want to avoid this situation since it effectively precludes a global return mechanism. However, if  $\gamma_s$  intersects the  $z$ -nullcline, then it will continue up and to the left in reverse time as in Figure 4.5. The following lemma provides conditions under which  $\gamma_s$  lies entirely above its tangent line at the node, allowing us use a linear approximation to find a lower bound for the intersection of  $\gamma_s$  with  $P(L^+)$ .

LEMMA 4.3.3. *Let equations (4.13)-(4.15) satisfy the conditions (a)-(d) of Lemma 4.3.2. Furthermore assume*

- (e)  $\frac{2p^2(a+1)^2}{\delta} + 2pa - 6(m+1) < 0$ , and
- (f)  $p(a+1) > 2$ .

*Let  $m_s$  denote the slope of the strong eigenvector to the node. That is*

$$m_s = \frac{6r\delta}{-\mu_s} = \frac{6r\delta}{|\mu_s|}.$$

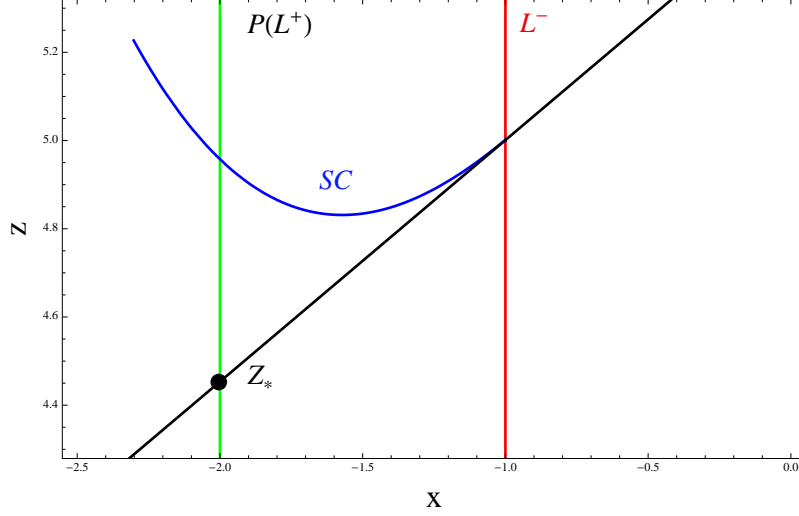


FIGURE 4.5. A lower bound for the edge of the funnel.

Then the strong canard  $\gamma_s$  is tangent to the line  $z = m_s(x + 1) + z_-$  at  $x = -1$ , and lies above the line for  $x < -1$ .

The method of proof is to show that  $\gamma_s$ , thought of as  $z = \gamma_s(x)$ , is concave up at the node  $(-1, z_-)$ . This shows that  $\gamma_s$  lies above the line

$$z - m_s(x + 1) = z_-$$

near the folded node. We will then consider the direction of the vector field along the line to show that  $\gamma_s$  remains above the line.

PROOF. The  $z$  coordinate of the strong canard tends to  $z_-$  as  $x \rightarrow -1$ , however since the point  $(-1, z_-)$  is a node, there are many trajectories that do so. The strong canard can be characterized as the trajectory whose slope tends to  $m_s$  as  $x \rightarrow -1$ . That is

$$\lim_{x \rightarrow -1} \frac{dz}{dx} = \frac{6r\delta}{|\mu_s|}.$$

The concavity of the strong canard determines whether it approaches its tangent line from above or below. We begin with the first derivative,

$$\frac{dz}{dx} = \frac{rh'(x)(\lambda + h(x) - z)}{f(x) - (m + 1)h(x) - \lambda + z}.$$

To assist us in the calculations, we define

$$\eta(x) = f(x) - (m+1)h(x) - \lambda + z$$

$$\phi(x) = \lambda + h(x) - z$$

noting that

$$\phi(-1) = \delta, \quad \phi'(-1) = \frac{-6r\delta}{|\mu_s|}, \quad \eta(-1) = 0,$$

$$h'(-1) = 0, \quad h''(-1) = -6, \quad h'''(x) = 6$$

and

$$\lim_{x \rightarrow -1} \frac{h'(x)}{\eta(x)} = \frac{6}{|\mu_s|}.$$

Now, we use the quotient rule to obtain:

$$\frac{d^2 z}{dx^2} = \frac{r}{(\eta(x))^2} \left[ \eta(x) \left( h'(x) \left( h'(x) - \frac{dz}{dx} \right) + \phi(x) h''(x) \right) - h'(x) \phi(x) \eta'(x) \right].$$

In particular, we are interested in

$$\mathcal{L} = \lim_{x \rightarrow -1} \frac{d^2 z}{dx^2}.$$

Using L'Hopital's rule, we see

$$\begin{aligned} \mathcal{L} = & \lim_{x \rightarrow -1} \left[ \frac{r}{2\eta(x)\eta'(x)} \right. \\ & \cdot \left[ \eta(x) \left( h'(x) \left( h''(x) - \frac{d^2 z}{dx^2} \right) + h''(x) \left( h'(x) - \frac{dz}{dx} \right) + \phi(x) h'''(x) + h''(x) \phi(x) \right) \right. \\ & + \eta'(x) \left( h'(x) \left( h'(x) - \frac{dz}{dx} \right) + \phi(x) h''(x) \right) - \eta'(x) \phi(x) h''(x) \\ & \left. \left. - h'(x) \left( \phi(x) \left( f''(x) - (m+1)h''(x) + \frac{dz}{dx} \right) + \phi'(x) \eta'(x) \right) \right] \right], \end{aligned}$$

which simplifies to

$$\mathcal{L} = \frac{3r}{\eta'(-1)} \left( \frac{12r\delta}{|\mu_s|} + \delta \right) - \frac{3r}{|\mu_s|} \left( \frac{6r\delta}{|\mu_s|} \right) - \frac{3r}{|\mu_s|} \left( \frac{\delta(2p + 6(m+1) + \mathcal{L})}{\eta'(-1)} - \frac{6r\delta}{|\mu_s|} \right).$$

Simplifying further and gathering the  $\mathcal{L}$  terms on one side gives

$$(4.28) \quad \frac{\eta'(-1)|\mu_s| + 3r\delta}{3r\delta} \mathcal{L} = 12r + |\mu_s| - 2p - 6(m+1).$$

Using the node conditions—specifically the bound on  $r$  from condition (d)—we can show the coefficient of  $\mathcal{L}$  is negative since

$$\begin{aligned} \eta'(-1)|\mu_s| + 3r\delta &= \left( -2p(a+1) + \frac{6r\delta}{|\mu_s|} \right) \mu_s + 3r\delta \\ &= 9r\delta - 2p(a+1)|\mu_s| \\ &< \frac{3}{2}p^2(a+1)^2 - 2p^2(a+1)^2 - 2p(a+1)\sqrt{p^2(a+1)^2 - 6r\delta} \\ &< 0. \end{aligned}$$

Since we are looking for a lower bound on the edge of the singular funnel, we want the strong canard to lie above its tangent line at the node. So, we want  $\mathcal{L} > 0$ , which happens when the right-hand side of (4.28) is negative. That is, we want

$$(4.29) \quad 12r + |\mu_s| - 2p - 6(m+1) < 0.$$

Using the bound for  $r$  again as well as the estimate  $|\mu_s| < 2p(a+1)$ , we see that (4.29) will be true if

$$(4.30) \quad \frac{2p^2(a+1)^2}{\delta} + 2pa - 6(m+1) < 0.$$

Therefore condition (e) implies that  $\gamma_s$  lies above the line  $z - m_s(x+1) = z_-$  near the node.

Next, we want to show that it remains above the line moving away from  $L^-$  in reverse time. To do so we consider the vector field on lines of the form

$$C = z - m_s x.$$

In particular, we look for conditions such that

$$(4.31) \quad \dot{C}|_{C=z_-} \leq 0.$$

When this happens,  $\gamma_s$  must be repelled away above the line in reverse time. Obviously,  $\dot{C} = 0$  at the node  $(-1, z_-)$ . When

$$p(a+1) > 2,$$

then  $\dot{C}|_{C=z_-}$  is increasing as a function of  $x$  and the condition in (4.31) is satisfied. Thus conditions (e) and (f) together ensure that  $\gamma_s$  lies above the line  $z - m_s(x+1) = z_-$  on  $M_A^-$ .  $\square$

We define  $z_*$  to be the intersection of the line  $x = -2$  (i.e.  $P(L^+)$ ) with the linear approximation of the funnel,  $z - m_s(x+1) = z_-$  as shown in Figure 4.5. Lemma 4.3.3 ensures that  $z_*$  lies in the interior of the funnel. As we construct the singular periodic orbit,  $z_*$  provides a target for trajectories returning from  $M_A^+$ .

**4.3.6. Singular Periodic Orbit.** We now seek conditions so that a singular orbit leaves the folded node, lands on  $M_A^+$  along  $P(L^-)$ , follows a trajectory of the reduced problem towards  $L^+$ , crosses  $L^+$  transversely, and returns to  $M_A^-$  on  $P(L^+)$  below  $z_*$ . Singularities on  $L^+$  and  $M_A^+$  will play a major role in determining conditions that guarantee the existence of the singular periodic orbit.

We will define  $z_+$  to be the  $z$  coordinate of the folded singularity on  $L^+$ , so

$$\begin{aligned} z_+ &= (m+1)h(1) + \lambda - f(1) \\ &= (m+1)(k-2) + \lambda - p(1-a)^2 + b. \end{aligned}$$

If  $z_+$  lies above the intersection of the  $z$  nullcline with the fold  $L^+$ , then there will be a region where trajectories cross  $L^+$  transversely as depicted in Figure 4.6.

**LEMMA 4.3.4.** *Let equations (4.13)-(4.15) satisfy the conditions of Lemmas 4.3.2 and 4.3.3. Furthermore, assume  $\delta < 4$  and*

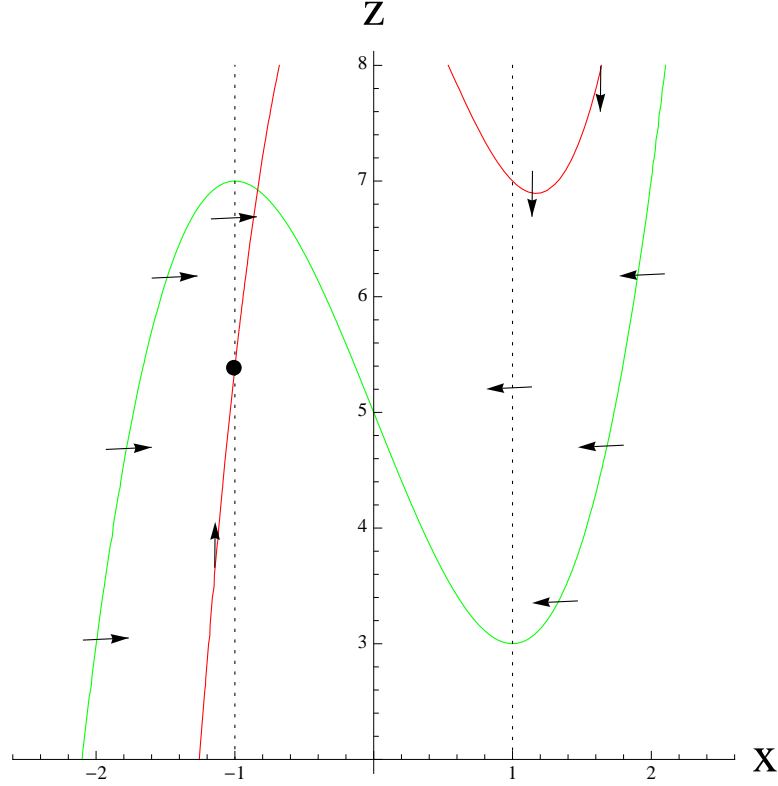


FIGURE 4.6. Locally invariant regions on the critical manifold. Dotted black lines denote folds. The green cubic is the true  $z$  nullcline. The red curve is the  $x$  nullcline. The regions between the nullclines are locally invariant. That is, the only way to leave these regions is to hit the fold.

$$(g) \quad 4(ap - m) - \delta > 0$$

$$(h) \quad \Delta_\delta(a, p, m) < 0,$$

where

$$(4.32)$$

$$(4.33) \quad \begin{aligned} \Delta_\delta(a, p, m) = & p^2(-3m + 2ap)^2 - 4m(-3m + 2ap)^3 \\ & + 4p^3(-\delta - 2m + p + 2ap) - 18mp(-3m + 2ap)(-\delta - 2m + p + 2ap) \\ & - 27m^2(-\delta - 2m + p + 2ap)^2. \end{aligned}$$

Then the singular orbit from the folded node will land on  $P(L^-) \subset M_A^-$ , follow a trajectory of the reduced problem (4.23), and cross the fold  $L_+$  transversely.



REMARK 6. *The condition that  $\delta < 4$  will be replaced with a stricter condition in Lemma 4.3.5 to ensure that the singular orbit returns to the funnel.*

PROOF. The intersection of the  $z$  nullcline with  $L^+$  occurs at  $z = h(1) + \lambda$ . Therefore, there is a positively invariant region where trajectories can only leave  $M_A^+$  by crossing  $L^+$  transversally if

$$z_+ = (m+1)h(1) + \lambda - f(1) > h(1) + \lambda,$$

which happens if and only if

$$\begin{aligned} 0 &< mh(1) - f(1) \\ \Leftrightarrow 0 &< m(k-2) - p(1-a)^2 + b \\ \Leftrightarrow 0 &< 4(ap-m) - \delta. \end{aligned}$$

Thus condition (g) gives us that the nullclines are aligned as in Figure 4.6 along  $L^+$ , and the positively invariant region exists. Next, we show that the singular orbit from the node enters this positively invariant region.

The assumption that  $\delta < 4$  ensures that  $z_- > h(1) + \lambda$ . This is because the fast fiber from the folded node on  $L^-$  lands on  $P(L^-) \subset M_A^+$  exactly the distance  $\delta$  below the  $z$  nullcline. Here, the vector field of (4.23) points up and to the left. If the  $x$  nullcline lies above the  $z$  nullcline, then the trajectory will continue up and to the left until it enters the positively invariant region shown in Figure 4.6. Condition (g) implies that the  $x$  nullcline lies above the  $z$  nullcline at the fold. Thus, the only way for the nullclines to switch their orientation is for them to intersect, creating a true equilibrium of (4.23). The nullclines intersect wherever the curves  $z = h(x) + \lambda$  and  $z = (m+1)h(x) + \lambda - f(x)$  intersect. That is, intersections occur whenever

$$mh(x) - f(x) = 0.$$

Note that  $mh(x) - f(x)$  is a cubic. Therefore, the number of zeroes of  $mh(x) - f(x)$  is determined by the cubic discriminant, which is precisely the quantity  $\Delta_\delta$ .

If  $\Delta_\delta < 0$  there is only one intersection, but if  $\Delta_\delta > 0$  there are three. Condition (c) implies the  $x$  nullcline lies below the  $z$  nullcline on  $L^-$  (i.e. where  $x = -1$ ), and condition (g) implies the  $x$  nullcline lies above the  $z$  nullcline on  $L^+$  (i.e. where  $x = +1$ ). By the Intermediate Value Theorem, the nullclines will intersect for some  $x$  such that  $-1 < x < 1$ . Therefore, the conditions (g) and (h) prevent there from being an intersection on either stable branch of  $M_0$ . This implies a singular trajectory through the folded node will cross  $L^+$  transversely.  $\square$

REMARK 7. *In fact, the condition  $\delta > 0$  precludes true equilibria on  $M_A^-$ . This can be seen by comparing the slopes of the  $x$  and  $z$  nullclines on  $M_A^-$ . The  $x$  nullcline is the curve  $z = (m+1)h(x) - \lambda - f(x)$ , so it has slope*

$$\begin{aligned} \frac{dz}{dx} &= (m+1)h'(x) - f'(x) \\ &= (m+1)h'(x) - 2p(x-a) \\ &> (m+1)h'(x), \end{aligned}$$

*since  $x \leq -1$  on  $M_A^-$ . Meanwhile, the  $z$  nullcline is given by the equation  $z = h(x) + \lambda$  which has slope*

$$\frac{dz}{dx} = h'(x).$$

*Since an equilibrium is precisely the intersection of these curves, any equilibrium on  $M_A^-$  will result in the  $x$  nullcline crossing the fold above the  $z$  nullcline, implying  $\delta < 0$ .*

Lemma 4.3.4 allows for the possibility that the folded singularity  $(1, z_+)$  is also a folded node. If we consider the Jacobian at the point  $(1, z_+)$ , we see that condition (g) implies  $\det(J(1, z_+)) > 0$ . Therefore, the stability of the folded singularity depends on  $f'(1)$ . To exclude the possibility of SAOs along  $L^+$ , we want to avoid the case where  $(1, z_+)$  is a stable folded node. If  $f'(1) > 0$ , then the folded singularity will be

unstable. Requiring  $f'(-1) < 0 < f'(1)$  implies that  $p > 0$  and  $-1 < a < 1$ . We update condition (b) from Lemma 4.3.2 accordingly, so we now have

$$(b) \quad -1 < a < 1.$$

Finally, we need to find conditions so that the singular trajectory from the folded node returns to the funnel. This will show that we in fact have a singular periodic orbit.

LEMMA 4.3.5. *Let equations (4.13)-(4.15) satisfy the conditions (a)-(h) from Lemmas 4.3.2-4.3.4. Additionally, suppose the equations satisfy*

$$(i) \quad 4(m+4) - 5ap - p > 0.$$

*Then there is a singular periodic orbit  $\Gamma$ .*

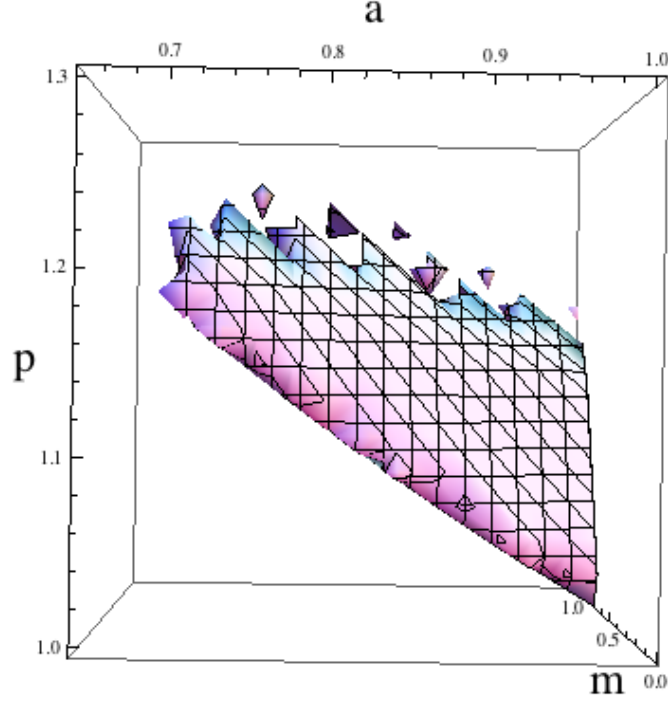
PROOF. By Lemma 4.3.2, we know the system will have a folded node singularity. Let  $\Gamma$  be the singular trajectory consisting of the fast fiber of the layer problem from the singular node to  $P(L^-)$ . By Lemma 4.3.4 we know that the trajectory will follow the slow flow on  $M_A^+$  until it intersects  $L_+$  transversely. Furthermore, we know that  $z_+$  is an upper bound on the  $z$  coordinate of the intersection. If  $z_+ < z_*$ , then  $\Gamma$  will land in the singular funnel upon leaving  $L^+$ . Direct calculation shows that  $z_+ < z_*$  precisely when  $4(m+4) - 5ap - p > 0$ .  $\square$

#### 4.3.7. Main Result.

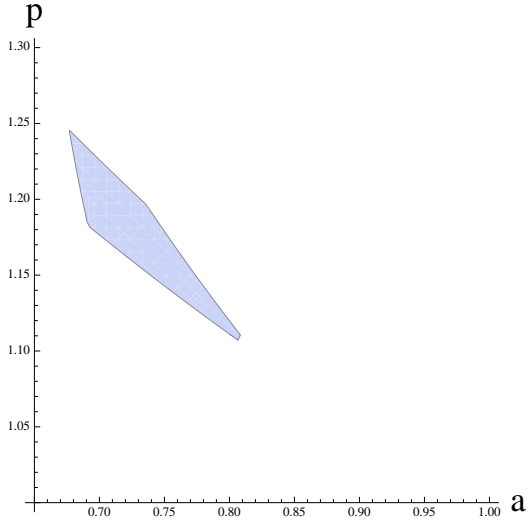
THEOREM 4.3.6. *Suppose the parameters of the system (4.13)-(4.15) satisfy the conditions (a)-(i). Then, for  $\epsilon$  sufficiently small, the system will have a stable periodic orbit of MMO-type  $1^s$  for some  $s > 0$ .*

PROOF. Lemmas 4.3.2-4.3.5 show that these conditions satisfy the assumptions of Theorem 4.3.1.  $\square$

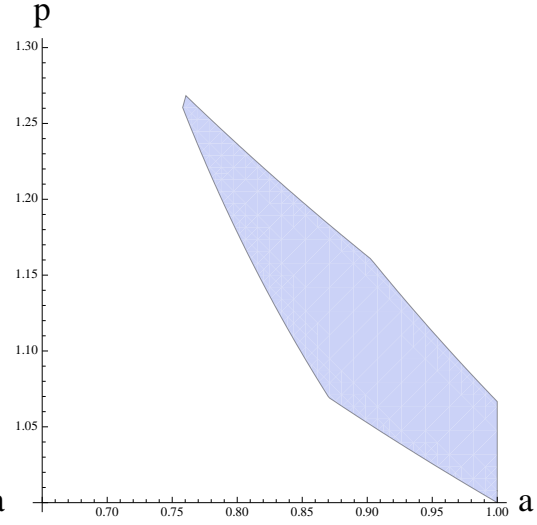
Figure 4.7 depicts a portion of phase space that satisfies conditions (a)-(i) in Theorem 4.3.6. These conditions place restrictions on  $a$ ,  $p$ ,  $m$ , and  $r$  explicitly, as



(A) Solid in  $apm$ -space.



(B) Slice for  $m = 0.4$ .



(C) Slice for  $m = 0.6$ .

FIGURE 4.7. Parameters that will produce an MMO orbit. Parameters in  $apm$ -space for  $\delta = 1.3$  that satisfy conditions (a)-(i) from Theorem 4.3.6.

well as  $b$  and  $k$  through the restrictions on  $\delta$ . However, there are no restrictions on  $\lambda$ . Additionally, Figure 4.8 shows the time series for  $x$  for a trajectory satisfying the conditions of Theorem 4.3.6.

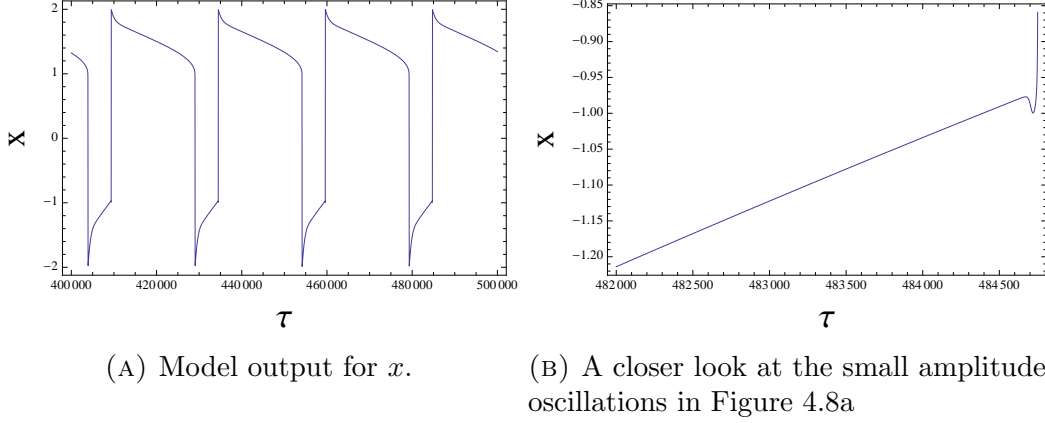
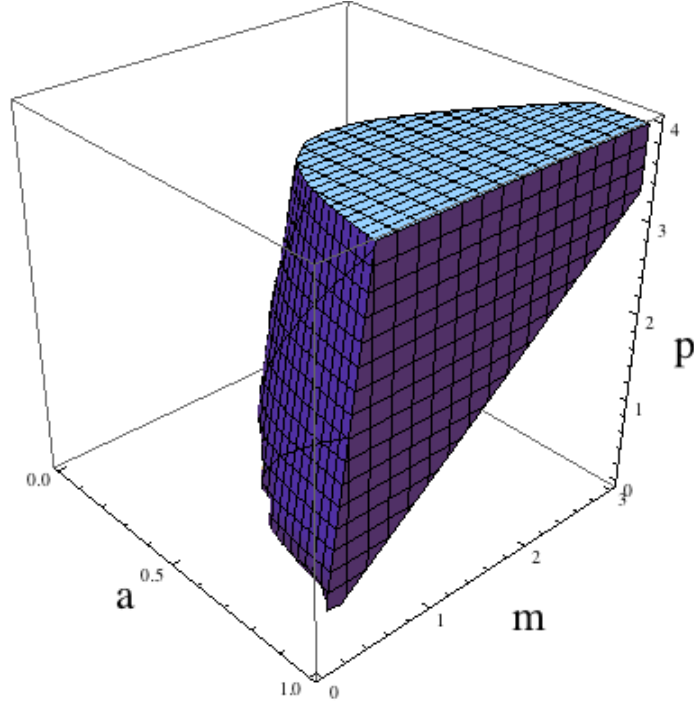


FIGURE 4.8. MMO orbit.  $\epsilon = 0.001$ ,  $a = 0.91$ ,  $p = 1.05$ ,  $b = 0.31$ ,  $k = 2.2$ ,  $r = 0.3$ ,  $\lambda = 1$ , and  $m = 0.6$ . With these parameters  $\delta = 1$ .

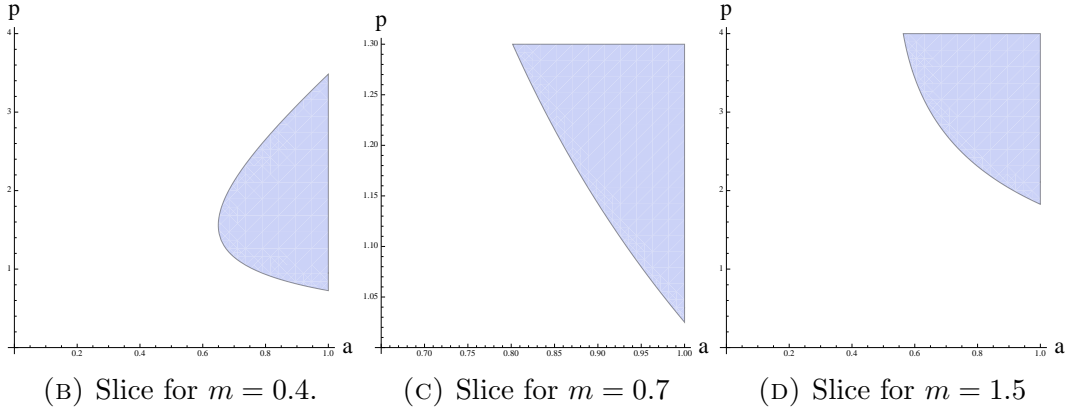
#### 4.4. Discussion

We have found sufficient conditions such that the system (4.13)-(4.15) has a stable periodic orbit with MMO signature  $1^s$ . To our knowledge, this is the first climate-based model that has been analyzed to demonstrate MMOs. The dimensionless model is a variant of the Koper model with an added nonlinearity. As with the standard Koper model, the model has an ‘S’-shaped critical manifold and a parameter regime with both a folded node and global return mechanism. Although the additional nonlinearity in the model does not factor into obtaining a folded node, nonlinear effects play a significant role in determining the shape of the funnel, and consequently the return mechanism. From a mathematical standpoint, it is significant that the additional nonlinearity does not destroy the functionality of the model to produce an MMO pattern.

While the conditions (a)-(i) in Theorem 4.3.6 are sufficient, they are not all necessary conditions for the model to exhibit MMOs. In fact, they are rather strict. This is a direct consequence of linearly approximating the funnel to obtain conditions analytically. Figure 4.9 depicts the portion of phase space satisfying only the conditions of Theorem 4.3.6 that do not relate to the linear approximation of the funnel. While it is not expected that all of these parameter choices will produce a stable MMO orbit, there are still parameter regimes outside of this range that are able to do so.



(A) Solid in  $apm$ -space.



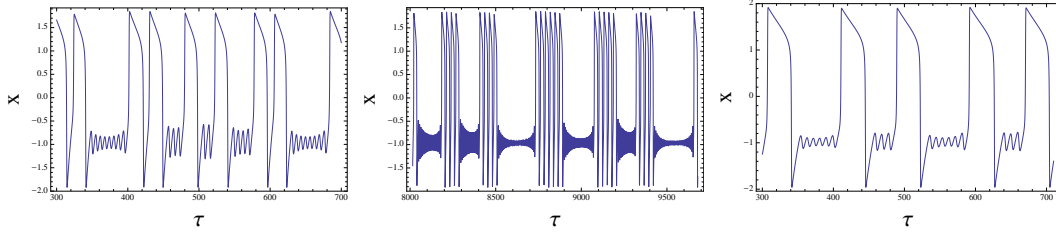
(B) Slice for  $m = 0.4$ .

(C) Slice for  $m = 0.7$

(D) Slice for  $m = 1.5$

FIGURE 4.9. More parameters that could produce MMOs. Parameters in  $apm$ -space for  $\delta = 1.3$  that satisfy conditions (a)-(d), (g), and (h) from Theorem 4.3.6.

Notably, there should be MMO orbits with  $a > 1$  (which does not satisfy condition (b)) as well as MMO orbits in a parameter regime that has equilibria on  $M_A^+$  (which violates condition (h)) as long as the equilibria occur for  $x > 2$ . The stable periodic orbits (of some MMO type) outside of the parameter regime described by Theorem 4.3.6 can be much more complicated as a result of the return mechanism projecting the singular periodic orbit closer to the boundary of the funnel (i.e., closer to the strong canard  $\gamma_s$ ). The behavior in this regime is also described by Brøns *et al* in [4].

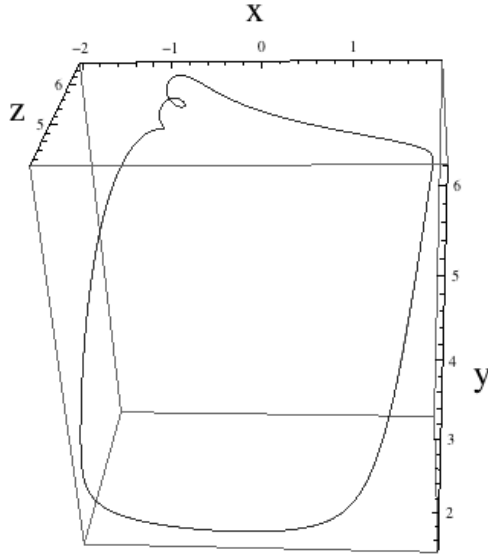


(A) Example of 3 time-scale series  $\epsilon = 0.1$ ,  $a = 0.8$ ,  $p = 3$ ,  $b = 2$ ,  $k = 4$ ,  $r = 0.05$ ,  $m = 1$ , and  $\lambda = 1$ . (B) Example of 3 time-scale series  $\epsilon = 0.1$ ,  $a = 0.8$ ,  $p = 3$ ,  $b = 2.3$ ,  $k = 4$ ,  $r = 0.01$ ,  $m = 1$ , and  $\lambda = 1$ . (C) Example of 3 time-scale series  $\epsilon = 0.05$ ,  $a = 0.8$ ,  $p = 3$ ,  $b = 2.32$ ,  $k = 4$ ,  $r = 0.1$ ,  $m = 1$ , and  $\lambda = 1$ .

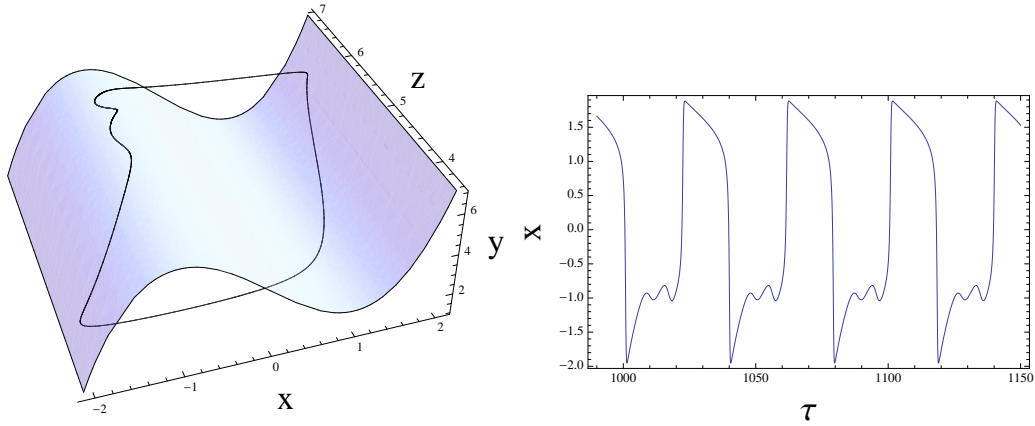
FIGURE 4.10. Examples of MMO patterns in the three time-scale case.

The trajectories shown in Figures 4.10-4.11 do not come from sets of parameters that satisfy the conditions in Theorem 4.3.6. We chose to include the trajectory from Figure 4.11 because the time series it generates is closer to the pattern found in Figure 4.1 than, for example, the one in Figure 4.8. In some sense, this is because there are two different questions being considered: (1) “can the model described by (4.13)-(4.15) produce mixed mode oscillations?” and (2) “can the model produce a qualitatively similar pattern to the temperature record depicted in Figure 4.1?” The analysis in Section 3 proves that the model can exhibit mixed mode oscillations, although it removes a portion of phase space relevant to the second question. Still, it provided us with insight as to where to look. Specifically, the folded node conditions (a)-(d) are necessary (in a system with only one fast variable).

The time series in Figures 4.1 and 4.11c are qualitatively similar in that they both contain large oscillations followed by a series of smaller amplitude oscillations. The model can give us some insight about the climate system. The physical implication of the requirement that  $-1 < a < 1$  is that  $\text{CO}_2$  drawdown due to terrestrial mechanisms is most efficient at a temperature somewhere between the stable glacial and interglacial states. Through the requirements on  $\delta$  we learn about the relationship between  $b$ ,  $m$ , and  $k$ . This relates the amount of  $\text{CO}_2$  removed from the atmosphere when the planet is most efficient at doing so ( $b$ ), the ratio of the timescales of the land-atmosphere carbon flux to that of the ocean-atmosphere exchange ( $m$ ), and the



(A) Attracting periodic orbit in the 3D phase space.



(B) The attracting periodic orbit shown with the critical manifold. (C) Model output for  $x$  for the trajectory in Figure 4.11a.

FIGURE 4.11. Another MMO orbit.  $\epsilon = 0.1$ ,  $a = 0.8$ ,  $p = 3$ ,  $b = 2.1$ ,  $k = 4$ ,  $r = 1$ ,  $m = 1$ , and  $\lambda = 1$ .

minimum/maximum values of atmospheric carbon ( $k$ ). Finally,  $r$  tells us something about the proportion of carbon in the atmosphere to carbon in the ocean required for the ocean to switch from absorbing to outgassing. If  $r$  is large, we will no longer have a folded node. It may be the case that  $r \ll 1$ , which puts us near the folded saddle-node limit and allows for more complicated behavior. Some simulations with  $r \ll 1$  are shown in Figure 4.10.



The analysis required to show MMOs due to a folded node assumes a separation of time scales and (at least) two slow variables. As mentioned in the introduction and Section 2, it is often difficult to determine exactly which parameters are small enough to perform this analysis. Here we rely on the wisdom of climate scientists. It may be that changes in atmospheric greenhouse gases happen on a similar timescale to temperature. Figure 4.11 depicts the case where there is only a marginal time-scale separation and we still see MMOs. To push this idea further, future work may consider a model where temperature and atmospheric carbon vary on roughly the same time-scale. As we briefly mentioned in the introduction, a delayed Hopf mechanism can generate MMOs in systems with two fast variables and one slow variable. This should provide a natural way to incorporate Milankovitch forcing into the model as a slow variable.

## CHAPTER 5

### Conclusion

The motivation for this thesis was to understand possible mechanisms for abrupt transitions observed in climate data. Mathematically, these abrupt transitions are interpreted as relaxation-type behavior, implying that the underlying dynamical system operates on multiple time scales. As is often the case in mathematically interesting problems, the “out of the box” theory does not apply to the models considered in this thesis.

#### 5.1. Non-smooth Canards

Chapter 2 establishes new results on canard-like phenomena in nonlinear, non-smooth, planar systems. The proofs rely on both the local analysis near the splitting line and global nonlinear dynamics. The local analysis was performed by Desroches et al. in [15], however the piecewise-linear nature of the model was not enough to produce a true canard explosion. As seen in Chapter 2, canard cycles in nonlinear piecewise-smooth systems behave much more like their smooth brethren. In some sense, the new results in Chapter 2 can be seen as bridging the gap between the quasi-canards in piecewise-linear systems and ‘standard’ canards in smooth systems.

The possibility of canards near a smooth fold in a piecewise-smooth system may not be surprising. The local blow-up analysis of Krupa and Szmolyan [33, 34] at the canard point still applies. Since there is a return mechanism, albeit a non-smooth one, the existence of canard orbits is a reasonable expectation. However, the locations of special curves in the  $\lambda, \epsilon$  parameter plane may change. More surprising is the existence of canards near a corner. The fast and slow dynamics are no longer tangent, the canard point is not a removable singularity of the slow dynamics, and

the local analysis of Krupa and Szmolyan does not apply. However, if the slope of the unstable branch of the critical manifold is small enough, there will be canard orbits. Theorem 2.3.5 essentially says if the splitting line crosses the unstable branch of the critical manifold near a fold, then the system will behave like a smooth system.

The side of the splitting line containing only a stable branch does not factor in to whether the system will exhibit canard behavior. However, it does factor into determining whether the periodic orbits will exist before or after the bifurcation. Showing the existence of a subcritical super-explosion relies on new local analysis, as no one had considered the case where the slope of the stable branch was small in a piecewise-smooth system.

## 5.2. Relaxation Oscillations in Ocean Models

In Chapter 3, two variations of Stommel's model are introduced to analyze a possible long-term ocean-atmosphere feedback mechanism and its role in D-O events. Both are three time-scale models with one fast variable corresponding to temperature difference between the equator and the pole as well as one intermediate variable corresponding to the analogous salinity difference. The main difference between the models is the number of slow variables.

The first model has only one slow variable, which is a ratio of forcing terms from Stommel's original model. The results established in Chapter 2 are applied to this model, providing conditions under which the model exhibits relaxation oscillations. This model, analyzed in Section 3.4, provided the initial motivation for extending the theory of canards to piecewise-smooth systems.

The second variation of Stommel's model incorporated two slow variables, allowing the two forcing terms to vary independently. Although not rigorously proven, strong analytical evidence is provided that the model will exhibit relaxation oscillations under a certain parameter regime. The argument is verified through simulation, showing that the model does, in fact, exhibit relaxation oscillations.

The oscillatory patterns produced by both models (Figures 3.5b and 3.9b) are remarkably similar. Additionally, the output appears qualitatively similar to the proxy data in Figure 3.1, suggesting that this feedback mechanism helps explain D-O events. One important similarity between the model output and proxy data is the asymmetric behavior that occurs while the model/climate is in each of the stable states. Mathematically, this can be explained by the slopes of the critical manifolds in the two models. The critical manifold is steeper in the haline state near the jump point, which is a corner. In the thermal state, the jump point is smooth, so the fast and slow dynamics are tangent. In the variations of Stommel’s model analyzed in Chapter 3, the steeper slopes correspond to a greater time-scale separation, so the dynamics in the haline state should be slower than those in the thermal state.

### 5.3. MMOs in a Climate Based Model

In Chapter 3, a smooth system is analyzed, exploring the relationship of mixed-mode oscillations to glacial-interglacial cycles. Again, relaxation-type behavior is observed in the data (Figure 4.1), accompanied by an asymmetric response in each of the stable states. This time, the asymmetric behavior is due to smaller structured oscillations appearing in the cold state. A fast/slow (or possibly three time-scale) model of temperature, atmospheric carbon, and oceanic carbon is analyzed. The model is shown to exhibit MMOs under a certain parameter regime.

The demonstration of MMOs relies on the presence of a folded node singularity with a global return mechanism. The folded node is accompanied with a funnel, and all trajectories in the funnel are singular canards. Finding conditions for a folded node is relatively simple. Finding a suitable global return mechanism that sends trajectories from the node into the funnel is significantly more difficult. The approach taken here is to find conditions analytically under which a singular periodic orbit satisfies the requirements, and a linear estimate of the funnel is used.

Due to the difficulty involved in finding conditions analytically, the return mechanism is often demonstrated numerically. There is another drawback to this approach:

since the linear approximation must lie inside the funnel for the analysis to work, the conditions found necessarily cut out a portion of the funnel near the boundary. The more complicated—and potentially more interesting—MMO patterns are observed when the return mechanism send trajectories near the boundary of the funnel. The model is simulated to show some of these complicated patterns.

#### 5.4. Future Work

My hope for this thesis is that it portrays climate science not only as a place where interesting mathematics can be applied, but also as an application that can inspire the development of new mathematics. Much in the way the first variation of Stommel’s model in Chapter 3 inspired work on canards in piecewise-smooth systems, I would like to generalize Theorem 3.4.1 to apply to piecewise-smooth systems—establishing Conjecture 3.4.6 as a veritable theorem in the process. Theorem 3.4.1 was originally proved while developing the theory for MMOs due to a folded node in smooth systems. Proving the non-smooth analog would go a long way towards developing a theory for MMOs in non-smooth systems—that is, the analog of Theorem 4.3.1.

## REFERENCES

1. Dorian S. Abbot, Aiko Voigt, and Daniel Koll, *The Jormungand global climate state and implications for Neoproterozoic glaciations*, Journal of Geophysical Research: Atmospheres **116** (2011), no. D18.
2. David Archer and Ray Pierrehumbert, *The warming papers*, John Wiley & Sons, 2011.
3. Eric Benoit, Jean Louis Callot, Francine Diener, Marc Diener, et al., *Chasse au canard (première partie)*, Collectanea Mathematica **32** (1981), no. 1, 37–76.
4. M Brøns, Martin Krupa, and Martin Wechselberger, *Mixed mode oscillations due to the generalized canard phenomenon*, Fields Institute Communications **49** (2006), 39–63.
5. M. I. Budyko, *The effect of solar radiation variations on the climate of the Earth*, Tellus **21** (1969), no. 5, 611–619.
6. Ken Caldeira and James F Kasting, *Susceptibility of the early Earth to irreversible glaciation caused by carbon dioxide clouds*, Nature **359** (1992), no. 6392, 226–228.
7. P. Cessi, *Convective adjustment and thermohaline excitability*, J. of Phys. Oceanography **26** (1996), 481–491.
8. A. Colin de Verdière, *A simple model of millennial oscillations of the thermohaline circulation*, J. of Phys. Oceanography **37** (2007), 1142–1155.
9. ———, *The instability of the thermohaline circulation in a low-order model*, J. of Phys. Oceanography **40** (2010), 757–773.
10. A. Colin de Verdière, M. Ben Jelloul, and F. Sévellec, *Bifurcation structure of thermohaline millennial oscillations*, J. of Climate **19** (2006), 5777–5795.
11. Thomas M. Cronin, *Paleoclimates: Understanding Climate Change Past and Present*, ch. Glacial Millennial Climate Change, pp. 149–184, Columbia University Press, 2010.
12. Michel Crucifix, *Oscillators and relaxation phenomena in Pleistocene climate theory*, Philosophical Transactions of the Royal Society A: Mathematical, Physical and Engineering Sciences **370** (2012), no. 1962, 1140–1165.
13. Willi Dansgaard, SJ Johnsen, HB Clausen, D Dahl-Jensen, NS Gundestrup, CU Hammer, CS Hvidberg, JP Steffensen, AE Sveinbjörnsdottir, J Jouzel, et al.,

*Evidence for general instability of past climate from a 250-kyr ice-core record*, Nature **364** (1993), no. 6434, 218–220.

14. M. Desroches, J. Guckenheimer, B. Krauskopf, C. Kuehn, H. Osinga, and M. Wechselberger, *Mixed-mode oscillations with multiple time scales*, SIAM Review **54** (2012), no. 2, 211–288.
15. Mathieu Desroches, Emilio Freire, S. John Hogan, Enrique Ponce, and Phanikrishna Thota, *Canards in piecewise-linear systems: explosions and super-explosions*, Proceedings of the Royal Society A: Mathematical, Physical and Engineering Science **469** (2013), no. 2154.
16. Henk Dijkstra, *Nonlinear physical oceanography: A dynamical systems approach to the large scale ocean circulation and el niño*, ch. A Dynamical Systems Approach, pp. 63–118, Springer, 2005.
17. Henk A. Dijkstra and Michael Ghil, *Low-frequency variability of the large-scale ocean circulation: A dynamical systems approach*, Reviews of Geophysics **43** (2005), no. 3, n/a–n/a.
18. Freddy Dumortier and Robert H Roussarie, *Canard cycles and center manifolds*, vol. 577, American Mathematical Soc., 1996.
19. Wiktor Eckhaus, *Relaxation oscillations including a standard chase on french ducks*, Asymptotic Analysis II, Springer, 1983, pp. 449–494.
20. Neil Fenichel, *Persistence and smoothness of invariant manifolds for flows*, Indiana Univ. Math. Journal **21** (1971), 193–226.
21. ———, *Asymptotic stability with rate conditions*, Indiana Univ. Math. Journal **23** (1974), 1109–1137.
22. ———, *Asymptotic stability with rate conditions II*, Indiana Univ. Math. Journal **26** (1977), 81–93.
23. ———, *Geometric singular perturbation theory for ordinary differential equations*, Journal of Differential Equations **31** (1979), 53–98.
24. A. Ganopolski and S. Rahmstorf, *Rapid changes of glacial climate simulated in a coupled climate model*, Nature **409** (2001), 153–158.
25. Paul Glendinning, *Stability, instability and chaos: an introduction to the theory of nonlinear differential equations*, Cambridge university press, 1994.
26. ———, *View from the pennines: non-trivial pursuits*, Mathematics Today-Bulletin of the Institute of Mathematics and its Applications **39** (2003), no. 4, 118–119.

27. Isaac M. Held, *The gap between simulation and understanding in climate modeling*, Bulletin of the American Meteorological Society **86** (2005), no. 11, 1609–1614.
28. Andrew McC. Hogg, *Glacial cycles and carbon dioxide: A conceptual model*, Geophysical Research Letters **35** (2008), no. 1.
29. Peter Imkeller, *Energy balance models—viewed from stochastic dynamics*, Stochastic Climate Models, Springer, 2001, pp. 213–240.
30. Christopher K. R. T. Jones, *Geometric singular perturbation theory*, Dynamical systems, Springer, 1995, pp. 44–118.
31. Marc Koper, *Bifurcations of mixed-mode oscillations in a three-variable autonomous van der pol-duffing model with a cross-shaped phase diagram*, Physica D: Nonlinear Phenomena **80** (1995), no. 1, 72–94.
32. P. Kowalczyk and P. Glendinning, *Boundary-equilibrium bifurcations in piecewise-smooth slow-fast systems*, Chaos: An Interdisciplinary Journal of Nonlinear Science **21** (2011), no. 2, 1–12.
33. M. Krupa and P. Szmolyan, *Extending geometric singular perturbation theory to nonhyperbolic points—fold and canard points in two dimensions*, SIAM Journal on Mathematical Analysis **33** (2001), no. 2, 286–314.
34. M. Krupa and P. Szmolyan, *Relaxation oscillation and canard explosion*, Journal of Differential Equations **174** (2001), no. 2, 312–368.
35. Martin Krupa and Martin Wechselberger, *Local analysis near a folded saddle-node singularity*, Journal of Differential Equations **248** (2010), no. 12, 2841 – 2888.
36. Christian Kuehn, *On decomposing mixed-mode oscillations and their return maps*, Chaos: An Interdisciplinary Journal of Nonlinear Science **21** (2011), no. 3, 1–15.
37. Corinne Le Quéré and Nicolas Metzl, *Natural processes regulating the ocean uptake of CO<sub>2</sub>*, SCOPE-Scientific Committee on Problems of the Environment International Council of Scientific Unions **62** (2004), 243–256.
38. Timothy M. Lenton and Christopher Huntingford, *Global terrestrial carbon storage and uncertainties in its temperature sensitivity examined with a simple model*, Global Change Biology **9** (2003), no. 10, 1333–1352.
39. Lorraine E. Lisiecki and Maureen E. Raymo, *A pliocene-pleistocene stack of 57 globally distributed benthic  $\delta O^{18}$  records*, Paleoceanography **20** (2005), no. 1.
40. James Lovelock, *Gaia: The living earth*, Nature **426** (2003), 769–770.



41. R. McGehee and C. Lehman, *A paleoclimate model of ice-albedo feedback forced by variations in earth's orbit*, SIAM Journal on Applied Dynamical Systems **11** (2012), no. 2, 684–707.
42. Didier Paillard and Frédéric Parrenin, *The antarctic ice sheet and the triggering of deglaciations*, Earth and Planetary Science Letters **227** (2004), no. 34, 263 – 271.
43. J. R. Petit, J. Jouzel, D. Raynaud, N. I. Barkov, J.M. Barnola, I. Basile, M. Bender, J. Chappellaz, M. Davis, G. Delaygue, M. Delmotte, V. M. Kotlyakov, M. Legrand, V. Y. Lipenkov, C. Lorius, L. PÉpin, C. Ritz, E. Saltzman, and M. Stievenard, *Climate and atmospheric history of the past 420,000 years from the Vostok ice core, Antarctica*, Nature **399** (1999), 429–436.
44. Rafel Prohens and Antonio E Teruel, *Canard trajectories in 3d piecewise linear systems*, Discrete and Continuous Dynamical Systems **33** (2013), no. 10, 4595–4611.
45. D.A. Randall, R. A. Wood, S. Bony, R. Colman, T. Fichefat, J. Fyfe, V. Kattsov, A. Pitman, J. Shukla, J. Srinivasan, R. J. Stouffer, A. Sumi, and K. E. Taylor, *Climate change 2007: The physical science basis. contribution of working group I to the fourth assessment report of the intergovernmental panel on climate change*, ch. Climate Modes and Their Evaluation, pp. 590–662, Cambridge University Press, Cambridge, United Kingdom and New York, NY, USA, 2007.
46. Andrew Roberts and Paul Glendinning, *Canard-like phenomena in piecewise smooth systems*, arXiv:1311.5192, 2013.
47. H. Rotstein, S. Coombes, and A. Gheorghe, *Canard-like explosion of limit cycles in two-dimensional piecewise-linear models of FitzHugh-Nagumo type*, SIAM Journal on Applied Dynamical Systems **11** (2012), no. 1, 135–180.
48. Jonathan Rubin and Martin Wechselberger, *Giant squid-hidden canard: the 3d geometry of the Hodgkin-Huxley model*, Biological Cybernetics **97** (2007), no. 1, 5–32.
49. ———, *The selection of mixed-mode oscillations in a hodgkin-huxley model with multiple timescales*, Chaos: An Interdisciplinary Journal of Nonlinear Science **18** (2008), no. 1, 015105–015105.
50. Raj Saha, *The role of sea ice in thermohaline oscillations*, Ph.D. thesis, University of North Carolina at Chapel Hill, 2011.
51. ———, *Periodic fluctuations in deep water formation due to sea ice*, preprint, March 2012.

52. Barry Saltzman and Kirk A. Maasch, *Carbon cycle instability as a cause of the late Pleistocene ice age oscillations: Modeling the asymmetric response*, Global Biogeochemical Cycles **2** (1988), no. 2, 177–185.
53. ———, *A first-order global model of late Cenozoic climatic change*, Earth and Environmental Science Transactions of the Royal Society of Edinburgh **81** (1990), 315–325.
54. Barry Saltzman and Kirk A. Maasch, *A first-order global model of late Cenozoic climatic change ii. further analysis based on a simplification of CO<sub>2</sub> dynamics*, Climate Dynamics **5** (1991), no. 4, 201–210 (English).
55. Barry Saltzman, Alfonso Sutera, and Alan Evenson, *Structural stochastic stability of a simple auto-oscillatory climatic feedback system.*, Journal of Atmospheric Sciences **38** (1981), 494–503.
56. J. Schewe, A. Levermann, and H. Cheng, *A critical humidity threshold for monsoon transitions*, Climate of the Past Discussions **7** (2011), no. 3, 1737–1765.
57. William D Sellers, *A global climatic model based on the energy balance of the Earth-atmosphere system*, The Warming Papers (2011), 125.
58. U. Siegenthaler and J. L. Sarmiento, *Atmospheric carbon dioxide and the ocean*, Nature **365** (1993), 119–125.
59. Daniel M. Sigman and Edward A. Boyle, *Glacial/interglacial variations in atmospheric carbon dioxide*, Nature **407** (2000), 859–869.
60. D. J. W. Simpson and J. D. Meiss, *Andronov–Hopf bifurcations in planar, piecewise-smooth, continuous flows*, Physics Letters A **371** (2007), no. 3, 213–220.
61. Henry Stommel, *Thermohaline convection with two stable regimes of flow*, Tellus **13** (1961), no. 2, 224–230.
62. Peter Szmolyan and Martin Wechselberger, *Canards in  $\mathbb{R}^3$* , Journal of Differential Equations **177** (2001), no. 2, 419 – 453.
63. Peter Szmolyan and Martin Wechselberger, *Relaxation oscillations in  $\mathbb{R}^3$* , Journal of Differential Equations **200** (2004), no. 1, 69–104.
64. Ka Kit Tung, *Simple climate modeling*, Discrete and Continuous Dynamical Systems **7** (2007), no. 3, 651–660.
65. Balth Van der Pol, *LXXXVIII. on relaxation-oscillations*, The London, Edinburgh, and Dublin Philosophical Magazine and Journal of Science **2** (1926), no. 11, 978–992.

66. Lennaert van Veen, *Overturning and wind-driven circulation in a low-order ocean-atmosphere model*, Dynamics of atmospheres and oceans **37** (2003), no. 3, 197–221.
67. M. Wechselberger, *Existence and bifurcation of canards in  $\mathbb{R}^3$  in the case of a folded node*, SIAM Journal on Applied Dynamical Systems **4** (2005), no. 1, 101–139.
68. Pierre Welander, *A simple heat-salt oscillator*, Dyn. Atmos. Oceans **6** (1982), 233–242.
69. Esther Widiasih and Jim Walsh, *A dynamics approach to a low order climate model*, Discrete and Continuous Dynamical Systems (to appear).
70. Esther R. Widiasih, *Dynamics of a discrete time energy balance model with ice albedo feedback*, Ph.D. thesis, University of Minnesota, 2010.
71. Christopher L. Wolfe and Paola Cessi, *The adiabatic pole-to-pole overturning circulation*, Journal of Physical Oceanography **41** (2011), no. 9, 1795–1810.
72. Yuuki Yamamoto, Naoki Kitahara, and Makoto Kano, *Long memory effect of past climate change in Vostok ice core records*, Thermochemica Acta **532** (2012), 41–44.